Supported Metal Catalyst Preparation using Deep Eutectic Solvents

Dissertation

Zur Erlangung des Doktorgrades der Naturwissenschaften
(Dr. rer. nat.)
an der Fakultät für Chemie und Pharmazie
der Universität Regensburg

vorgelegt von
Melanie Iwanow
aus Elisabethszell
2019

This work has been carried out between December 2015 and May 2019 under the supervision of Prof. Dr. Burkhard König at the University of Regensburg, Institute of Organic Chemistry and at the Fraunhofer Institute for Interfacial Engineering and Biotechnology IGB, Straubing branch, Bio, Electro and Chemocatalysis BioCat.

Date of submission: 29.05.2019
Date of colloquium: 05.07.2019

Board of examiners:	Prof. Dr. Alexander Breder	(chair)
	Prof. Dr. Burkhard König	(1st referee)
	Prof. Dr. Volker Sieber	(2nd referee)
	Prof. Dr. Frank-Michael Matysik	(examiner)

"Das schönste Glück des denkenden Menschen ist,

das Erforschliche erforscht zu haben und das Unerforschliche zu verehren"

Johann Wolfgang von Goethe

„Das, wobei unsere Berechnungen versagen, nennen wir Zufall“

Albert Einstein

(Nobelpreis für Physik, 1922)

Für meine Familie

Für Oma

TABLE OF CONTENTS

CHAPTER 1

1 Activated Carbon as Catalyst Support: Precursor, Preparation, Modification and Characterization

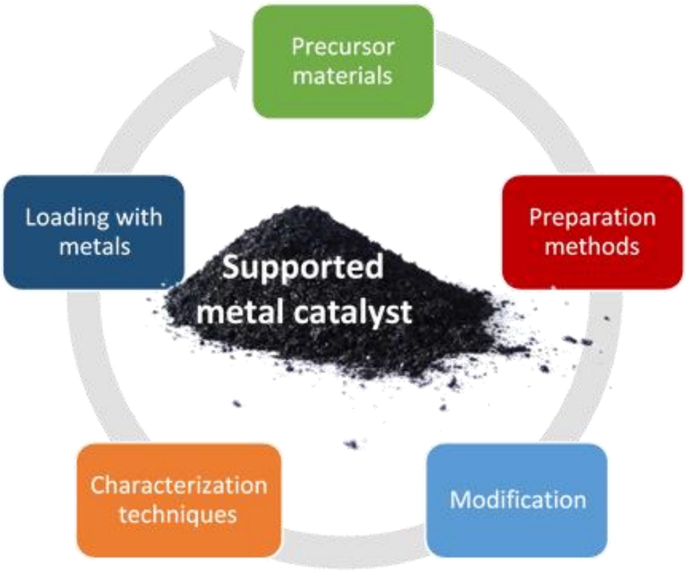

This chapter has been prepared for submission in Catalysis Science & Technology:

M. Iwanow, T. Gärtner, V. Sieber, B. König, *Catalysis Science & Technology* **2019**, submitted.

MI carried out the literature research and wrote the manuscript. TG, VS and BK supervised the project and BK is the corresponding author.

1.1 Introduction

Support materials for metal catalysts allow the dispersion and stabilization of small metal particles on a surface. Compared to the bulk metal, these catalyst preparations present a larger surface area of catalytically active atoms.[1] The use of activated carbon as support for metal catalysts shows several advantages compared to other support materials. The carbon surface is inert, especially in strongly acidic and basic conditions or the pore size distribution and the chemical properties on the surface can be adjusted (polarity and hydrophobicity) according to the applications planned. In addition, metal particles can be recovered simply by burning the carbon support.[1-2] Thus, porous carbon materials represent a large part of the supporting materials for the preparation of heterogeneous catalysts. Nevertheless, only a small amount of the worldwide produced activated carbon (< 1 %) is used as catalyst support. A possible reason may be the lack of reproducibility due to inconsistent carbon precursor compositions.[2]

In general, activated carbon is an amorphous carbon modification with a high surface area and a well-developed porosity, which can be produced from a variety of carbon sources.[3] The preparation of activated carbons is already broadly covered in the literature, so only a brief overview with selected examples is presented here. Emphasis is given to carbon precursors, preparation and modification methods, characterization techniques and metal loading on the carbon materials.

1.2 Precursor materials for activated carbon production

Many cheap raw materials with high carbon content can be used for the production of activated carbon.[4] Fossil and renewable sources for the preparation of activated carbon are discussed in this part of the review, as well as special precursor solutions or ionic liquids and deep eutectic solvents as non-conventional precursor materials. The properties of the resulting activated carbon depend, in addition to the type of precursor material, on the preparation/ activation method and the modification used.

1.2.1 Coal

In the beginning of the 1990s, 360 kilotons activated carbon were produced, whereby 42 % were based on coal as precursor due to the availability and low cost of coals such as brown coals, bituminous coals, petroleum cokes or anthracites. The coals should have a low mineral matter content and thus, a low ash content.[4-5] Bituminous coal-based activated carbons result in a well-developed porous structure due to the presence of primary pores in the coals. However, the size of these pores is very small.[5] Activated carbons prepared from bituminous coals are more durable compared to other coal-based carbons.[6] Petroleum coke as by-product of the refinery industry, shows a high carbon content, low amount of ash and is widely available.[7] Anthracites are very suitable precursors for activated carbon preparation, since they are high-rank coals (high C to H atomic ratio without carbonization) and show a non-negligible volume of very fine micropores.[8-9]

Various working groups investigated the preparation of activated carbons by different methods from coal precursors. Yang *et al.* synthesized nitrogen-doped activated carbon from petroleum coke for an enhanced CO_2 capture.[7] Pietrzak *et al.* used high volatile bituminous coals, brown coals and anthracites for modified activated carbon preparation.[5, 10-12] Lillo-Ródenas *et al.* investigated the chemical activation with sodium or potassium hydroxide by the use of an anthracite precursor.[8, 13-14]

1.2.2 Wood

Non-fossil precursors for the preparation of activated carbons are of great interest due to an increasing demand of these materials. Wood and the lignocellulosic wastes from forestry and agriculture are well-suited for this purpose.[15] Wood is mainly composed of cellulose (40 wt% to 55 wt%), hemicelluloses (mostly xylan in hardwoods with 20 wt% to 35 wt%) and lignin (18 wt% to 35 wt%). Cellulose maintains the structure of the cell walls of plants and is the most abundant raw material with a production of 10^{11} - 10^{12} tons per year, followed by lignin as second most abundant raw material.[16] Lignin is a three-dimensional phenolic polymer and is responsible for the cementation of cellulose fibres in plants.[17] Hemicelluloses, predominantly xylan, are non-cellulosic polysaccharides with a comparable low molecular weight.[15]

Khezami *et al.* investigated the preparation of activated carbon from wood and its main components: cellulose, xylan and lignin.[15] Suhas *et al.* reviewed the usage of cellulose as well as lignin for activated carbon preparation in detail.[16-17] Hameed and coworkers prepared high surface area activated carbon from wood sawdust.[18]

1.2.3 Agricultural waste/ biomass

The usage of agricultural waste as precursor for activated carbon materials is summarized in a variety of reviews.[3, 19-24] Any low cost lignocellulosic materials with high carbon content are of great interest as starting material.[22] An exemplary overview of agricultural by-products and waste used for the production of activated carbon materials is shown in Table 1.1.

Table 1.1. Exemplary overview of agricultural waste sources for activated carbon production.

Carbon source	References
straw	[25] [26] [27] [28] [29]
rice husk	[30] [23] [31] [32] [33]
bagasse	[30] [34] [35] [36] [37]
miscanthus	[38] [39]
bamboo	[40] [41] [42]
cotton residues	[43] [44]
nutshells	[45] [46] [47] [48] [49]
fruit pits	[49] [50] [51] [52] [53]
fruit seeds	[54] [55] [56]
fruit peels	[57] [58] [59]
coconut shells	[60] [61] [62] [63]
olive stones	[64] [65] [66]
sunflower seed oil residues	[67] [68]
coffee residue	[69] [70]
corn cobs	[71] [72]
oil palm residues	[73] [74] [75]
rotten strawberries	[76]

According to Ioannido *et al.*, the composition and structure of the used raw materials determine the reactivity during pyrolysis and activation steps and thus, the resulting elemental composition. They concluded that pyrolysis of agricultural waste provides up to twice the amount of char obtained from wood. Different starting materials yield activated carbons with different ash contents or BET surface areas. Nutshells and cherry stones show for example less ash content compared to grape seeds. Olive waste and bagasse result in activated carbons with high surface areas, whereas straw is less suitable to produce large surfaces.[19] Yahya *et al.* mentioned that the yields of the activated carbons prepared from these residues is lower compared to anthracite or coal as starting materials. Nevertheless, high volatile matter content in the biomass are advantageous for the production of porous activated carbon materials as well as the low cost of the agricultural waste.[22]

1.2.4 Ionic liquids and deep eutectic solvents

Zhang *et al.* demonstrated the preparation of carbon materials with high surface areas from protic ionic liquids and salts. The precursors have low-molecular weights, are available and cheap. Preparation of the carbon materials is simple: Neutralization of the nitrogen-containing bases *e.g.* phenanthroline or 3-cyanopyridine with sulfuric acid and subsequent removal of the solvent leads to the desired protic ionic liquids and salts. Carbonization at 1000 °C results in the final carbon materials with high nitrogen content without further modification. The basic components of the protic ionic liquids influence the yield of the materials. Thermally stable benzene moieties increase significantly the amount of carbon material produced, whereas mixtures based on amines or heterocycles decrease the yields.[77] The salt templating method developed of Antonietti and coworkers produces carbon materials with large surface areas from ionic liquids. A defined salt mixture was added to the ionic liquids 1-butyl-3-methyl-pyridinium dicyanamide (Bmp-dca, N-doped materials) or 1-ethyl-3-methyl-imidazolium tetracyanoborate (Emim-tcb, N- and B-doped materials) and the mixture was heated under nitrogen atmosphere. Removal of the salt by immersing in water for several hours, filtration and drying in vacuum lead to the final carbon material.[78] Iwanow *et al.* investigated deep eutectic solvents as raw materials for activated carbon production. They dissolved the metal salts already in the low melting mixtures before pyrolysis and prepared carbon-supported metal catalysts in one-step. Nevertheless, the surface area of these materials is much lower compared to the conventional activated carbons, but high nitrogen contents are obtained depending on the composition of the deep eutectic solvents.[79]

1.2.5 Precursor solutions

Xu *et al.* used energy-rich carbon precursors for the spherical carbon preparation via ultrasonic spray pyrolysis. Lithium, sodium or potassium propiolates are one class of such energy-rich materials and exhibit leaving groups such as CO, CO_2 or C_2H_2 eliminated by decarbonylation or decarboxylation. Poly(propiolate) salts are formed by polymerization of the starting materials after heating. The different cations of the propiolates cause changes in the thermal behavior of the starting materials, since different temperatures are required for the decomposition or different amounts of gases are released. Alkali salts of acetylene dicarboxylic acid can also be used as precursor for the preparation of carbon spheres. The structure and morphology of the carbon spheres can be influenced by the used alkali salts.[80]

1.3 Activated carbon preparation

The following chapter summarizes the different preparation methods for activated carbon materials. Depending on the carbon source, different pre-treatment steps are required before the carbonization/pyrolysis and activation of the precursor materials could be performed. In addition to the most widely used method of physical or chemical activation, specialized methods such as salt templating and ultrasonic spray pyrolysis are presented.

1.3.1 Pre-treatment

Different pre-treatment steps are necessary before carbonization or activation of the carbonaceous precursors. The use of biomass as carbon precursor requires often additional washing steps to remove impurities.[30] Drying at ~100 °C for a defined time removes the free moisture in the material, which could affect the carbonization step.[81] A defined and standardized starting material size of the raw materials is also essential for the activated carbon production process and is obtained by milling and sieving of the carbon precursors.[30, 45, 81-82]

1.3.2 De-ashing / demineralization

Activated carbons contain different ash contents due to mineral components in the raw materials, which affect the chemical properties of the prepared materials. For catalytic applications, only activated carbons with the lowest possible ash contents can be used. Prior to the production of activated carbons from the precursor materials, the amount of ash and minerals in the materials are reduced by leaching with acidic or basic solutions.[83] Samples are mostly demineralized by concentrated hydrochloric and hydrofluoric acids according to the Radmacher and Mohrhauer method.[10] Dofour *et al.* described the procedure in detail. The stepwise treatment with hydrochloric acid, hydrofluoric acid and again hydrochlorid acid removes the metal oxides and silica in the samples and is a comparatively soft method for the carbon material. The treatment with HNO_3 is another possibility for the removal of the mineral contents; however, this method causes the oxidation of the material, and thus produces new oxygen-containing surface functionalities.[84]

1.3.3 Physical activation

Physical activation of carbon materials is a two-step process. After preparation of char by carbonization of the precursor materials for a certain time at a defined temperature under inert gas atmosphere, air, CO_2 or steam activate the materials at higher temperatures (800 - 1000 °C) to form a porous structure according to the equations 1 - 3.[81, 85-86]

$$C + O_2 \rightarrow CO_2 \quad (1)$$

$$C + CO_2 \rightarrow 2\,CO \quad (2)$$

$$C + 2\,H_2O \rightarrow CO_2 + 2\,H_2 \quad (3)$$

It is necessary to eliminate a large amount of internal carbon for the formation of a well-developed and highly porous carbon structure.[6] In general, the physical activation of carbon materials has the advantage over chemical activation to avoid impurities or additives in the final materials from the incorporation of the activating substances.[16]

Several literature reports show a larger reactivity of steam as mild oxidizing reagent compared to carbon dioxide. Nevertheless, no clear tendencies were found regarding the pore development.[87-91] Rodríguez-Reinoso *et al.* and Zamora and coworkers investigated the influence of the different physical activation gases on the development of porosity from olive stone-based chars. They concluded that activation with steam results in activated carbon materials with lower micropore volumes and wider pore size distributions (higher amounts of meso- and macropores are formed) compared to carbon dioxide.[64, 87] Kalderis *et al.* prepared activated carbons from bagasse and rice husk by physical and chemical activation. They found that physical activation leads to significantly lower surface areas compared to the surface obtained by chemical activation with zinc chloride at the same temperature.[30]

1.3.4 Chemical activation

Chemical activation is a one-step method. Impregnation or mixing of the carbon precursor with the activating agent and subsequent carbonization of that mixture leads to highly porous activated carbon materials.[8, 92] The activation agents promote a cross-link formation due to their dehydration properties, which causes a rigid matrix. This structure is less susceptible to volatile loss and volume contraction during the carbonization, resulting in higher activated carbon yields, since no carbon burn-off is necessary.[6, 85] Additional advantages of the chemical activation are lower temperatures for pyrolysis, the formation of very high surface areas and it is possible to control the development of microporosity *e.g.* a narrow pore size distibution can be obtained.[8, 15] Various parameters influence the formation of porosity during the chemical activation process. A few examples for the different preparation conditions are the choice of the activing agent (KOH, NaOH,

$ZnCl_2$, H_3PO_4, $MgCl_2$, $AlCl_3$, K_2CO_3, etc.), the impregnation technique or physically mixing processes used, the activation agent to carbon precursor ratio, the flow of inert gas during carbonization and the pyrolysis temperature and time.[13-14]

Highly developed pore structures are obtained by chemical activation of carbon precursors with hydroxides.[9, 14] Song *et al.* investigated the activated carbon preparation by chemical activation with KOH from corn cob. They found that KOH plays a crucial role in the formation of porosity. Metallic potassium is formed during the carbonization of the carbon precursor, which intercalates in the carbon structure and is responsible for further release of carbon dioxide, carbon monoxide and hydrogen.[71] According to Marsh and Rodriguez-Reinoso, the activating agents react with the formed char and not directly with the carbon precursor to form a porous structure.[56, 93] Hsu *et al.* studied the preparation of highly porous activated carbons from bituminous coal by chemical activation with $ZnCl_2$, H_3PO_4 and KOH. The choice of activating reagent influences strongly the activated carbon properties. Higher yields are obtained by activation with $ZnCl_2$ and H_3PO_4 compared to KOH, whereas less porosity is developed. The acidic character of the activation agents $ZnCl_2$ and H_3PO_4 seems to be suitable for the development of large pore structures in the carbon source.[6] Diamadopoulos and coworkers observed also the production of smaller surface areas by H_3PO_4 activation of bagasse and rice husk due to a reaction of the activating agent with the carbon precursor. Thereby, phosphate esters or polymerization by-products are formed, which are strongly bonded to the carbon matrix and are not removed by the subsequent washing step.[30]

1.3.5 Salt templating

Fechler *et al.* developed the salt templating method for preparation of highly porous functional carbon materials using ionic liquids as carbon source. Inorganic non-carbonizable salts are mixed with the carbon precursor and elevated temperatures lead to condensation and scaffolding of the carbon source by the presence of the molten salt. The aim of the method is to retain as long as possible the miscibility of the carbon precursor and salt melt during the reaction. After a washing step to remove the salt from the carbon materials, high specific surface areas are obtained with pore sizes corresponding to the salt clusters and salt percolation structures. The polarizability can be adjusted by selection of the cation size and counterion, which influences the pore size and the miscibility during the production process.[78, 94]

1.3.6 Ultrasonic spray pyrolysis (USP)

The USP method for continuous preparation of meso- and macroporous carbon spheres was used by Skrabalak *et al.*. Ultrasonically nebulization of a precursor solution (carbon source and inorganic salts) by a humidifier results in a mist of micron-sized droplets. These droplets are transported into a furnace by an inert gas stream, where the solvent evaporates and the precursor decomposes. The formed carbon sphere/ salt composites are collected in water bubblers. The salt is dissolved in the collection solvent and by-products either remain in the solvent or are removed by the gas stream, resulting in the desired porous carbon spheres (Figure 1.1).[95]

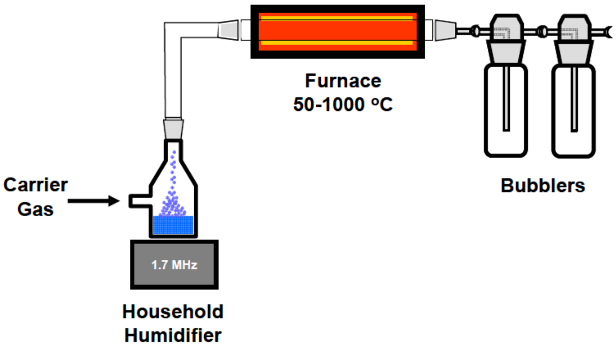

Figure 1.1. Experimental setup of ultrasonic spray pyrolysis. - Reprinted with permission from S. E. Skrabalak, K. S. Suslick, Journal of the American Chemical Society 2006, 128, 12642-12643. Copyright (2006) American Chemical Society.

Suslik and coworkers used the USP process for preparation of well-dispersed iron impregnated porous carbon microspheres. An iron source ($FeCl_3$ or $Fe(NO_3)_3$ is already added to the precursor solution consisting of sucrose as carbon source and NaCl or $NaNO_3$ as inorganic salt. The pyrolysis of the precursor solution leads to dehydration of carbon as well as iron salt conversion to crystalline or non-crystalline iron species depending on the production conditions. The porosity of the carbon spheres is induced by either aromatization of carbon around an *in situ* template, *in situ* chemical activation or gasification of carbon.[96] Xu *et al.* found that the morphology of the porous carbon materials, prepared from propiolate salts with USP, are dependent on the choice of starting materials. The thermal decomposition behavior of the precursors, and thus the resulting morphology of the carbon materials is influenced by the propiolate cations.[80]

1.3.7 Spherical carbons

The preparation of spherical mesoporous carbon particles as catalyst support with high surface areas, controllable particle sizes and large uniform pores received much attention.[97-98] One possibility to prepare such carbon spheres with defined particle sizes and pore structures is the nanocasting strategy using silica scaffolds as shown by Fuertes *et al.*.[99] Nevertheless, due to the complex and high-cost preparation of these carbon materials (preparation of the solid scaffolds, pyrolysis of the carbon precursors in these templates and finally, the selective removal of the silica template) and the risk of structure and morphology defects by the harsh carbonization and template removal processes, this method is industrially infeasible.[97]

Carbon spheres are also prepared by hydrothermal treatment of aqueous low cost biomass, such as lignocellulosic materials or carbohydrate precursor solutions at defined temperatures in closed systems.[100-101] The proposed mechanism of the formation of carbon spheres seems conform to the LaMer model and starts with a polymerization step of the carbohydrate monomers, followed by a carbonization step when the nucleation is caused by the supersaturation of the solution. The resulting nuclei grow uniformly until the final size is obtained depending on the growth parameters.[102] Linares-Solano and coworkers activated the resulting carbon spheres to develop different textural properties by maintaining the morphology. Surface areas higher than 3100 $m^2\ g^{-1}$ could be synthesized.[98]

Yan *et al.* presented another method for the preparation of spherical carbon materials by aerosol-assisted self-assembly using amphiphilic triblock copolymers as template and low-molecular weight soluble phenol resin as carbon source. The amphiphilic surfactant influences the pore size and mesostructure of the resulting spherical carbons. Finally, the template is removed by calcination.[97]

1.3.8 Comparison of conventional and microwave heating

Conventional heating for physical or chemical activation of the precursor materials has several drawbacks such as the non-uniform heating of the samples or a high-energy demand due to long carbonization and activation times at high temperatures.[103-104] Microwave irradiation is a promising alternative with some advantages. In contrast to conventional heating, which is based on the convection mechanism involving conduction and radiation, the sample can be heated uniformly and contactless by the heat generated from electromagnetic energy, resulting in significant time reduction and therefore energy savings.[103] The major problem of microwave heating is that the carbon sources are poor receptors for the irradiation, thus activation agents are necessary as heat carriers and for promotion of porosity.[104]

Wang *et al.* prepared activated carbons with high surface areas by microwave-induced $ZnCl_2$ activation within minutes. The porosity of the materials can be simply tailored by the carbon precursor to $ZnCl_2$ ratio and the used microwave irradiation time.[104] Foo *et al.* investigated the activated carbon preparation by microwave heating with K_2CO_3 activation from wood sawdust. They obtained highly porous activated carbons by varying of the impregnation ratio, microwave power and irradiation time. They concluded that the high surface areas are formed due to opening of previously inaccessibly pores and the additional creation of new pores by the interior and volumetric heating of microwave radiation.[18] Lin and coworkers compared the activated carbon preparation with KOH activation by conventional and microwave heating. The microwave-induced materials showed higher surface areas compared to those prepared by conventional heating using the same precursor to activating agent ratio.[105]

1.4 Activated carbon modification

Depending on the starting materials or preparation methods used, various modification treatments can be performed to functionalize the surface of the activated carbons according to the subsequent use of the materials.

1.4.1 Surface area and porosity

In general, high surface areas and well-developed porosity of activated carbons are beneficial for the use as catalyst support to obtain a highly dispersed loading of metal particles on the surface. The size of the pores is also important. Highly porous activated carbons with narrow micropores can block active centers being not available for the reactants.[2] The surface area and development of porosity (amount of porosity, pore size and shape) of the activated carbons can be influenced by the used preparation conditions.

Lyubchik *et al.* used different chemical ($HClO_4$ or $Mg(ClO_4)_2$) and physical (CO_2) activation methods for the modification of the porosity of anthracite-based activated carbons. The final pore size distribution (mainly microporous or mainly mesoporous) depend on the choice of the activation agent, the treatment time and temperature and the initial textural properties of anthracite as carbon source.[106] Wang *et al.* found that acidic treatments generally enhance the surface area and porosity of activated carbons, since the inorganic impurities in the materials were removed. Hydrofluoric acid modification showed the greatest enhancement of the surface area and porosity.[107] However, the surface area and developed porosity of the activated carbon materials is only one parameter affecting the material application as catalyst support. Another important characteristic is the chemical composition of the activated carbon surface.[2]

1.4.2 Chemical surface properties

The chemical properties of the carbon surface influence the acid-base and hydrophilic character and can affect the preparation of carbon-supported catalysts. Different types of active phase-support interactions can be induced by the introduction of heteroatoms on the carbon surface, which is only marginally possible in other catalyst supports e.g. silica or alumina.[2] Depending on the application of the carbon-supported catalysts, different possibilies are available for the modification of the properties on the surface of the activated carbon materials.

Oxygen-containing surface groups

The amount and composition of oxygen-containing surface groups can be influenced by treatment with different oxidants such as H_2O_2, HNO_3, oxygen/ air, ozone or NaOCl. Thereby, the acidic or basic behavior and the resulting surface chemistry of the activated carbons are determined.

Jaramillo *et al.* investigated the influence of different oxidizing reagents on the activated carbon materials prepared from cherry stones. Different amounts of oxygen functional groups were found on the surface of the materials depending on the oxidizing agents used: $HNO_3 > O_3 > H_2O_2 > O_2$ (air). Mostly carboxyl groups are formed by the oxidative treatments with HNO_3 and ozone. However, HNO_3 also cause a decrease of microporosity and of the basic sites on the carbon materials compared to ozone modification, thus O_3 is the most promising reagent for the formation of oxygen functional groups.[108] Han *et al.* investigated activated carbons with similar porosity, but different amounts of oxygen groups on the surface. They observed a decrease of the hydrophobic property of the carbon surface due to formation of acidic groups by oxidization with H_2O_2. This property change, based on the increase of oxygen surface groups, made the surface more accessible for the aqueous metal solution during the impregnation process and results in a better platinum dispersion. Nevertheless, less acidic and more thermally stable surface groups avoid the sintering of the metal particles by enhanced metal-carbon interaction.[109] Figueiredo *et al.* observed different types of oxygen surface groups depending on the oxidizing agent. Oxidative treatment with liquid agents (HNO_3 or H_2O_2) increases the amount of carboxylic groups, while carbonyl and hydroxyl surface groups result from modification with O_2 or N_2O.[110]

Nitrogen-containing surface groups

Nitrogen-enrichment of activated carbons is possible at the precursor stage or as a modification step after the production of activated carbons and results mostly in a basic character of the prepared materials. Typical nitrogen agents are ammonia, urea or amines. Different types of nitrogen-containing functional groups on activated carbon surfaces are shown in Figure 1.2.[10, 111]

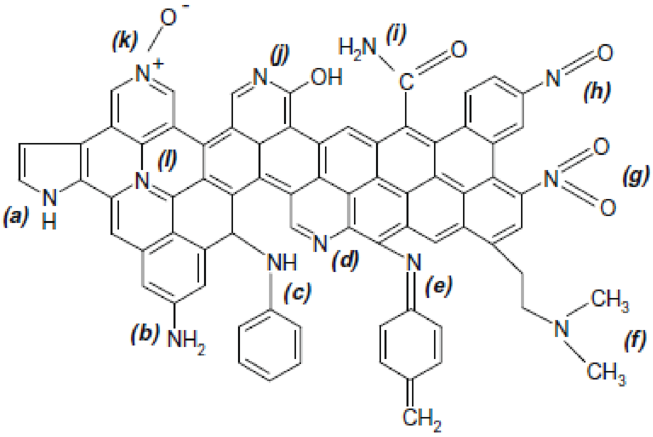

Figure 1.2. Overview of nitrogen-containing functional groups on the surface of activated carbons: a) pyrrole, b) primary amine, c) secondary amine, d) pyridine, e) imine, f) tertiary amine, g) nitro, h) nitroso, i) amide, j) pyridine, k) pyridine-N-oxide and l) quaternary nitrogen.[10] - Reprinted with permission of R. Pietrzak, Fuel, 2009, 88, 1871-1877. Copyright (2009) Elsevier Science Ltd.

Ammoxidation of activated carbons is a very effective process for the introduction of nitrogen surface groups. The simultaneous oxidation and nitrogenation of the activated carbon samples changes the chemical structure significantly, and thus the acid-base character of the materials. Pietrzak *et al.* observed that the amount of nitrogen in the activated carbons depends on the preparation stage at which the ammoxidation is performed and of the different pre-treated carbon precursors used. The largest nitrogen content in the samples was found by ammoxidation of demineralized coal in the last preparation step after carbonization and activation.[10] Hu and coworkers synthesized nitrogen-doped carbon materials from coconut shell by urea modification and K_2CO_3 activation. The carbonized precursor is mixed with urea (1:1 weight ratio), heated and the unreacted urea is removed by a washing step with hot water. Subsequently, the urea-treated samples are activated. The treatment with urea enhanced significantly the nitrogen content in the samples, while the final amount of nitrogen is reduced by the activation step.[63, 112]

1.5 Activated carbon characterization

Many production methods and possible precursors for activated carbon preparation are known. Also many characterization methods have been reported. In most cases, several characterization methods are used to be able to correlate the resulting activities and activated carbon properties with the preparation and modification methods. In the following, typical characterization techniques are introduced and the information obtained from the analytical methods is discussed on selected examples.

1.5.1 Surface characterization

Scanning electron microscopy (SEM)

Surface morphology of activated carbons is investigated with scanning electron micrographs. The measurement determines the porosity of a surface area. Cavities or holes can be observed on activated carbon with higher porosity, while smooth surfaces characterize activated carbon with less porosity.[71]

Singh *et al.* showed SEM pictures of activated carbons prepared from the biomass *Arundo donax* with different ratios of KOH as activating reagent. Smooth surfaces are found without KOH, while a high degree of porosity is obtained by the optimum KOH to biomass ratio, resulting in high surface areas.[113] Saka *et al.* have shown that the external surface of the activated carbons prepared from acorn shell by chemical activation with $ZnCl_2$ exhibits cracks and holes in different sizes. They concluded that a porous structure is formed due to the volatization of most of the organic compounds during the carbonization process and a ruptured surface is obtained.[46] SEM micrographs also allow the determination of different types of pores. The group of Okman showed SEM investigations on activated carbons prepared from grape seeds by activation with KOH. The sponge-like surface of the activated carbon indicates a microporous structure.[56]

Fourier transmission infrared spectroscopy (FTIR)

Activated carbon consists mainly of carbon atoms, besides different heteroatoms such as oxygen, hydrogen, nitrogen and sulphur. Thus, different functional groups govern the surface of the activated carbons and FTIR provides information on these chemical structures.[65] The spectra are usually recorded between 4000 cm^{-1} and 400 cm^{-1}. The most characteristic bands of functional groups on the surface of the activated carbons are ≈3500, 1700, 1610, 1420 and 1140 cm^{-1}, which indicate free or intermolecular bonded OH groups, carbonyl (C=O) stretching vibrations of carboxyl groups, ketones or aldehydes, C=C double bonds, aromatic rings and ether C-O stretching bonds, respectively.[65, 82, 114] Changes of the surface properties due to the modification of the activated carbon samples can also be detected by FTIR measurements.

Shafeeyan *et al.* investigated new nitrogen-containing functional groups on the surface of ammonia treated activated carbon samples such as bands of N-H stretching vibrations (3376 - 3294 cm^{-1}), cyclic amides (1665 - 1641 cm^{-1}), nitriles (2251 - 2265 cm^{-1}) and pyridine-like functionalities (1334 - 1330cm^{-1}). Simultaneously, a diminished band at about 1700 cm^{-1} was found due to the decomposition of the oxygen-containing surface groups at higher treatment temperatures.[114] The group of Moreno-Castilla investigated the treatment with oxidizing agents (H_2O_2 or HNO_3) or activating reagents by FTIR. They found that the amount of oxygen fixed on the surface of the treated carbons in form of carboxyl groups, ketones, ether groups and carboxyl-carbonate structures is higher using nitric acid compared to hydrogen peroxide.[115]

Nitrogen adsorption - desorption isotherms

The surface area and pore size distribution of solid catalyst materials can be determined by gas adsorption - desorption measurements at 77 K. To obtain reproducible isotherms from the measurements, a controlled outgassing of the adsorbent with a defined temperature, change in pressure and residual pressure is necessary to remove all physisorbed species from the surface. Different methods can be used for the measurements. The volumetric method with determination of the gas removed from the gas phase and the gravimetric method, where the uptake of the gas by the adsorbent is determined by the increase in mass. In addition, static or dynamic techniques are available for the determination of adsorbed gas.[116]

As a result, physisorption isotherms are obtained by plotting the amount of adsorbed gas n^a in mol g^{-1} against the equilibrium relative pressure (p/p^0). The resulting isotherms can be grouped in six different types. Type 1 isotherms are concave to the p/p^0 axis and n^a approaches the limiting value $p/p^0 \rightarrow 1$. These type is formed by microporous solids with a relatively small external surface for example of activated carbons or molecular sieve zeolites.[116]

Numerous methods are available for calculating surface area, pore size, pore distributions and pore volume by fitting to the isotherms with different assumptions. For example, Brunauer-Emmet-Teller (BET) method[117] or Langmuir method [118] for the determination of the surface area of porous materials, Dubinin-Radushkevich equation[119] for calculation of microporosity and Barrett-Joyner-Halenda model[120] for pore size distribution. In addition, the hysteresis between the adsorption and desorption gives information on mesopores. The absence of a hysteresis indicates that there is no or only little mesoporosity.[65] An overview of the pore classification and the concerning pore sizes is shown in Table 1.2.[116]

Table 1.2. Overview of the pore classification in the context of physisorption.[116, 121]

Pore type	**Pore size**
Macropores	> 50 nm
Mesopores	2 nm - 50 nm
Micropores	< 2 nm
Ultramicropores	< 0.7 nm

Sethia *et al.* investigated the activation temperature influence on the porosity and surface area of nitrogen-containing activated carbon samples by N_2 adsorption measurements. Non-activated carbon samples show a very low nitrogen uptake indicating small surface areas without pores. A sharp increase of the isotherms at very low relative pressures with subsequent stagnation could be observed with activated carbons prepared between 550 °C and 650 °C due to a narrowly distributed ultramicroporous structure. The prepared activated carbon sample at 700 °C present a broader isotherm knee resulting from a wider pore distribution.[122] Kalderis *et al.* prepared activated carbons from bagasse and rice husk by chemical activation with $ZnCl_2$, NaOH and H_3PO_4. They observed that the surface area of the activated carbon depends strongly on the activation agent used, the impregnation ratio of the raw material to activation agent, the activation temperature and activation time. $ZnCl_2$ shows the best results with surface areas of 674 and 750 m^2 g^{-1}, while the activation with H_3PO_4 leads to surface areas below 100 m^2 g^{-1} due to a high retention of phosphates in the carbon structures forming phosphate esters or polymerization by-products that bind on the solid carbon-matrix.[30]

Boehm titrations

Boehm titrations are used for the determination of acidic or basic surface oxygen functional groups of solid materials. Acidic character is caused by carboxyl groups (R-COOH), lactones (R-OCO), phenolic groups (R-OH) and carbonyl or quinone groups (R=O). Differentiation is possible by titration with different basic solutions $NaHCO_3$, Na_2CO_3, NaOH, $NaOC_2H_5$, respectively. Titration of the samples with hydrochloric acid determines the basic properties on activated carbon surface in form of pyrone or chromene-like structures and aromatic π-electrons.[108, 123-124]

Nowicki *et al.* showed different acidic and basic conditions on the surface of the activated carbon materials resulting from different activation methods of cherry stones-based carbons. Activation by carbon dioxide leads to basic surface character, while using the chemical activation with KOH results in weakly acidic surface properties of the materials. The temperature used for the activation shows less influence compared to the activation method.[52] Comparison of the amounts of acidic and basic surface groups on treated and untreated activated carbon from bituminous coal investigated Pietrzak. He found that the carbonization process reduces slightly the amount of acidic surface groups, while the amount of basic surface groups remains constant. Nitrogen introduction to the materials leads to an obvious decrease of acidic surface groups and simultaneously increase of basic properties.[10]

Phenol, methylene blue and iodine adsorption

Adsorption capacity and amount of pores of activated carbon materials are determined by using different adsorbates (phenol, methylene blue and iodine). The activated carbons are added to defined methylene blue or phenol solutions and are shaken for a certain time. The concentration of the adsorbates methylene blue and phenol is spectrophotometrically determined at defined absorbance wavelengths. The iodine number is determined by titration with sodium thiosulfate. Generally, the iodine number represents the surface area resulting from the amount of micropores (< 1 nm). Mesopores (< 1.5 nm) are denoted by methylene blue adsorption, which is also used as model substrate for the adsorption of organic pollutants. [51, 125] Phenol adsorption takes place in ultramicropores and micropores with diameters between 0.7 nm and 2 nm and thus, determination of specific surface areas is possible. In addition, phenol is the primarily used liquid-phase reference for adsorption studies. Adsorption capacity of phenol is influenced by oxygen-containing functional groups: basic properties promote the adsorption of phenol by oxidative coupling reactions and acidic functional groups decrease the amount of adsorbed phenol.[51, 126-127]

Duman and coworkers studied different pyrolysis temperatures and activation times with $ZnCl_2$ for the preparation of highly porous activated carbon from fruit stones and nutshells. They found that both conditions influence strongly the adsorption of phenol and methylene blue on the nutshell-based carbons. It is essential to find the optimum activation time, since shorter treatments (6 h) do not lead to a porous structure and longer activation times (24 h) causes a collapsing of the structure.[51] Song *et al.* used methylene blue adsorption and iodine number to investigate the surface area and porosity of the activated carbon prepared from corn cob by physical (steam) and chemical (KOH) activation with different carbonization and activation conditions. Chemical activation shows obviously larger surface areas compared to steam activation.[71]

Temperature-programmed desorption (TPD)

TPD is used for the study of surface oxides due to the thermal stability of the surface groups (Figure 1.3). The samples were heated in an inert gas atmosphere or in vacuum with a constant heating rate and the evolved gases are determined by mass spectrometry. In general, each type of surface group decomposes to a defined product such as CO_2 from carboxylic acid or lactones and CO from carbonyl, hydroxide or quinone groups, and thus information on the amounts of oxygen-containing surface groups are obtained. Nevertheless, the decomposition products are not always clearly assignable, since two adjacent carboxyl groups form primarily the anhydride followed by decomposition to CO and CO_2.[15, 123]

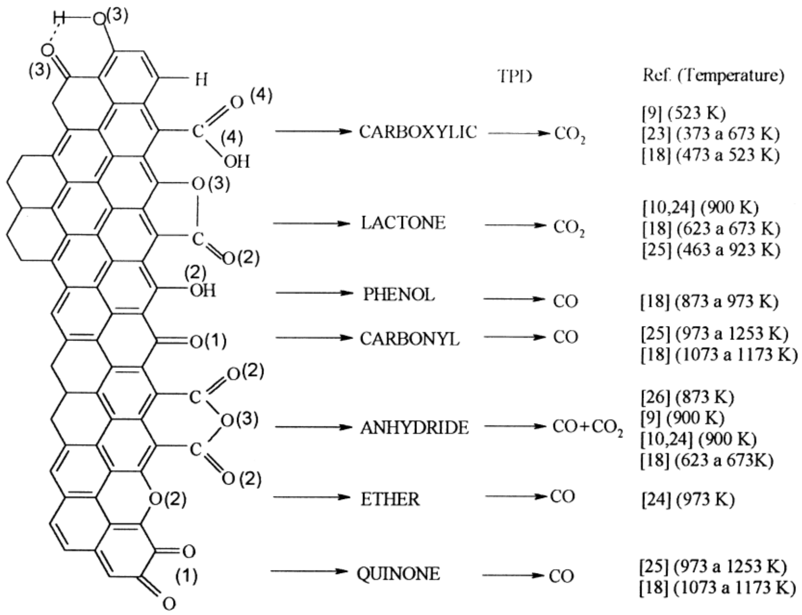

Figure 1.3. Overview of the different surface functional groups on activated carbon and the decomposition products and temperatures by TPD.[110] - Reprinted with permission of J. L. Figueiredo, M. F. R. Pereira, M. M. A. Freitas and J. J. M. Órfão, Carbon, 1999, 37, 1379-1389. Copyright (1999) Elsevier Science Ltd.

Capart and coworkers investigated the activated carbons produced from wood and the basic wood components lignin, cellulose and xylan by KOH activation with TPD. The different prepared materials showed no significant difference of the surface functionalities. All TPD spectra exhibit a water peak at about 500 K according to dehydration of carboxylic acid during formation of anhydrides, a CO peak at 900 K due to decomposition of carboxylic anhydrides and a CO_2 peak at about 500 K resulting from carboxylic acids.[15] Figueiredo *et al.* examined the influence of oxidative treatments on activated carbon by TPD studies. Enhanced CO and CO_2 peaks found by TPD indicate an increasing amount of oxygen-containing surface groups on the activated carbon materials. They could observe that gas phase oxidation leads to a larger amount of mainly hydroxyl and carbonyl groups, whereas liquid phase treatment with nitric acid results in an increase of carboxylic acid groups. [110] Lillo-Ródenas *et al.* used TPD for determination of the released gases during the activation process of anthracite with sodium or potassium hydroxide, and thus for clarification of the activation mechanism with hydroxides. The reaction of carbon precursor and metal hydroxide at lower temperatures (Na: 570 °C and K: 400 °C) leads to formation of hydrogen and metal carbonates as well as metallic metal or M_2O (M = Na or K). The absence of carbon dioxide at these temperatures suggests that the carbonates are not formed by reaction of hydroxides with CO_2. At higher temperatures, CO and CO_2 are found due to the decomposition of the metal carbonates. Moreover, they found that no porosity of the resulting materials was formed by using a metal carbonate instead of hydroxide as activation reagent.[8, 14] Pis and coworkers used the TPD method for evaluation of the thermal stability of introduced nitrogen functionalities by modification with ammonia due to the evolution of NH_3 and HCN. Depending on the modification temperature, nitrogen is incorporated mainly to aromatic rings at higher temperatures, while less temperature-stable amide-like functionalities are formed at lower temperatures.[128]

1.5.2 Composition of activated carbon

Elemental composition by CHNS/O

The elemental composition is determined for starting materials as well as for the resulting activated carbon materials. Thereby, the influence of the different preparation, activation and modification methods on the carbon or heteroatom content can be compared.

Nowicki *et al.* found that physical activation of cherry stones results in a higher carbon content and simultaneously lower hydrogen and oxygen amounts, while chemical activation shows only smaller changes of the elemental composition with exception of a significant decrease of the nitrogen content.[52] Pietrzak examined the different elemental compositions of the bituminous coal based materials after carbonization, activation and ammoxidation for the enrichment of nitrogen. He found that the carbonization step causes an increase of the carbon content, a decrease of oxygen and hydrogen and the nitrogen amount stays almost constant. The activation process leads to an increase of oxygen, while all other elements decrease. Thus, the activation reagent (KOH) oxidizes the initial material during this step. As expected, the ammoxidation results in an enrichment of nitrogen.[10]

Scanning electron microscopy with energy-dispersive X-ray (SEM-EDX)

An energy-dispersive X-ray detector allows the investigation of the composition of the materials and of the distribution of elements on the investigated materials by EDX mapping.

Ternero-Hidalgo *et al.* found by SEM-EDX investigations that the treatment of olive stones-based carbons with H_3PO_4 during chemical activation or modification with HNO_3 occurs uniformly on the entire surface, since the heteroatoms (nitrogen and phosphorous) are quite homogeneously distributed on the surface of the activated carbons.[129]

X-ray photoelectron spectroscopy (XPS or ESCA)

X-ray photoelectron spectroscopy determines the chemical state of elements and the composition of the sample on the upper surface layer (only few atomic layers). X-ray irradiation (Mg-Kα or Al-Kα) excite core electrons to leave the atoms and their kinetic energies are measured. The characteristic binding energies are calculated from the measured kinetic energies. After baseline subtraction, the curves are fitted to Gaussian and Lorenztian peak shapes with different proportions. For calibration of the XPS method, the carbon 1s electron binding energy is referenced at 284.6 eV.[10, 123, 130-131]

Pietrzak investigated with XPS different methods for the enrichment of bituminous coal by ammoxidation. The greatest enrichment of nitrogen occurs by using the ammoxidation as last step after carbonization and activation of the bituminous coal. The measurements shows that nitrogen is introduced in the activated carbon as amines, imines, amides, pyridine nitrogen and pyrrole nitrogen or as oxidized nitrogen species *e.g.* pyridine-N-oxides.[10] Díaz-Terán *et al.* examined the surface of the samples (surface groups, chemical state of the elements, metal content and distribution) during the activation process of lignocellulosic precursor with KOH by XPS. They observed that the oxygen on the surface of the material is associated with potassium as carbonates or oxides.[130] Cordero and coworkers observed by XPS that different amounts and species of nitrogen-containing surface groups are obtained by HNO_3 treatment of olive stones-based activated carbon depending on the activation method. Chemical activation by H_3PO_4 forms a larger amount of N-containing surface groups, mainly as nitro groups, compared to physical activation with CO_2, whereby only less oxidized nitrogen species are formed. They concluded that the phosphorous species in the carbons could be responsible for the examined difference.[129]

X-ray diffraction (XRD)

X-ray diffraction gives information on the crystallinity or amorphicity of activated carbons. Comparison of resulting XRD patterns with the crystallographic databases clarify that partially graphitic structures are available in the activated carbon materials. In addition, XRD can be used for investigations of the activation process by detecting crystalline intermediates of the activation reagents.

Liang and coworkers found in the activated carbon prepared by microwave-induced $ZnCl_2$ activation of wood broad peaks at about 23° and 44° due to the (002) and (100) reflexes of graphite. Thus, they concluded the formation of a carbon structure with randomly orientated graphitic carbon layers. Calculation of *d*-values by the Bragg equation allows the comparison of the layer distances found in the activated carbon samples with the values of graphite (0.335 nm). The prepared wood-based activated carbon shows higher *d*-values between 0.365 nm and 0.375 nm.[104] Singh *et al.* received very similar results by KOH activation of biomass *Arundo donax* with broad peaks at 23° and 43°. Moreover, they found that the intensity of the reflections are enhanced by an increasing KOH to biomass ratio, indicating that KOH promotes the graphitization of the prepared activated carbons.[113] Díaz-Terán *et al.* used XRD to detect the development of crystalline compounds during the activation of a lignocellulosic precursor with KOH. They found the formation of K_2CO_3 during this step, which increases with the pyrolysis temperature and is responsible for the pore development.[130]

Thermogravimetric analysis (TGA)

TGA provides information on the weight loss of the starting materials during the heating process due to *e.g.* decomposition.

Kumar *et al.* found by using TGA that the activation process of the used nutshells by $ZnCl_2$ proceeds in three steps. In the beginning, the organic matter decomposes, followed by a further decomposition of the obtained intermediates and the activating reagent. At least, the char reacts with $ZnCl_2$ and the pores open.[132] Kalderis and coworkers observed also three steps in the study of the thermal behavior of rise husk and bagasse. The first step (~100 °C) shows a weight loss due to the moisture of the samples. Further heating to about 370 °C leads to decomposition of the main components cellulose, hemicellulose and lignin and the loss of the volatile matter is responsible for the decrease in weight. Higher temperatures results in carbonization of the residues and gaseous products or tars are formed associated with another weight loss.[30]

Ash content

The total ash content is determined by using ASTM standards. A defined amount of sample is weighed in a porcelain basin, heated in a muffle furnace to a given final temperature and for a certain time. After cooling to room temperature in a desiccator, the sample is reweighed. The ash content is calculated using the following equation:

Ash content [%] = remaining solids weight [g] / original materials weight [g] * 100 [30, 50]

1.6 Metal loading methods

The macroscopic distribution of a metal on the support, the size of the metal crystallites on the support surface and the oxidation state of the metal species determine the catalytic performance of a supported metal catalyst.

The most used preparation techniques for metal loading on carbon support are ionic adsorption, colloid deposition and electroless plating or mixtures of these methods. Uniformly impregnated catalysts are produced by adsorption of an ionic metal species *e.g.* $[Pd(OH)_4]^{2-}$ or $[PtCl_6]^{2-}$ on the carbon support via functional groups on the surface and in the pores, which is greatly affected by the pH of the solutions.[1, 133] Egg-shell impregnated catalysts are prepared by deposition of a metal colloid (preformed or *in situ* generated) on the surface and macropores of the support. The egg-shell distribution is caused by the size of the colloid particles, whereby the inner pore system of the support is not or only very limited accessible.[1, 134] Deposition of the metal atoms on the carbon support by electroless plating occurs via a redox mechanism and can be achieved by adding a reducing agent.[1, 135] Finally, a reduction step is necessary to form the active metal on carbon catalysts by adding a reducing agent, such as hydrogen, formaldehyde or sodium borohydride, after the impregnation step.[1]

1.7 Conclusion

Each step in the preparation of a carbon-supported catalyst influences its final properties such as the surface area, the pore size distribution, the attrition resistance, the ash content and the surface chemistry of the carbon materials, and thus the performance of the catalyst.[1]

- The choice of starting material influences the particle size distribution, morphology and the attrition resistance of the carbon material. These properties determine the filterability and activity of the prepared supported metal catalysts. A smaller particle size leads to an increased geometrical area, and thus to a higher catalytic activity of the catalyst, while larger particles enhance the filterability of the materials during catalyst recycling.[1]
- The pore size distribution of the carbon-based supports, influenced by the precursor material and the preparation and activation techniques used, determines the available surface area for the impregnation with catalytically active metal particles. In addition,

the porosity influences the access of reactants to the active supported metal particles, thereby affecting the catalytic activity.[1, 136]

- The surface chemistry, in particular oxygen-containing surface groups of the activated carbon support, influences the preparation of the catalyst and the resulting activity. The oxygen functionalities determine the acid-base character for adsorption of ionic species or the redox properties of the materials for deposition of the metal particles by redox reaction with carbon. Acidic oxygen functional groups (carboxyl or lactone groups) reduce the hydrophobicity of the carbon and thereby increase the surface accessibility to the aqueous metal precursor solution. Moreover, they ensure highly dispersed metal crystallites and stabilize them.[1, 137-139]

Nevertheless, a rational design of carbon-supported catalyst materials is still difficult. Empiricism, experience and precise procedures in practical production are important elements for the preparation of active, stable and reproducible heterogeneous supported catalysts.

1.8 References

[1] E. Auer, A. Freund, J. Pietsch, T. Tacke, *Applied Catalysis A: General* **1998**, *173*, 259-271.

[2] F. Rodŕíguez-Reinoso, A. Seṕulveda-Escribano, in *Carbon Materials for Catalysis*, **2008**, pp. 131-155.

[3] T. M. Alslaibi, I. Abustan, M. A. Ahmad, A. A. Foul, *Journal of Chemical Technology & Biotechnology* **2013**, *88*, 1183-1190.

[4] M. J. Munoz-Guillena, M. J. Illan-Gomez, J. M. Martin-Martinez, A. Linares-Solano, C. Salinas-Martinez de Lecea, *Energy & Fuels* **1992**, *6*, 9-15.

[5] R. Pietrzak, H. Wachowska, P. Nowicki, *Energy & Fuels* **2006**, *20*, 1275-1280.

[6] L.-Y. Hsu, H. Teng, *Fuel Processing Technology* **2000**, *64*, 155-166.

[7] J. Yang, L. Yue, B. Lin, L. Wang, Y. Zhao, Y. Lin, K. Chang, H. DaCosta, X. Hu, *Energy & Fuels* **2017**, *31*, 11060-11068.

[8] M. A. Lillo-Ródenas, D. Cazorla-Amorós, A. Linares-Solano, *Carbon* **2003**, *41*, 267-275.

[9] A. Perrin, A. Celzard, A. Albiniak, J. Kaczmarczyk, J. F. Marêché, G. Furdin, *Carbon* **2004**, *42*, 2855-2866.

[10] R. Pietrzak, *Fuel* **2009**, *88*, 1871-1877.

[11] R. Pietrzak, K. Jurewicz, P. Nowicki, K. Babeł, H. Wachowska, *Fuel* **2007**, *86*, 1086-1092.

[12] R. Pietrzak, H. Wachowska, P. Nowicki, K. Babeł, *Fuel Processing Technology* **2007**, *88*, 409-415.

[13] M. A. Lillo-Ródenas, D. Cazorla-Amorós, A. Linares-Solano, F. Béguin, C. Clinard, J. N. Rouzaud, *Carbon* **2004**, *42*, 1305-1310.

[14] M. A. Lillo-Ródenas, J. Juan-Juan, D. Cazorla-Amorós, A. Linares-Solano, *Carbon* **2004**, *42*, 1371-1375.

[15] L. Khezami, A. Chetouani, B. Taouk, R. Capart, *Powder Technology* **2005**, *157*, 48-56.

[16] Suhas, V. K. Gupta, P. J. M. Carrott, R. Singh, M. Chaudhary, S. Kushwaha, *Bioresource Technology* **2016**, *216*, 1066-1076.

[17] Suhas, P. J. M. Carrott, M. M. L. Ribeiro Carrott, *Bioresource Technology* **2007**, *98*, 2301-2312.

[18] K. Y. Foo, B. H. Hameed, *Bioresource Technology* **2012**, *111*, 425-432.

[19] O. Ioannidou, A. Zabaniotou, *Renewable and Sustainable Energy Reviews* **2007**, *11*, 1966-2005.

[20] A. Jain, R. Balasubramanian, M. P. Srinivasan, *Chemical Engineering Journal* **2016**, *283*, 789-805.

[21] R. Hoseinzadeh Hesas, W. M. A. Wan Daud, J. N. Sahu, A. Arami-Niya, *Journal of Analytical and Applied Pyrolysis* **2013**, *100*, 1-11.

[22] M. A. Yahya, Z. Al-Qodah, C. W. Z. Ngah, *Renewable and Sustainable Energy Reviews* **2015**, *46*, 218-235.

[23] Y. Chen, Y. Zhu, Z. Wang, Y. Li, L. Wang, L. Ding, X. Gao, Y. Ma, Y. Guo, *Advances in Colloid and Interface Science* **2011**, *163*, 39-52.

[24] P. González-García, *Renewable and Sustainable Energy Reviews* **2018**, *82*, 1393-1414.

[25] X. Li, C. Han, X. Chen, C. Shi, *Microporous and Mesoporous Materials* **2010**, *131*, 303-309.

[26] P. Gao, Z.-h. Liu, G. Xue, B. Han, M.-h. Zhou, *Bioresource Technology* **2011**, *102*, 3645-3648.

[27] V. Fierro, G. Muñiz, A. H. Basta, H. El-Saied, A. Celzard, *Journal of Hazardous Materials* **2010**, *181*, 27-34.

[28] Q. Miao, Y. Tang, J. Xu, X. Liu, L. Xiao, Q. Chen, *Journal of the Taiwan Institute of Chemical Engineers* **2013**, *44*, 458-465.

[29] C. Qin, Y. Chen, J.-m. Gao, *Materials Letters* **2014**, *135*, 123-126.

[30] D. Kalderis, S. Bethanis, P. Paraskeva, E. Diamadopoulos, *Bioresource Technology* **2008**, *99*, 6809-6816.

[31] P. K. Malik, *Dyes and Pigments* **2003**, *56*, 239-249.

[32] N. Yalçın, V. Sevinç, *Carbon* **2000**, *38*, 1943-1945.

[33] K. Le Van, T. T. Luong Thi, *Progress in Natural Science: Materials International* **2014**, *24*, 191-198.

[34] H. Demiral, G. Gündüzoğlu, *Bioresource Technology* **2010**, *101*, 1675-1680.

[35] M. Valix, W. H. Cheung, G. McKay, *Chemosphere* **2004**, *56*, 493-501.

[36] E. C. Bernardo, R. Egashira, J. Kawasaki, *Carbon* **1997**, *35*, 1217-1221.

[37] K. J. Cronje, K. Chetty, M. Carsky, J. N. Sahu, B. C. Meikap, *Desalination* **2011**, *275*, 276-284.

[38] R. Michel, N. Mischler, B. Azambre, G. Finqueneisel, J. Machnikowski, P. Rutkowski, T. Zimny, J. V. Weber, *Environmental Chemistry Letters* **2006**, *4*, 185-189.

[39] T. Shim, J. Yoo, C. Ryu, Y.-K. Park, J. Jung, *Bioresource Technology* **2015**, *197*, 85-90.

[40] Q.-S. Liu, T. Zheng, P. Wang, L. Guo, *Industrial Crops and Products* **2010**, *31*, 233-238.

[41] B. H. Hameed, A. T. M. Din, A. L. Ahmad, *Journal of Hazardous Materials* **2007**, *141*, 819-825.

[42] C.-S. Yang, Y. S. Jang, H. K. Jeong, *Current Applied Physics* **2014**, *14*, 1616-1620.

[43] Z. Jieying, Q. Zhao, Z. Ye, *Applied Surface Science* **2014**, *299*, 86-91.

[44] H. Deng, G. Zhang, X. Xu, G. Tao, J. Dai, *Journal of Hazardous Materials* **2010**, *182*, 217-224.

[45] Ö. Şahin, C. Saka, *Bioresource Technology* **2013**, *136*, 163-168.

[46] C. Saka, *Journal of Analytical and Applied Pyrolysis* **2012**, *95*, 21-24.

[47] A. Ahmadpour, D. D. Do, *Carbon* **1997**, *35*, 1723-1732.

[48] A. C. Lua, T. Yang, *Journal of Colloid and Interface Science* **2004**, *274*, 594-601.

[49] R. Pietrzak, P. Nowicki, J. Kaźmierczak, I. Kuszyńska, J. Goscianska, J. Przepiórski, *Chemical Engineering Research and Design* **2014**, *92*, 1187-1191.

[50] Ç. d. Şentorun-Shalaby, M. G. Uçak-Astarlıogˇlu, L. Artok, Ç. Sarıcı, *Microporous and Mesoporous Materials* **2006**, *88*, 126-134.

[51] A. Aygün, S. Yenisoy-Karakaş, I. Duman, *Microporous and Mesoporous Materials* **2003**, *66*, 189-195.

[52] P. Nowicki, J. Kazmierczak, R. Pietrzak, *Powder Technology* **2015**, *269*, 312-319.

[53] C. Bouchelta, M. S. Medjram, O. Bertrand, J.-P. Bellat, *Journal of Analytical and Applied Pyrolysis* **2008**, *82*, 70-77.

[54] S. Uçar, M. Erdem, T. Tay, S. Karagöz, *Applied Surface Science* **2009**, *255*, 8890-8896.

[55] M. Al Bahri, L. Calvo, M. A. Gilarranz, J. J. Rodriguez, *Chemical Engineering Journal* **2012**, *203*, 348-356.

[56] I. Okman, S. Karagöz, T. Tay, M. Erdem, *Applied Surface Science* **2014**, *293*, 138-142.

[57] M. E. Fernandez, G. V. Nunell, P. R. Bonelli, A. L. Cukierman, *Industrial Crops and Products* **2014**, *62*, 437-445.

[58] D. Prahas, Y. Kartika, N. Indraswati, S. Ismadji, *Chemical Engineering Journal* **2008**, *140*, 32-42.

[59] K. Y. Foo, B. H. Hameed, *Microporous and Mesoporous Materials* **2012**, *148*, 191-195.

[60] M. J. Prauchner, F. Rodríguez-Reinoso, *Microporous and Mesoporous Materials* **2012**, *152*, 163-171.

[61] Z. Hu, M. P. Srinivasan, *Microporous and Mesoporous Materials* **1999**, *27*, 11-18.

[62] Y. L. Tan, M. A. Islam, M. Asif, B. H. Hameed, *Energy* **2014**, *77*, 926-931.

[63] L. Yue, Q. Xia, L. Wang, L. Wang, H. DaCosta, J. Yang, X. Hu, *Journal of Colloid and Interface Science* **2018**, *511*, 259-267.

[64] S. Román, J. F. González, C. M. González-García, F. Zamora, *Fuel Processing Technology* **2008**, *89*, 715-720.

[65] S. M. Yakout, G. Sharaf El-Deen, *Arabian Journal of Chemistry* **2016**, *9*, S1155-S1162.

[66] M. L. Martínez, M. M. Torres, C. A. Guzmán, D. M. Maestri, *Industrial Crops and Products* **2006**, *23*, 23-28.

[67] K. Y. Foo, B. H. Hameed, *Bioresource Technology* **2011**, *102*, 9794-9799.

[68] S. Deng, B. Hu, T. Chen, B. Wang, J. Huang, Y. Wang, G. Yu, *Adsorption* **2015**, *21*, 125-133.

[69] V. Boonamnuayvitaya, S. Sae-ung, W. Tanthapanichakoon, *Separation and Purification Technology* **2005**, *42*, 159-168.

[70] S. M. Lamine, C. Ridha, H.-M. Mahfoud, C. Mouad, B. Lotfi, A. H. Al-Dujaili, *Energy Procedia* **2014**, *50*, 393-400.

[71] M. Song, B. Jin, R. Xiao, L. Yang, Y. Wu, Z. Zhong, Y. Huang, *Biomass and Bioenergy* **2013**, *48*, 250-256.

[72] A.-N. A. El-Hendawy, *Carbon* **2003**, *41*, 713-722.

[73] D. Adinata, W. M. A. Wan Daud, M. K. Aroua, *Bioresource Technology* **2007**, *98*, 145-149.

[74] I. A. W. Tan, A. L. Ahmad, B. H. Hameed, *Desalination* **2008**, *225*, 13-28.

[75] J. Guo, A. C. Lua, *Microporous and Mesoporous Materials* **1999**, *32*, 111-117.

[76] L. Yue, L. Rao, L. Wang, L. Wang, J. Wu, X. Hu, H. DaCosta, J. Yang, M. Fan, *Industrial & Engineering Chemistry Research* **2017**, *56*, 14115-14122.

[77] S. Zhang, M. S. Miran, A. Ikoma, K. Dokko, M. Watanabe, *Journal of the American Chemical Society* **2014**, *136*, 1690-1693.

[78] N. Fechler, T.-P. Fellinger, M. Antonietti, *Advanced Materials* **2013**, *25*, 75-79.

[79] M. Iwanow, J. Finkelmeyer, A. Söldner, M. Kaiser, T. Gärtner, V. Sieber, B. König, *Chemistry – A European Journal* **2017**, *23*, 12467-12470.

[80] H. Xu, J. Guo, K. S. Suslick, *Advanced Materials* **2012**, *24*, 6028-6033.

[81] M. A. F. Mazlan, Y. Uemura, S. Yusup, F. Elhassan, A. Uddin, A. Hiwada, M. Demiya, *Procedia Engineering* **2016**, *148*, 530-537.

[82] G. Tzvetkov, S. Mihaylova, K. Stoitchkova, P. Tzvetkov, T. Spassov, *Powder Technology* **2016**, *299*, 41-50.

[83] Z. Phiri, R. C. Everson, H. W. J. P. Neomagus, B. J. Wood, *Journal of Analytical and Applied Pyrolysis* **2017**, *125*, 127-135.

[84] A. Dufour, A. Celzard, V. Fierro, E. Martin, F. Broust, A. Zoulalian, *Applied Catalysis A: General* **2008**, *346*, 164-173.

[85] A. Ahmadpour, D. D. Do, *Carbon* **1996**, *34*, 471-479.

[86] A. Mohammad-Khah, R. Ansari, *International Journal of ChemTech Research* **2009**, *1*, 859-864.

[87] F. Rodríguez-Reinoso, M. Molina-Sabio, M. T. González, *Carbon* **1995**, *33*, 15-23.

[88] H. Kühl, M. M. Kashani-Motlagh, H. J. Mühlen, K. H. van Heek, *Fuel* **1992**, *71*, 879-882.

[89] G. Q. Lu, D. D. Do, *Carbon* **1992**, *30*, 21-29.

[90] K. Tomków, T. Siemieniewska, F. Czechowski, A. Jankowska, *Fuel* **1977**, *56*, 121-124.

[91] W. F. DeGroot, G. N. Richards, *Carbon* **1989**, *27*, 247-252.

[92] M. Wu, Q. Zha, J. Qiu, Y. Guo, H. Shang, A. Yuan, *Carbon* **2004**, *42*, 205-210.

[93] H. Marsh, F. Rodríguez-Reinoso, in *Activated Carbon* (Eds.: H. Marsh, F. Rodríguez-Reinoso), Elsevier Science Ltd, Oxford, **2006**, pp. 322-365.

[94] T.-P. Fellinger, A. Thomas, J. Yuan, M. Antonietti, *Advanced Materials* **2013**, *25*, 5838-5855.

[95] S. E. Skrabalak, K. S. Suslick, *Journal of the American Chemical Society* **2006**, *128*, 12642-12643.

[96] J. D. Atkinson, M. E. Fortunato, S. A. Dastgheib, M. Rostam-Abadi, M. J. Rood, K. S. Suslick, *Carbon* **2011**, *49*, 587-598.

[97] Y. Yan, F. Zhang, Y. Meng, B. Tu, D. Zhao, *Chemical Communications* **2007**, 2867-2869.

[98] A. J. Romero-Anaya, M. Ouzzine, M. A. Lillo-Ródenas, A. Linares-Solano, *Carbon* **2014**, *68*, 296-307.

[99] A. B. Fuertes, *Journal of Materials Chemistry* **2003**, *13*, 3085-3088.

[100] Y. Shin, L.-Q. Wang, I.-T. Bae, B. W. Arey, G. J. Exarhos, *The Journal of Physical Chemistry C* **2008**, *112*, 14236-14240.

[101] J. Ryu, Y.-W. Suh, D. J. Suh, D. J. Ahn, *Carbon* **2010**, *48*, 1990-1998.

[102] X. Sun, Y. Li, *Angewandte Chemie International Edition* **2004**, *43*, 597-601.

[103] J. Kazmierczak-Razna, P. Nowicki, R. Pietrzak, *Powder Technology* **2015**, *273*, 71-75.

[104] T. Wang, S. Tan, C. Liang, *Carbon* **2009**, *47*, 1880-1883.

[105] Y. Ji, T. Li, L. Zhu, X. Wang, Q. Lin, *Applied Surface Science* **2007**, *254*, 506-512.

[106] S. B. Lyubchik, R. Benoit, F. Béguin, *Carbon* **2002**, *40*, 1287-1294.

[107] S. Wang, G. Q. Lu, *Carbon* **1998**, *36*, 283-292.

[108] J. Jaramillo, P. M. Álvarez, V. Gómez-Serrano, *Fuel Processing Technology* **2010**, *91*, 1768-1775.

[109] W. Han, H. Liu, H. Zhu, *Catalysis Communications* **2007**, *8*, 351-354.

[110] J. L. Figueiredo, M. F. R. Pereira, M. M. A. Freitas, J. J. M. Órfão, *Carbon* **1999**, *37*, 1379-1389.

[111] G. Yang, H. Chen, H. Qin, Y. Feng, *Applied Surface Science* **2014**, *293*, 299-305.

[112] J. Chen, J. Yang, G. Hu, X. Hu, Z. Li, S. Shen, M. Radosz, M. Fan, *ACS Sustainable Chemistry & Engineering* **2016**, *4*, 1439-1445.

[113] G. Singh, I. Y. Kim, K. S. Lakhi, P. Srivastava, R. Naidu, A. Vinu, *Carbon* **2017**, *116*, 448-455.

[114] M. S. Shafeeyan, W. M. A. W. Daud, A. Houshmand, A. Arami-Niya, *Applied Surface Science* **2011**, *257*, 3936-3942.

[115] C. Moreno-Castilla, M. A. Ferro-Garcia, J. P. Joly, I. Bautista-Toledo, F. Carrasco-Marin, J. Rivera-Utrilla, *Langmuir* **1995**, *11*, 4386-4392.

[116] K. S. Sing, D. H. Everett, R. A. Haul, L. Moscou, R. A. Pierotti, J. Rouquerol, T. Siemieniewska, in *Handbook of Heterogeneous Catalysis*, **2008**.

[117] S. Brunauer, P. H. Emmett, E. Teller, *Journal of the American Chemical Society* **1938**, *60*, 309-319.

[118] K. Sing, *Colloids and Surfaces A: Physicochemical and Engineering Aspects* **2001**, *187-188*, 3-9.

[119] M. M. Dubinin, *Carbon* **1989**, *27*, 457-467.

[120] E. P. Barrett, L. G. Joyner, P. P. Halenda, *Journal of the American Chemical Society* **1951**, *73*, 373-380.

[121] N. Setoyama, K. Kaneko, F. Rodriguez-Reinoso, *The Journal of Physical Chemistry* **1996**, *100*, 10331-10336.

[122] G. Sethia, A. Sayari, *Carbon* **2016**, *99*, 289-294.

[123] H. P. Boehm, *Carbon* **2002**, *40*, 145-149.

[124] T. Otowa, Y. Nojima, T. Miyazaki, *Carbon* **1997**, *35*, 1315-1319.

[125] C. Srinivasakannan, M. Zailani Abu Bakar, *Biomass and Bioenergy* **2004**, *27*, 89-96.

[126] P. Galiatsatou, M. Metaxas, D. Arapoglou, V. Kasselouri-Rigopoulou, *Waste Management* **2002**, *22*, 803-812.

[127] D. M. Nevskaia, A. Santianes, V. Muñoz, A. Guerrero-Ruíz, *Carbon* **1999**, *37*, 1065-1074.

[128] C. Pevida, M. G. Plaza, B. Arias, J. Fermoso, F. Rubiera, J. J. Pis, *Applied Surface Science* **2008**, *254*, 7165-7172.

[129] J. J. Ternero-Hidalgo, J. M. Rosas, J. Palomo, M. J. Valero-Romero, J. Rodríguez-Mirasol, T. Cordero, *Carbon* **2016**, *101*, 409-419.

[130] J. Díaz-Terán, D. M. Nevskaia, J. L. G. Fierro, A. J. López-Peinado, A. Jerez, *Microporous and Mesoporous Materials* **2003**, *60*, 173-181.

[131] H. Guedidi, L. Reinert, J.-M. Lévêque, Y. Soneda, N. Bellakhal, L. Duclaux, *Carbon* **2013**, *54*, 432-443.

[132] A. Kumar, H. Mohan Jena, *Applied Surface Science* **2015**, *356*, 753-761.

[133] K. Kyong Tae, C. Jong Shik, L. Kyung Hee, K. Young Gul, S. Joon Young, *Carbon* **1992**, *30*, 467-475.

[134] J. Qiu, H. Zhang, C. Liang, J. Li, Z. Zhao, *Chemistry – A European Journal* **2006**, *12*, 2147-2151.

[135] L.-M. Ang, T. S. A. Hor, G.-Q. Xu, C.-h. Tung, S. Zhao, J. L. S. Wang, *Chemistry of Materials* **1999**, *11*, 2115-2118.

[136] M. Gurrath, T. Kuretzky, H. P. Boehm, L. B. Okhlopkova, A. S. Lisitsyn, V. A. Likholobov, *Carbon* **2000**, *38*, 1241-1255.

[137] M. O. Corapcioglu, C. P. Huang, *Carbon* **1987**, *25*, 569-578.

[138] V. Z. Radkevich, T. L. Senko, K. Wilson, L. M. Grishenko, A. N. Zaderko, V. Y. Diyuk, *Applied Catalysis A: General* **2008**, *335*, 241-251.

[139] M. L. Toebes, J. A. van Dillen, K. P. de Jong, *Journal of Molecular Catalysis A: Chemical* **2001**, *173*, 75-98.

CHAPTER 2

2 Preparation of supported Palladium Catalysts using Deep Eutectic Solvents

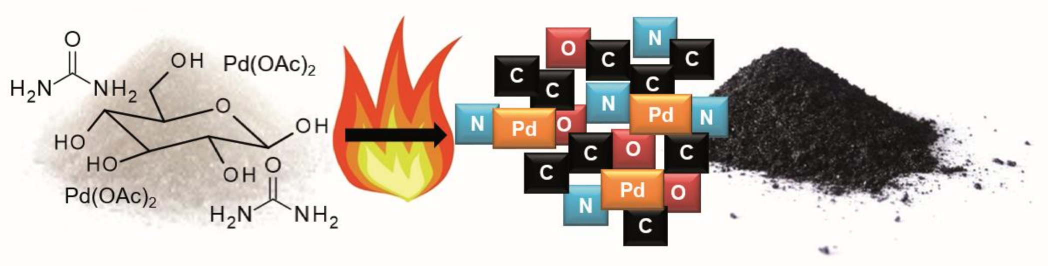

This chapter has been published as:

M. Iwanow, J. Finkelmeyer, A. Söldner, M. Kaiser, T. Gärtner, V. Sieber, B. König, *Chemistry – A European Journal* **2017**, *23*, 12467-12470.
- reproduced with permission of John Wiley & Sons.

MI carried out the synthesis of catalysts (parts during master thesis), characterization experiments and wrote the manuscript. JF performed during her Bachelor thesis under supervision of MI the experiments in Table 2.2 and parts of the unpublished results in 2.6 (2.6.1 - 2.6.3 and 2.6.4 activity test reactions and SEM). AS carried out the XRD measurements. TG, VS and BK supervised the project. BK is the corresponding author.

2.1 Introduction

Supported palladium catalysts, like palladium on activated carbon, find extensive use in chemical synthesis for a wide variety of reactions ranging from the reduction of alkynes, alkenes, aldehydes, ketones, nitro groups, nitriles and imines to carbon-carbon bond formation reactions like the Sonogashira, Heck or Suzuki cross coupling reactions.[1] Supporting materials, like activated carbon, are used for a fine distribution of metals on a large surface and for the stabilization of small metal particles.[2] Thereby, catalytically active atoms are better accessible than in comparable metal bulk materials.[3] Another advantage of activated carbon as a supporting material is the facile recovery and recycling of the precious metals by oxidation of the carbon after use.[4]

Conventionally, several steps are necessary for the preparation of these catalysts. The surface of the activated carbon produced by either steam or chemical activation, is loaded by ionic adsorption of a metal salt forming uniformly impregnated catalysts, which is subsequently dried and reduced to the metallic form.[2, 5]

We report here a simple single step method for the preparation of supported metal catalysts using deep eutectic solvents (DES). A great advantage over the conventional impregnation method is that all kinds of metal precursors or mixtures of them can be easily supported in different ratios. Moreover, the deep eutectic solvents can influence the properties of the supporting material. DES[6-7], which are defined as a fluid, composed of two or three components[8], which are able to self-associate by hydrogen bond interactions to form an eutectic mixture with a melting point lower than that of each individual component,[9] are prepared using cheap and abundant non-toxic starting materials.[10-12] The solubility of metal compounds, especially of metal oxides[13] and the fact that several DES show a high carbon content renders them well-suited starting materials for catalyst preparation. All components are stirred under heating to an adequate temperature until a homogeneous, clear liquid has formed.[14] This liquid serves as solvent for the palladium precursor and the subsequent pyrolysis of the mixture yields the active catalyst without further activation. Moreover, the prepared catalysts can be easily reused after a filtration and washing step (Table S2.1 and Figure S2.1 in Chapter 2.5). The supporting material (CNO) consists of carbon, nitrogen and oxygen, which is already loaded with the metal.[15]

2.2 Results and discussion

Our initial studies began with the preparation of a deep eutectic solvent consisting of 40 wt% D-glucose and 60 wt% urea, the dissolution of palladium(II) acetate in the mixture and the subsequent pyrolysis in a round-bottom flask (Figure 2.1a).

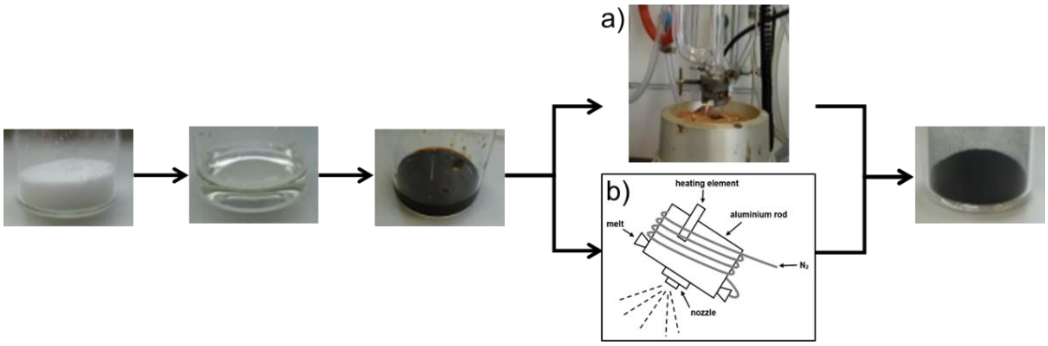

Figure 2.1. Overview of the preparation of supported palladium catalysts using DES: DES production, dissolution of $Pd(OAc)_2$, pyrolysis using the flask (a) or nozzle (b) method and finally, the Pd/CNO catalyst prepared.

To improve the relatively low active Pd/CNO catalyst obtained (Table 2.1, entry 2), a nebulization apparatus was constructed for the preparation of smaller particles, and thus of a larger surface (Figure 2.1b). This theory could be verified by BET measurements. The catalysts prepared by nozzle show a four times greater surface (38.89 ± 1.18 m^2 g^{-1}) compared to the catalysts produced by flask method (10.14 ± 0.48 m^2 g^{-1}), whereas the surface of a commercial activated carbon is still much higher (800 - 1200 m^2 g^{-1} [2]). Nevertheless, the activity to surface ratio is noticeably better. In the case of the catalyst prepared by nozzle, the time to reach complete conversion is only three times as high compared to a commercial Pd/C catalyst (10 wt% Pd loading, Sigma Aldrich); even though the surface of the supporting material was approximately 25 times lower (Figure 2.2 and Table S2.2, S2.3 and S2.4 in Chapter 2.5).

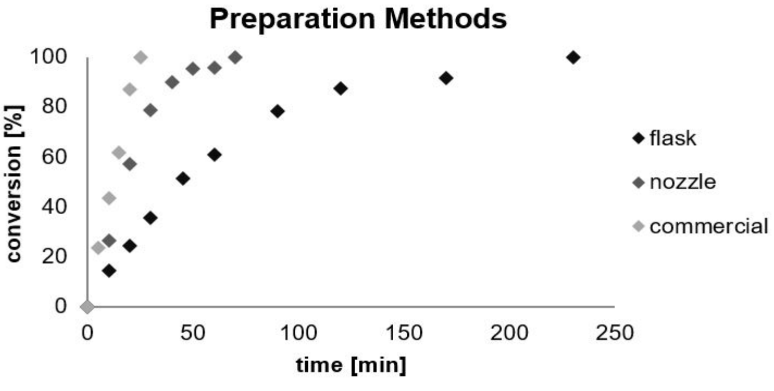

Figure 2.2. Activity comparison of a commercial catalyst Pd/C and the catalysts prepared by nozzle or flask method.

A strong dependency of the catalyst activity on the preparation temperature was determined as well. It could be shown that 440 °C was the optimum preparation temperature for the catalysts prepared by a urea - D-glucose DES for simple hydrogenation reactions with 1-dodecene **1** as test substrate (Table 2.1, Table S2.5 and Figure S2.2 in Chapter 2.5). A threefold faster conversion was observed using catalysts prepared by nozzle method at 440 °C compared to the catalyst prepared by flask method at a lower temperature (Entry 2).

Table 2.1. Comparison of catalysts prepared at different temperatures and by different methods. a) Conversion determined by GC-MS analysis; the reactions were carried out with 1 mmol 1-dodecene **1** and 25 mg catalyst in 5 mL MeOH.

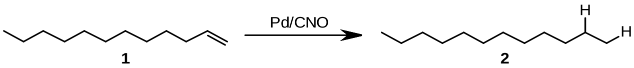

Entry	Conditions	Time [min]	Conversion [%]$^{a)}$
1	10 w% Pd/C (Sigma Aldrich), 1 mmol **1**	25	100
2	10 w% Pd, flask, 420 °C, 1 mmol **1**	230	100
3	10 w% Pd, nozzle, 250 °C, 1 mmol **1**	60	5
4	10 w% Pd, nozzle, 380 °C, 1 mmol **1**	90	36
5	10 w% Pd, nozzle, 420 °C, 1 mmol **1**	90	59
6	**10 w% Pd, nozzle, 440 °C, 1 mmol 1**	**70**	**100**
7	10 w% Pd, nozzle, 470 °C, 1 mmol **1**	90	94
8	10 w% Pd, nozzle, 500 °C, 1 mmol **1**	90	93

Additionally, a deep eutectic solvent dependency of the optimum preparation temperature for the catalysts was observed. In general, the preparation temperature for the catalysts with the highest activity ranged between 440 and 510 °C (Table 2.2 and S2.6 in Chapter 2.5).

Table 2.2. Overview of the DES dependent optimum preparation temperature.

DES system	Optimum temperature [°C]
choline chloride - D-sorbitol	470
choline chloride - vanillin	440
choline chloride - D-fructose	490
choline chloride - D-glucose	460
urea - D-glucose - D-fructose	470
urea - D-fructose	510
urea - D-glucose	440
N,N'-dimethylurea - vanillin	450
N,N'-dimethylurea - D-fructose	480
N,N'-dimethylurea - lignin	480

SEM-BSE investigations, indicated a better distribution of the palladium on the surface of the catalyst prepared by nozzle at 440 °C (Figure 2.3c) compared to the catalyst prepared at a lower temperature, shown in Figure 2.3b, or by flask method (Figure 2.3a), which explain the different activities of the catalysts.

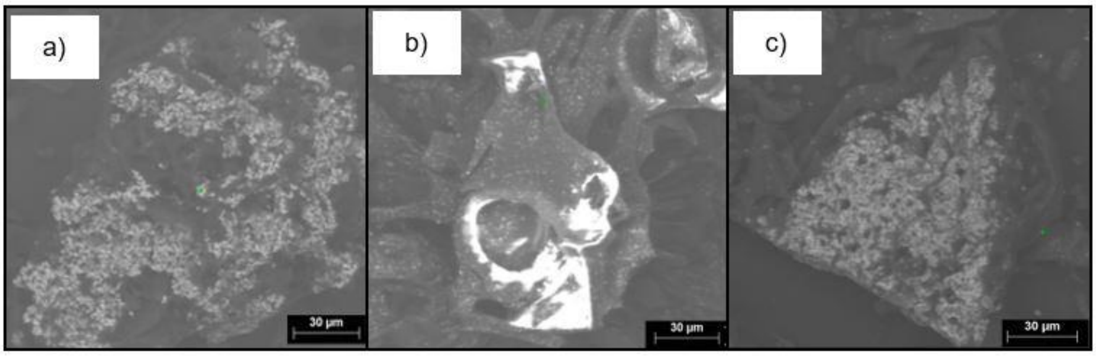

Figure 2.3. SEM investigation (BSE mode) of the Pd/CNO catalysts; a) prepared by flask; b) prepared by a nozzle at 420 °C c) prepared by nozzle at 440 °C.

This result was confirmed by X-ray photoelectron spectroscopy (XPS), whereby the metal loading on the surface of the catalysts was determined exemplarily for urea - D-fructose based catalysts (Figure 2.4 and Table S2.7 in Chapter 2.5) prepared by nozzle or flask method at the DES dependent optimum temperature 490 °C. The catalysts prepared by nozzle show with 13.5 wt% again a higher palladium amount, and thus a better distribution on the top surface layer, while 6.4 wt% palladium were found at the catalyst surface prepared by flask method.

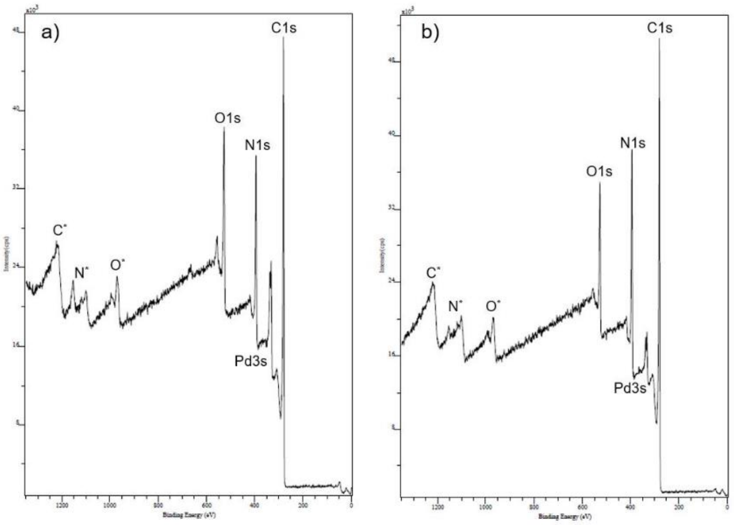

Figure 2.4. XPS analysis of urea - D-fructose based catalysts prepared by a) nozzle or b) flask method at 490 °C.

Considering the supporting material more precisely, SEM-EDX investigations and CHNS/O measurements offered different compositions based on the used DES and preparation temperature. The hydrogen bond acceptors (urea, N,N'-dimethylurea and choline chloride) influence the nitrogen content of the support, while the temperature affects the carbon content.

Table 2.3. Functional groups on the surface of the supporting material based on urea - ᴅ-glucose DES were determined by Boehm titrations.

		250 °C	380 °C	420 °C	440 °C	470 °C	500 °C
Round-bottom flask	n (basic) [µmol/g]	364.0	934.1	1023.2	968.5	967.7	899.0
	n (acidic) [µmol/g]	537.6	979.6	1083.8	1036.5	868.0	770.1
Nozzle	n (basic) [µmol/g]	404.6	1139.9	1121.8	1019.8	888.7	707.6
	n (acidic) [µmol/g]	227.3	1074.9	967.0	902.3	654.0	419.4
Com. activated carbon	n (basic) [µmol/g]	505.9					
	n (acidic) [µmol/g]	587.9					

The amount of functional groups on the surface of the supporting materials based on the urea - ᴅ-glucose DES were determined by Boehm titrations (Table 2.3).[16-17] For each preparation temperature of the supporting material, a different amount of functional groups is available. Using the nozzle method, for all temperatures the amount of basic groups is higher than the amount of acidic groups. Using the round-bottom flask method, this behavior can be observed only at higher temperatures (470 and 500 °C), while it is the other way around for temperatures up to 440 °C. Moreover, much more functional groups on the surface could be found in comparison to a commercially available activated carbon at temperatures above 300 °C.

Table 2.4. Reproducibility tests using urea - ᴅ-glucose based Pd/CNO prepared by nozzle at 440 °C.

Reproducibility	Conversion after 60 min
1st preparation	92 %
2nd preparation	96 %
3rd preparation	89 %

In addition, the preparation of the catalysts at different times using the same conditions give relevant information about the reproducibility of the method. The urea - D-glucose based Pd/CNO catalysts were prepared three times at 440 °C by nozzle and Table 2.4 shows, that it is possible to reproduce the catalyst activity using this method.

2.3 Conclusion

In conclusion, the reported protocol shows the preparation of Pd/CNO catalysts by a simple single step method based on deep eutectic solvents, to the best of our knowledge, for the first time. In contrast to the commercial Pd/C, the catalyst activity can be influenced by many preparation parameters regarding the desired application field. It has to be investigated, if the preparation temperature depends on the used substrates as well and a further characterization of the supporting material is necessary to understand the preparation mechanism in more detail.

2.4 Experimental section

2.4.1 Chemicals

Commercial reagents and used chemicals were purchased from Sigma Aldrich, Acros, TCI, VWR, Carl Roth, Merck or Alfa Aesar and used without further purification.

2.4.2 Preparation

Flask method

In a round-bottom flask equipped with a magnetic stirring bar, the DES used was heated until a clear, homogeneous liquid was formed. In this solvent, a known amount of metal salt for a theoretical 10 wt% loading was dissolved. As soon as the palladium salt was completely dissolved, the mixture was heated under nitrogen atmosphere until 280 °C until a dry porous material was formed. This material was further pyrolyzed in a muffle furnace at 440 °C under nitrogen atmosphere until a fine black powder rises.

Nozzle method

In a round-bottom flask equipped with a magnetic stirring bar, the DES used was heated until a clear, homogeneous liquid was formed. In this solvent, a known amount of metal salt for a theoretical 10 wt% loading was dissolved. As soon as the metal salt was completely dissolved, the mixture was transferred to a heated nebulization apparatus. By the use of nitrogen pressure, the mixture was sprayed on a heated surface and further pyrolyzed in a muffle furnace under nitrogen atmosphere at different temperatures until a fine black powder rises.

2.4.3 Characterization

Gas chromatography with mass spectrometry detector (GC-MS)

The conversion of the test reactions were determined by GC-MS using a BPX5 column (SGE, 30 m, I. D. 0.25 mm, film 0.25 µm) connected to a QP2010 Plus gas chromatograph with a Single Quad MS-detector (both Shimadzu, Japan) with helium as the carrier gas. 0.5 µL of the diluted sample was automatically injected via SSL-injector (290 °C) starting at 60 °C for 1 min, then heated to 170 °C at 11 °C min^{-1} and finally to 270 °C at 70 °C min^{-1} and held for 3 min.

Scanning electron microscopy (SEM)

Scanning electron microscopy (SEM) was performed to determine the morphologies of the supporting material (SE detector), the distribution of the palladium on the support (BSE detector) and the composition of the support with the EDX detector. The samples were mounted on carbon tape and studied using a digital scanning electron microscope (Zeiss, DSM 940 A, Oberkochen, Germany) and operated in secondary imaging mode at 20 kV with a working distance of 33.0 mm.

Powder diffractogram measurements (XRD)

Diffractogram measurements (XRD) were obtained by a general purpose X-ray diffractometer (Rigaku, MiniFlex 600, Tokyo, Japan) equipped with a high-speed one-dimensional detector (Rigaku, D/teX Ultra, Tokyo, Japan) and a $K\beta$ foil filter. XRD patterns were recorded over the 2θ range of 0° - 90°, with a step width of 0.02°, a scanning speed of 2° min^{-1} and a Cu-$K\alpha$ radiation generated at 40 kV and 15 mA. The measurements were analyzed by the Rigaku PDXL software (Integrated X-ray powder diffraction software).

Brunauer-Emmet-Teller measurements (BET)

The BET measurements were recorded on a Physisorption analyzer ASAP 2010 from Micromeritics.

2.4.4 Activity test reactions

In a 10 mL-round-bottom flask, 1 mmol (222 µL, 168.32 mg) of 1-dodecene was dissolved in 5 mL methanol and 25 mg (2.4 mol%, 0.024 mmol) of the different Pd/CNO catalysts were added. The mixture was stirred under hydrogen atmosphere at room temperature and the conversion was checked and proved by GC-MS by frequent sampling for two hours. To compare the activity of the catalysts, one sample was tested using a commercial Pd/C catalyst (10 wt% Pd, Sigma Aldrich) with the same conditions.

2.5 Supporting information

Table S2.1. Reusability of a Pd/CNO catalyst prepared at 440 °C.

Pd/CNO							
Time [min]	0	15	30	45	60	75	90
1-Dodecene [%]	100	55.9	9.0	0	0	0	0
Dodecane [%]	0	22.8	46.8	60.8	76	84.9	91.8
Isomers [%]	0	21.3	44.2	39.2	24	15.1	8.2
Pd/CNO (recycled)							
Time [min]	0	15	30	45	60	75	90
1-Dodecene [%]	100	48.8	10.4	0	0	0	0
Dodecane [%]	0	27.8	50.0	63.6	71.2	79.6	87.5
Isomers [%]	0	23.4	39.6	36.4	28.8	20.4	12.5
Pd/CNO (2nd time recycled)							
Time [min]	0	15	30	45	60	75	90
1-Dodecene [%]	100	60.3	23.9	5.7	0	0	0
Dodecane [%]	0	20.6	38.4	50.3	59.6	70.7	80.1
Isomers [%]	0	19.1	37.7	44	40.4	29.3	19.9

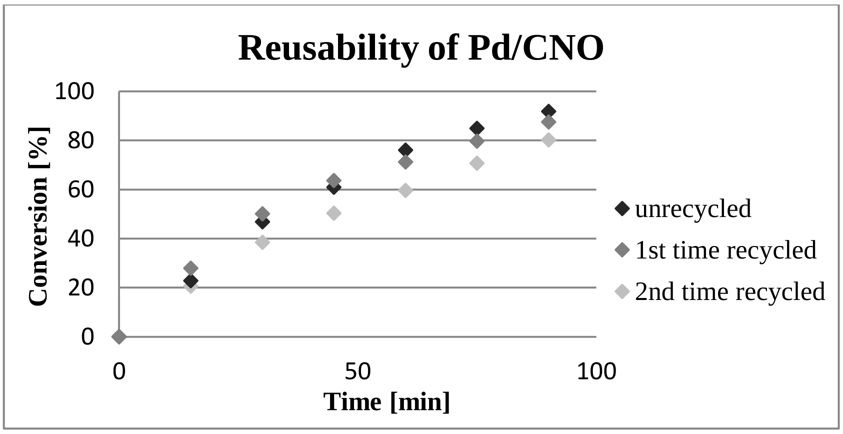

Figure S2.1. Reusability of a Pd/CNO catalyst prepared at 440 °C.

Table S2.2. Conversion of the catalyst prepared by round-bottom flask determined by GC-MS.

Conversion Pd/CNO (round-bottom flask)										
Time [min]	0	10	20	30	45	60	90	120	170	230
1-Dodecene [%]	100	65.8	43.9	21.7	0	0	0	0	0	0
Dodecane [%]	0	14.3	24.4	35.6	51.3	60.9	78.3	87.4	91.5	100
Isomers [%]	0	19.9	31.7	42.7	48.7	39.1	21.7	12.6	8.5	0

Table S2.3. Conversion of the catalyst prepared by nozzle at 440 °C determined by GC-MS.

Conversion Pd/CNO (nozzle 440 °C)								
Time [min]	0	10	20	30	40	50	60	70
1-Dodecene [%]	100	26.6	6.8	0	0	0	0	0
Dodecane [%]	0	26.7	57.2	78.6	89.9	95.4	95.9	100
Isomers [%]	0	46.7	36.0	21.4	10.1	4.6	4.1	0

Table S2.4. Conversion of the commercial palladium on activated carbon catalysts determined by GC-MS.

Conversion of commercial Pd/C						
Time [min]	0	5	10	15	20	25
1-Dodecene [%]	100	36.0	0	0	0	0
Dodecane [%]	0	23.8	43.7	61.9	87.0	100
Isomers [%]	0	40.2	56.3	38.1	13.0	0

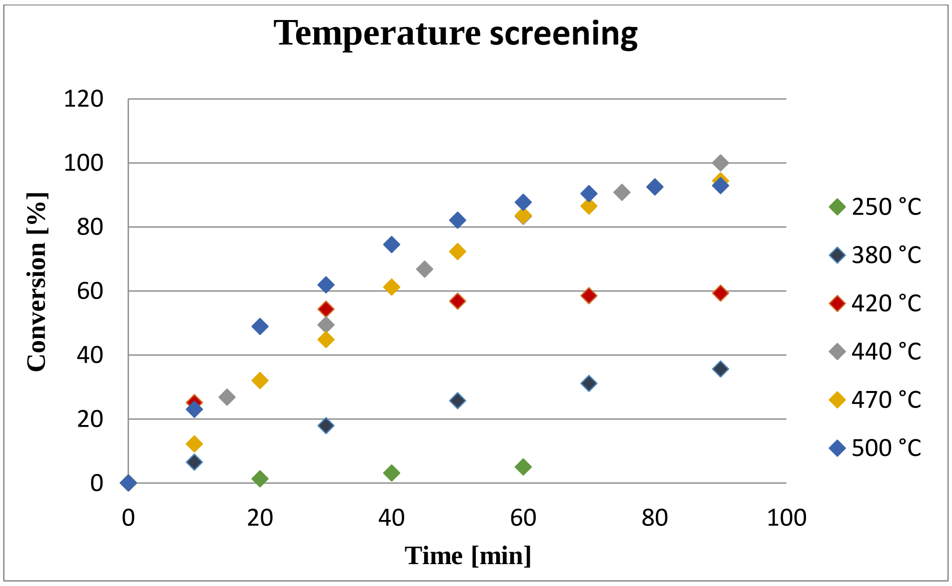

Figure S2.2. Conversions of the catalysts prepared by nozzle at different temperatures determined by GC-MS.

Table S2.5. Conversion of 1-dodecene [%] determined by GC-MS of the Pd/CNO catalysts prepared by nozzle at different temperatures.

Temperature Screening													
time [min]	**0**	**10**	**15**	**20**	**30**	**40**	**45**	**50**	**60**	**70**	**75**	**80**	**90**
250 °C	0	-	-	1.3	-	3.1	-	-	5.0	-	-	-	
380 °C	0	6.5	-	-	17.9	-	-	25.7	-	31.1	-	-	35.6
420 °C	0	25.1	-	-	54.3	-	-	56.8	-	58.5	-	-	59.3
440 °C	0	-	26.8	-	49.4	-	66.8	-	83.3	-	90.8	-	100
470 °C	0	12.2	-	32.0	44.8	61.2	-	72.3	83.6	86.5	-	92.5	94.4
500 °C	0	23.0	-	48.9	61.9	74.5	-	82.1	87.7	90.4	-	92.5	92.9

Table S2.6. Comparison of the catalysts prepared using different DES systems at 440 °C and the DES dependent optimum temperature.

Parameters	**Conversion after 90 min [%]**
choline chloride (1) : D-glucose (2)	
F + MF 440 °C	72.0
F + MF 460 °C	100 (75 min)
N,N'-dimethylurea (3) : D-fructose (1)	
F + MF 440 °C	56.5
F + MF 480 °C	98.4
choline chloride (1) : D-fructose (2)	
F + MF 440 °C	17.7
F + MF 490 °C	100
urea (4) : D-fructose (1)	
F + MF 440 °C	86.5
F + MF 510 °C	100 (75 min)
choline chloride (1) : D-sorbitol (1)	
F + MF 440 °C	59.1
F + MF 470 °C	18.2
choline chloride (1) : vanillin (2)	
F + MF 440 °C	90.9
N,N'-dimethylurea (4) : vanillin (5)	
F + MF 445 °C	91.8
F + MF 450 °C	100 (75 min)
Urea (18) : D-glucose (11) : D-fructose (11)	
F + MF 440 °C	78.9
F + MF 470 °C	99.0
N,N'-dimethylurea (60 wt%) : lignin (40 wt%)	
F + MF 440 °C	0.0
F + MF 480 °C	91.3

Table S2.7. Surface composition of the supporting material determined by XPS measurements using catalysts prepared with the DES urea and D-fructose. (F = round-bottom flask, MF = muffle furnace, CF = calcination furnace, N = nozzle)

	Compositon of the elements in [mass%]												
Element E_B (eV)	**C7 292.6**	**C6 291.1**	**C5 289.7**	**C4 288.3**	**C3 286.9**	**C2 285.7**	**C1 284.6**	**O 531**	**N2 400.1**	**N1 398.5**	**Pd3 acetate**	**Pd2 oxide**	**Pd1 metal**
F+MF 440 °C	0.7	1.6	2.2	5.8	8.5	22.9	24.2	8.0	12.0	10.6	1.5	1.8	0.2
F+CF 440 °C	1.2	1.6	2.9	5.8	7.1	27.6	28.5	5.8	11.4	7.2	1.0	-	-
F+MF 490 °C	0.9	1.3	2.3	5.2	6.5	19.7	27.4	6.6	10.1	6.4	3.4	6.8	3.3
N+MF 490 °C	1.1	1.7	2.6	6.9	7.8	21.7	25.9	6.0	11.8	8.3	1.8	3.8	0.8

Procedure of the Boehm titrations (Table 2.3 in the communication):

For each experiment, 300 mg of the prepared CNO supporting materials were agitated in 10 mL of hydrochloric acid (0.05 M) and in 10 mL of sodium hydroxide solution (0.05 M) for 24 hours at 25 °C. After filtration of the mixture, the hydrochloric acid solution was directly titrated with sodium hydroxide solution (0.05 M) using an autotitrator system after a saturation time of 2 hours in the presence of nitrogen. To the sodium hydroxide solution, 20 mL of hydrochloric acid (0.05 M) were added and the solution was saturated for 2 h with nitrogen followed by a back-titration with the 0.05 M sodium hydroxide solution.[13]

Composition of the different supporting materials prepared by different DES systems:

Table S2.8. Composition of the supporting materials of different DES at 440 °C.

DES System	**C [wt%]**	**N [wt%]**	**H [wt%]**	**O bzw. Cl [wt%]**
choline chloride - D-sorbitol	83.3	5.6	4.0	7.1
choline chloride - vanillin	73.7	1.0	3.1	22.2
choline chloride - D-fructose	82.1	2.8	4.0	11.1
choline chloride - D-glucose	81.2	2.5	4.0	12.3
urea - D-glucose - D-fructose	67.2	16.5	4.1	12.2
urea - D-fructose	61.3	20.5	3.3	14.9
urea - D-glucose	60.3	20.8	3.4	15.5
N,N'-dimethylurea - vanillin	77.4	3.5	3.7	15.4
N,N'-dimethylurea - D-fructose	71.3	13.9	4.2	10.6
N,N'-dimethylurea - lignin	75.0	6.5	3.6	14.9

2.6 Additional results - Different deep eutectic solvents for the Pd/CNO catalyst preparation

2.6.1 New deep eutectic solvents

Starting materials with a total amount of 2 mmol were measured according to the ratios shown in Table A2.1 and A2.2. For the screening of the N,N´-dimethylurea and lignin mixture, mass ratios and a total amount of 200 mg were used, since no molar mass for lignin is known (Table A2.3). The compounds were transferred to small glass vials and placed in a metal block thermostat. The melting points of the mixtures were determined by gradually increasing the temperature by 10 °C.

The novel mixtures should consist of carbon-rich starting materials in order to use them for catalyst preparation, since a larger amount of supporting material is formed during pyrolysis. Therefore, the mixtures with comparably low melting points and high ratios of the carbon-rich starting materials were chosen for the pyrolysis investigations (green marked in Table A2.1, A2.2 and A2.3).

Table A2.1. Screening of different molar ratios of N,N´-dimethylurea and vanillin and the resulting melting points.

New DES	**Molar ratio [mmol]**	***T_m* [°C]**
N,N‘-dimethylurea - vanillin	9:2	90
N,N‘-dimethylurea - vanillin	4:1	90
N,N‘-dimethylurea - vanillin	3:1	80
N,N‘-dimethylurea - vanillin	2:1	80
N,N‘-dimethylurea - vanillin	5:4	60
N,N‘-dimethylurea - vanillin	1:1	50
N,N‘-dimethylurea - vanillin	4:5	60
N,N‘-dimethylurea - vanillin	2:3	80
N,N‘-dimethylurea - vanillin	4:7	80
N,N‘-dimethylurea - vanillin	1:2	80
N,N‘-dimethylurea - vanillin	4:9	80
N,N‘-dimethylurea - vanillin	2:5	80

Table A2.2. Screening of different molar ratios of urea, D-glucose and D-fructose and the resulting melting points.

New DES	Molar ratio [mmol]	T_m [°C]
urea - D-glucose - D-fructose	8:1:1	>100
urea - D-glucose - D-fructose	7:1.5:1.5	100
urea - D-glucose - D-fructose	5:2.5:2.5	80
urea - D-glucose - D-fructose	4:3:3	80
urea - D-glucose - D-fructose	3:3.5:3.5	90
urea - D-glucose - D-fructose	2:4:4	100

Table A2.3. Screening of different weight ratios of N,N´-dimethylurea and lignin and the resulting melting points.

New DES	Mass ratio [wt%]	T_m [°C]
N,N‘-dimethylurea - lignin	99:1	>100
N,N‘-dimethylurea - lignin	97.5:2.5	>100
N,N‘-dimethylurea - lignin	95:5	>100
N,N‘-dimethylurea - lignin	92.5:7.5	>100
N,N‘-dimethylurea - lignin	87.5:12.5	>100
N,N‘-dimethylurea - lignin	80:20	>100
N,N‘-dimethylurea - lignin	70:30	100
N,N‘-dimethylurea - lignin	60:40	100
N,N‘-dimethylurea - lignin	50:50	100
N,N‘-dimethylurea - lignin	25:75	>100

2.6.2 Pyrolysis of several deep eutectic solvents

The starting materials were measured according to the ratios shown in Table A2.4. The composition of the novel deep eutectic solvents N,N'-dimethylurea - vanillin, N,N'-dimethylurea - lignin and urea - D-glucose - D-fructose were investigated by temperature screening as shown in Chapter 2.6.1, while all other molar ratios of the DES were found in a summary article published by Ruß *et al.*.[10]

The compounds were added in a 25 mL round-bottom flask and stirred at 110 °C until a clear homogenous liquid was formed. The mixture was heated under nitrogen atmosphere to 275 °C without stirring for one hour resulting in a dark brown liquid or a dry porous material. Further pyrolysis was done in a muffle furnace under nitrogen atmosphere up to 440 °C. The resulting supporting materials based on the different DES as starting materials are shown in Table A2.4. All DES, which produce more than 100 mg of CNO supporting material during the pyrolysis step (green marked), were used for the preparation of palladium catalysts Pd/CNO to investigate the influence of the different DES on the catalyst activity.

Table A2.4. Overview of the resulting pyrolysis amounts of different DES.

DES	Total amount of the mixture	Ratio	Resulting amount
choline chloride - oxalic acid	10 mmol	1:1	-
choline chloride - malonic acid	10 mmol	1:1	-
choline chloride - D-sorbitol (CS)	10 mmol	1:1	146.4 mg
choline chloride - D-fructose (CF)	10 mmol	1:2	429.1 mg
choline chloride - D-glucose (CG)	10 mmol	1:2	321.6 mg
choline chloride - urea	10 mmol	1:2	3.6 mg
choline chloride - vanillin (CV)	10 mmol	1:2	641.0 mg
choline chloride - D-mannitol	10 mmol	1:1	15.1 mg
choline chloride - N,N'-dimethylurea	10 mmol	1:2	-
N,N'-dimethylurea - D-fructose (DF)	10 mmol	3:1	117.3 mg
N,N'-dimethylurea - D-mannitol	10 mmol	5:3	17.3 mg
N,N'-dimethylurea - D-glucose	10 mmol	5:1	49.0 mg
N,N'-dimethylurea - D-sorbitol	10 mmol	3:1	10.4 mg
N,N'-dimethylurea - citric acid	10 mmol	7:2	-
N,N'-dimethylurea - vanillin (DV)	10 mmol	4:5	536.2 mg
N,N'-dimethylurea - lignin (DL)	-	60 wt%:40 wt%	204.7 mg
urea - D-fructose (UF)	10 mmol	4:1	152.7 mg
urea - D-glucose (UG)	10 mmol	9:2	111.3 mg
urea - D-galactose	10 mmol	7:1	86.1 mg
urea - D-sorbitol	10 mmol	3:1	51.4 mg
urea - D-glucose - D-fructose (UGF)	10 mmol	4.5:2.75:2.75	383.0 mg

2.6.3 Preparation of Pd/CNO catalysts

The catalysts were prepared using the round-bottom flask and nozzle method shown in Chapter 2.4.2.

Palladium catalysts for each DES were prepared by round-bottom flask method at 440 °C, followed by a temperature screening between 440 °C and 510 °C in steps of 10 °C. The screening was necessary to examine the DES dependent optimum preparation temperature. Finally, Pd/CNO catalysts were produced by nozzle method at the determined optimum temperature (Table 2.4 in Chapter 2.2).

2.6.4 Characterization of Pd/CNO catalysts

Activity test reactions and Brunauer-Emmet-Teller (BET) measurements

The activity test reactions and BET measurements of the different Pd/CNO catalysts were carried out as shown in Chapter 2.4.3 and 2.4.4.

An overview of the test reactions after 90 min using the Pd/CNO catalysts prepared by different DES, pyrolysis methods and pyrolysis temperatures are shown in Figure A2.1. The blue bars show the conversion of the catalysts prepared by round-bottom flask at 440 °C, while the red bars present the results of the catalysts produced at DES dependent optimum temperature using the same method. At least, the green bars show the turnover of the Pd/CNO prepared by nozzle method at the optimum temperature. Both, the pyrolysis temperature and method, influence significantly the activity of the catalysts. All catalysts prepared with the different DES can be tuned to a complete conversion (more than 98.9 %) after 90 minutes by using the optimum preparation conditions.

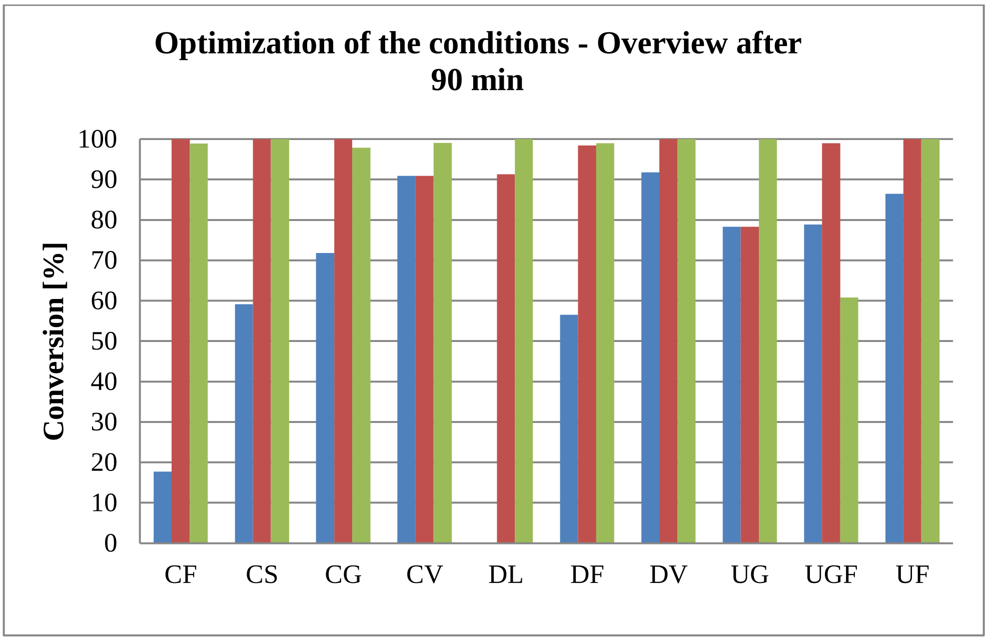

Figure A2.1. Overview of the activity test reactions of the Pd/CNO catalysts prepared by different DES, temperatures and different pyrolysis methods: flask at 440 °C (blue), flask at optimum temperature (red) and nozzle method at optimum temperature (green). C - choline chloride, D - N,N'-dimethylurea, U - urea, F - ᴅ-fructose, S - ᴅ-sorbitol, G - ᴅ-glucose, V - vanillin, L - lignin.

The results of the activity test reactions using the different prepared Pd/CNO catalysts are shown in Table A2.5 in detail. Catalysts prepared by the DES CG (75 min), DF (75 min), UF (75 min), CS (40 min), CV (60 min), DV (60 min) and DL (60 min) show already a complete conversion between 40 and 75 minutes. Nevertheless, a commercial palladium on carbon catalyst show a complete turnover after 25 minutes using the same conditions.

BET measurements of the DES based catalysts show significantly lower surface areas compared to commercial carbon catalysts. Thus, no correlations between the catalyst activity and surface area could be found, since catalysts with larger surfaces do not necessarily show higher activities. However, the activity of the catalysts prepared is only slightly worse compared to commercial catalysts with a distinctly larger surface area and the different supporting materials affect the catalyst activity, but the surface area is not the activity-determining factor.

Table A2.5. Characterization of the different catalysts prepared by activity test reactions, BET measurements and X-ray powder diffraction. a) Turnover determined by GC-MS; F = round-bottom flask, MF = muffle furnace, N = nozzle, - = not measured.

Preparation conditions	**Conversion after 90 min [%]a)**	**BET [m^2 g^{-1}]**
choline chloride (1) : D-glucose (2)		
F + MF 440 °C	72.0	16. 67 ± 0.15
F + MF 460 °C	100 (75 min)	-
N + MF 460 °C	97.9 (75 min)	145.16 ± 2.38
N,N'-dimethylurea (3) : D-fructose (1)		
F + MF 440 °C	56.5	1.00 ± 0.08
F + MF 480 °C	98.4	-
N + MF 480 °C	99.0 (75 min)	-
choline chloride (1) : D-fructose (2)		
F + MF 440 °C	17.7	47.59 ± 0.57
F + MF 490 °C	100	-
N + MF 490 °C	98.9	-
urea (4) : D-fructose (1)		
F + MF 440 °C	86.5	7.67 ± 0.09
F + MF 510 °C	100 (75 min)	30.80 ± 1.20
N + MF 510 °C	100	18.84 ± 0.65
choline chloride (1) : D-sorbitol (1)		
F + MF 440 °C	59.1	<1
F + MF 470 °C	18.2	-
N + MF 470 °C	99.1 (40 min)	-
choline chloride (1) : vanillin (2)		
F + MF 440 °C	90.9	18.62 ± 0.24
N + MF 440 °C	100 (60 min)	-
N + MF 430 °C	100 (60 min)	-
N,N'-dimethylurea (4) : vanillin (5)		
F + MF 445 °C	91.8	26.45 ± 0.38

F + MF 450 °C	100 (75 min)	20.48 ± 0.18
N + MF 450 °C	100 (60 min)	-
urea (18) : D-glucose (11) : D-fructose (11)		
F + MF 440 °C	78.9	5.00 ± 0.08
F + MF 470 °C	99.0	-
N + MF 470 °C	60.8	32.02 ± 0.31
N,N'-dimethylurea (60 wt%) : lignin (40 wt%)		
F + MF 440 °C	0.0	-
F + MF 480 °C	91.3	2.62 ± 0.34
N + MF 480 °C	100 (60 min)	43.33 ± 0.44

Scanning electron microscopy (SEM)

Comparing the different pyrolysis methods exemplarily for the catalysts based on the DES CV and pyrolyzed at 440 °C, a significant influence of the used pyrolysis method on the particle size of the catalysts could be determined. An inhomogeneous size distribution of the particles prepared by round-bottom flask (Figure A2.2b) was found. In contrast, the material prepared by nozzle shows a more homogeneous distribution with a smaller particle size and a more porous surface (Figure A2.2a). Distribution of palladium on the surface of the catalyst was investigated by back-scattered electron (BSE) detector. By using the nozzle method, a better distribution of palladium on the surface (Figure A2.2c) was found compared to the catalyst prepared by round-bottom flask method (Figure A2.2d). The improved distribution of palladium on the catalyst surface influences strongly the activity. The catalyst prepared by round-bottom flask shows a conversion of 90.9 % after 90 minutes, whereas by nozzle method a complete turnover after 60 minutes was obtained.

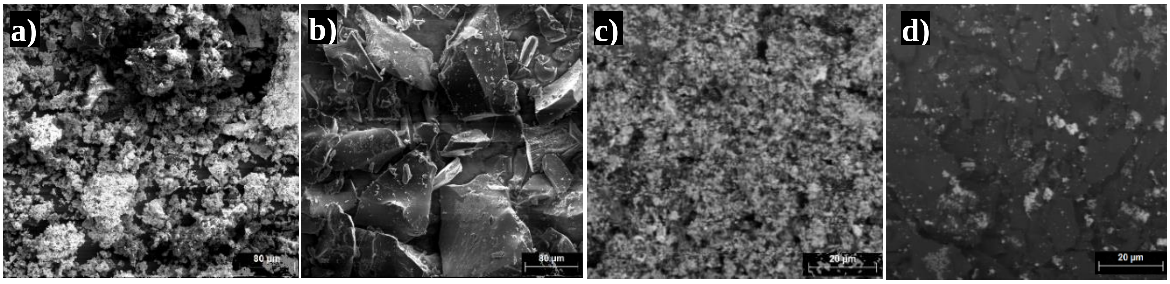

Figure A2.2. SEM micrographs of catalysts prepared with different pyrolysis methods, a) DES CV N + MF 440 °C, b) DES CV, F + MF 440 °C. SEM-BSE micrographs of the same catalysts c) DES CV N + MF 440 °C, d) DES CV, F + MF 440 °C.

2.6.5 Characterization of the supporting materials without metal

TGA measurements

20 mg of the DES starting materials according to the ratios described in Table A2.4 were measured in an alumina crucible. The mixtures were heated under an argon stream of 70 sscm to 500 °C using a heating rate of 10 °C min^{-1}.

The decomposition of all DES started between 150 - 170 °C with exception of the DES based on choline chloride and D-sorbitol (260 °C) and was stopped at 500 °C with a total weight loss between 70 % - 95 % (Figure A2.3, A2.4 and A2.5). The greatest weight loss of all DES can be observed between 200 °C and 300 °C. The choline chloride based mixtures CV, CF and CG loose about 70 % of their weight in this temperature range with exception of CS (90 %) (Figure A2.3) and the N,N´-dimethylurea (Figure A2.4) and urea (Figure A2.5) based mixtures 70 % - 80 % and 55 % - 70 %, respectively. All catalysts prepared show the highest activities at a pyrolysis temperature between 400 °C and 500 °C. In this area, the weight loss of the mixtures is only very low or the amount of formed supporting materials remains rather constant. Thus, the TGA measurements do not clarify why the small differences in pyrolysis temperature have a major influence on the catalyst activity.

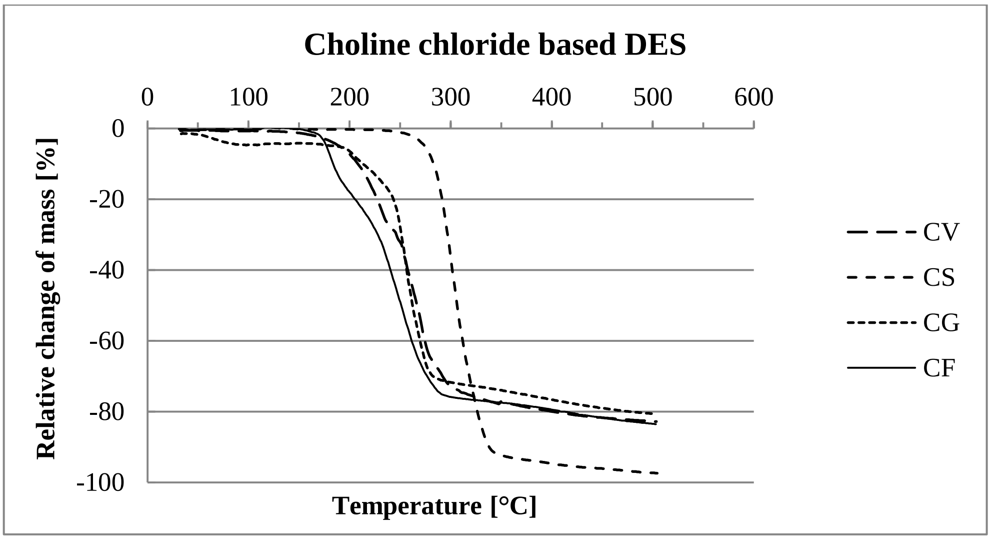

Figure A2.3: TGA measurements show the relative change of mass during the heating of choline chloride based DES under inert atmosphere to 500 °C.

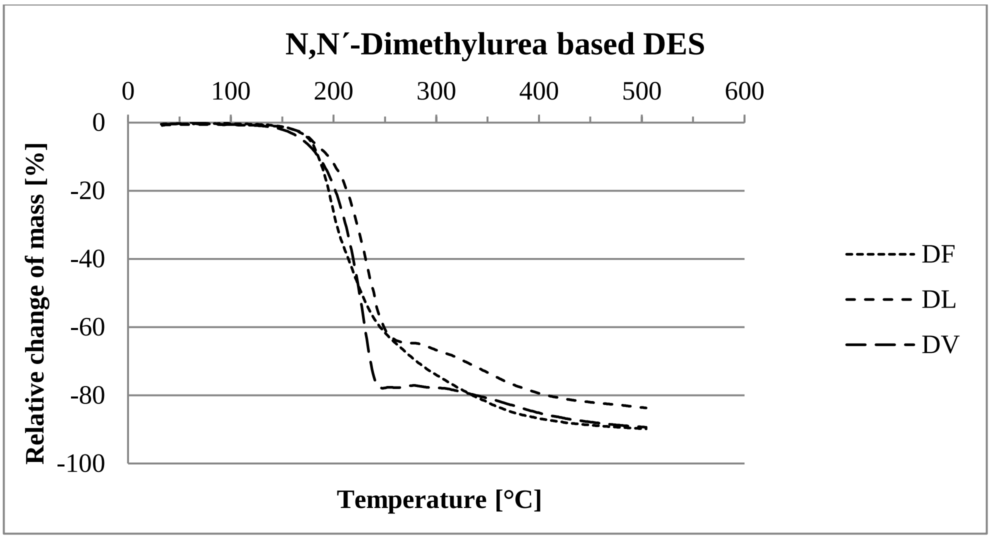

Figure A2.4. TGA measurements show the relative change of mass during the heating of N,N´-dimethylurea based DES under inert atmosphere to 500 °C.

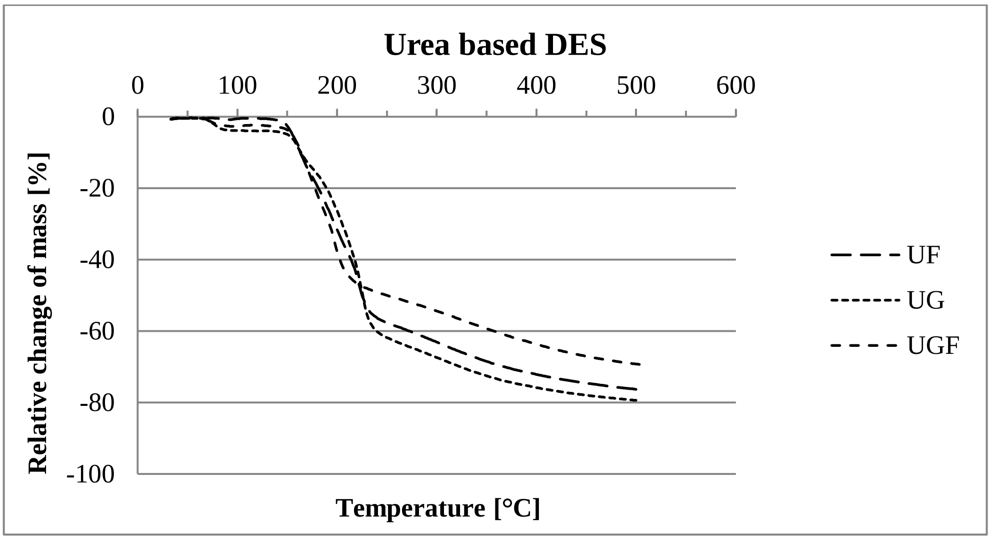

Figure A2.5. TGA measurements show the relative change of mass during the heating of urea based DES under inert atmosphere to 500 °C.

Particle Size Distribution

Particle size distribution of three different supporting materials based on the DES UG were measured. Samples were prepared using the flask method at 440 °C and 470 °C and the nozzle method at 440 °C. For the measurements, 100 - 250 mg of the sample was transferred to an ethanol chamber in the measuring device. After 60 s of sonication, the solution of ethanol and the solid supporting material was measured by laser diffraction.

Every measurement supplies three particle sizes: Diameter 10 % (D10), Diameter 50 % (D50) and Diameter 90 % (D90), which shows that 10 %, 50 % or 90 % of the particles are smaller than the denoted sizes.

Relatively large particles are formed by both preparation methods with D90 values of

78.3 µm (round-bottom flask method) and 110.1 µm (flask method) (Table A2.6). Contrary to the expectations, the nozzle method shows larger particle sizes compared to the flask method. In comparison with a commercially available activated carbon sample (VWR, D90 = 100 µm), our material shows a quite similar particle size.

Table A2.6. Particle size distribution of DES UG based supporting materials prepared by round-bottom flask method at 440 °C and 470 °C and by nozzle method at 440 °C.

	Diameter 10 % [µm]	**Diameter 50 % [µm]**	**Diameter 90 % [µm]**
Flask method 440 °C	11.2	39.1	78.3
Flask method 470 °C	13.1	41.5	80.1
Nozzle method 440 °C	15.2	48.2	110.1

2.6.6 Experiments for an increasing surface area of the UG based supports

Ammonium bicarbonate

In a 25 mL - round-bottom flask equipped with a magnetic stirring bar, 60 wt% (1080.9 mg) ᴅ-glucose and 30 wt% (540.5 mg) urea were heated to 110 °C in a sand bath until a clear homogeneous liquid was formed. In this solvent, 108 mg palladium acetate and 10 wt% (180.2 mg) ammonium bicarbonate were dissolved. After a complete dissolution, the mixture was heated under nitrogen atmosphere up to 280 °C without stirring for 1 h until a dry brown porous material resulted. Further pyrolysis was done in a muffle furnace under nitrogen atmosphere up to 440 °C.

BET surface: 1.97 ± 0.21 $m^2 g^{-1}$

Activity: 0% conversion after 90 min

Silica gel 60

In a 25 mL - round-bottom flask equipped with a magnetic stirring bar, 40 wt% (770.0 mg) ᴅ-glucose and 60 wt% (1040.0 mg) urea were heated to 110 °C in a sand bath until a clear homogeneous liquid was formed. In this solvent, 108 mg palladium acetate was dissolved and 600.0 mg silica gel 60 was added. Afterwards, the mixture was heated under nitrogen atmosphere to 270 °C without stirring for 1.5 h resulting in a dry brown porous material. Further pyrolysis was done in a muffle furnace under nitrogen atmosphere up to 440 °C.

BET surface: 262.28 ± 2.32 m^2 g^{-1}

Activity: 65.2 % conversion after 150 min

Zeolite

In a 25 mL - round-bottom flask equipped with a magnetic stirring bar, 40 wt% (770.0 mg) D-glucose and 60 wt% (1040.0 mg) urea were heated to 110 °C in a sand bath until a clear homogeneous liquid was formed. In this solvent, 108 mg palladium acetate was dissolved and 600.0 mg zeolite was added. Afterwards, the mixture was heated under nitrogen atmosphere to 270 °C without stirring for 1.5 h until a dry brown porous material was formed. Further pyrolysis was done in a muffle furnace under nitrogen atmosphere up to 440 °C.

BET surface: 8.34 ± 0.07 m^2 g^{-1}

Activity: 13.0 % conversion after 120 min

The influence of a larger surface area on the catalyst activity should be investigated. Two different strategies for the enlargement of the surface were examined. On the one hand, ammonium bicarbonate was added to the DES in order to produce a more porous material by the release of CO_2 during pyrolysis. On the other hand, an additional support was added to the mixture prior to pyrolysis. The Pd/CNO catalyst should be coated on particles with a large surface area, and thus increase the surface area.

BET measurements of the prepared samples show a significant increase of surface area to 262.28 m^2 g^{-1} using Silica gel 60 as additional support, while only small surface areas were obtained by the ammonium bicarbonate experiment and the addition of zeolites. Nevertheless, the activity of all samples decrease compared to the initial UG-based catalyst.

2.7 References

[1] R. A. Sheldon, I. Arends, U. Hanefeld, *Green chemistry and catalysis*, John Wiley & Sons, **2007**.

[2] E. Auer, A. Freund, J. Pietsch, T. Tacke, *Applied Catalysis A: General* **1998**, *173*, 259-271.

[3] D. S. Cameron, S. J. Cooper, I. L. Dodgson, B. Harrison, J. W. Jenkins, *Catalysis Today* **1990**, *7*, 113-137.

[4] C. Hagelüken, *Erzmetall* **1996**, *49*, 122-133.

[5] M. Gurrath, T. Kuretzky, H. Boehm, L. Okhlopkova, A. Lisitsyn, V. Likholobov, *Carbon* **2000**, *38*, 1241-1255.

[6] J. García-Álvarez, *European Journal of Inorganic Chemistry* **2015**, *2015*, 5147-5157.
[7] D. A. Alonso, A. Baeza, R. Chinchilla, G. Guillena, I. M. Pastor, D. J. Ramón, *European Journal of Organic Chemistry* **2016**, *2016*, 612-632.
[8] P. Liu, J.-W. Hao, L.-P. Mo, Z.-H. Zhang, *RSC Advances* **2015**, *5*, 48675-48704.
[9] Q. Zhang, K. De Oliveira Vigier, S. Royer, F. Jerome, *Chemical Society Reviews* **2012**, *41*, 7108-7146.
[10] C. Ruß, B. König, *Green Chemistry* **2012**, *14*, 2969-2982.
[11] M. Francisco, A. van den Bruinhorst, M. C. Kroon, *Angewandte Chemie* **2013**, *125*, 3152-3163.
[12] E. L. Smith, A. P. Abbott, K. S. Ryder, *Chemical Reviews* **2014**, *114*, 11060-11082.
[13] A. P. Abbott, G. Capper, D. L. Davies, K. J. McKenzie, S. U. Obi, *Journal of Chemical & Engineering Data* **2006**, *51*, 1280-1282.
[14] Z. Maugeri, P. D. de María, *Rsc Advances* **2012**, *2*, 421-425.
[15] R. Koirala, S. E. Pratsinis, A. Baiker, *Chemical Society Reviews* **2016**, *45*, 3053-3068.
[16] S. L. Goertzen, K. D. Thériault, A. M. Oickle, A. C. Tarasuk, H. A. Andreas, *Carbon* **2010**, *48*, 1252-1261.
[17] A. M. Oickle, S. L. Goertzen, K. R. Hopper, Y. O. Abdalla, H. A. Andreas, *Carbon* **2010**, *48*, 3313-3322.

CHAPTER 3

3 Pyrolysis of Deep Eutectic Solvents for the Preparation of Supported Copper Electrocatalysts

This chapter has been submitted as:

M. Iwanow, L. Vieira, I. Rud, J. Pößnecker, M. Kaiser, D. Van Opdenbosch, C. Zollfrank, T. Gärtner, B. König, V. Sieber, *Applied Catalysis B: Environmental* **2019**, submitted.

MI carried out the XRD, crystallite size, elemental analysis, reproducibility, LSV and potential screening experiments, developed analytical methods, evaluated all measured data and wrote the manuscript. IR synthesized the catalysts and carried out SEM, CV and CA experiments during his Master thesis under the supervision of MI and LV. JP performed the blank experiments during an internship under supervision of MI and LV. MK developed the GC method for gaseous products. DVO supported the evaluation of XRD. LV, TG, VS and BK supervised the project. VS is the corresponding author.

3.1 Introduction

Formate is widely used in the feed industry, grass silage, leather tanning and anti-icing. The worldwide production of formic acid amounts to 620 kt a^{-1} in 2012 and its demand is likely to increase steadily, when considering applications such as fuel cells or hydrogen carrier.[1-7] Looking at the worldwide formic acid production, the hydrolysis of methyl formate is currently the dominant process route.[8] Recent research activities are focusing on the reduction of greenhouse gas emissions via carbon-capture and usage.[9-11] Thus, electrochemical production of formate from renewable energy, CO_2 and water is an environmentally friendly alternative compared to the existing commercial production routes.

Principally, the electrochemical reduction of CO_2 offers an option for its utilization as building block in the synthesis of value-added chemicals, avoiding further CO_2-emissions, when using renewable energy. In addition, such processes provide a method for intermittent energy storage in energy-dense and portable chemicals.[12-14] Both aspects reduce our dependence on fossil energy sources, especially crude oil, and offers a way to substitute petrochemicals.[13] The electrocatalytic route for CO_2 conversion in aqueous media is a promising method, because it can be performed at ambient pressure and temperature, using low-cost catalysts.[15-16] However, the efficiency of this process depends strongly on the activity and selectivity of the catalyst material, which should bind and activate CO_2 at lower overpotentials, thus enabling the CO_2 conversion and suppressing H_2 evolution.[12, 17-19] A low-cost catalyst operating at high current densities and lower overpotentials would improve the commercial viability of the whole process.[14, 20-22]

According to product selectivity, Pb, Hg, Tl, In, Sn, Cd and Bi electrodes lead mainly to formate [20,23], while Au, Ag, Zn, Pd and Ga electrodes produce mainly CO. Ni, Fe, Pt and Ti electrodes have a rather low overpotential for hydrogen evolution and lead mostly to H_2.[12,23] Compared to the others, copper is the only metal that can convert CO_2 to a mixture of products, including alcohols, hydrocarbons, formate and CO at ambient pressure and temperature.[12,19,23-26] An extra advantage of copper as a catalyst, besides its low toxicity, is the rather low cost (~5900 $/t, 02/04/2019) compared to other catalysts that produce mainly formate from CO_2 such as tin (~20000 $/t) and indium (~340000 $/t).[27] Thus, copper is an attractive catalyst material for the electrochemical formate production.

In this work, we report the development of a new group of copper catalysts on a carbon support for the electrochemical production of formate from CO_2. Therefore, a facile single step preparation method involving the pyrolysis from deep eutectic solvents (DES) was used.[28] A great advantage over conventionally used impregnation methods is that the loading of the catalyst carrier is not determined by the adsorption behavior of the metal compounds on the support surface. Thus, all kinds of copper precursors in desired amounts can be used as starting materials and loaded on the DES-based supporting material. The choice of deep eutectic solvent and preparation temperature influence the properties of the final supporting material and therefore the activity of the electrocatalyst. The preparation procedure may improve the activity of the obtained copper catalysts due to a better stabilization of the copper on the support and *in situ* building of an active copper modification. The spatial proximity of CO_2 binding domains (amines)[29-30] or basic surface properties on the support and the active sites of the catalyst should favour the product formation.

3.2 Results and discussion

3.2.1 Catalyst preparation and characterization

The influence of the different parameters on the activity of the 96 prepared copper catalysts was investigated (Table 3.1).

Table 3.1. Overview of the catalysts prepared from different DES, copper precursors and pyrolysis temperatures; Colors indicate the electrochemical measurements carried out at each material: green (✓) - investigated on a GDL with product analysis, yellow (◆) - Cyclic voltammetry and chronoamperometry for pre-characterization; red (-) - coating of the material on a current collector was not possible.

DES	**Copper precursor and pyrolysis temperature [°C]**															
	CuNP				CuO				CuAc				Cu_2O			
	425	450	475	500	425	450	475	500	425	450	475	500	425	450	475	500
CF	◆	✓	◆	◆	◆	◆	◆	◆	◆	◆	◆	◆	◆	◆	◆	◆
CV	✓	✓	✓	✓	✓	✓	✓	✓	✓	◆	◆	◆	✓	◆	◆	◆
DF	◆	✓	◆	◆	-	-	-	-	-	-	◆	◆	◆	◆	◆	◆
DL	◆	✓	◆	◆	◆	◆	◆	◆	◆	◆	◆	◆	◆	◆	◆	◆
UG	✓	✓	✓	✓	◆	◆	◆	◆	◆	◆	◆	◆	◆	◆	◆	◆
UGF	◆	✓	◆	◆	◆	◆	◆	◆	◆	◆	◆	◆	◆	◆	◆	◆

All prepared copper catalysts were electrochemically characterized using cyclic voltammetry and chronoamperometry in argon and CO_2 saturated 0.5 M $KHCO_3$ electrolyte. The comparison of current densities in CO_2 and Ar saturated solutions gives a hint of the material activity, although this method is not conclusive and chemical analysis is needed. We used this method for pre-screening of the current densities in different materials. Those with the highest current densities in CO_2 and the highest difference with regard to Argon saturated solutions were chosen for chemical analysis (Table S3.1 in Chapter 3.5). Based on these data and due to a methodical comparison of the preparation parameter, 19 catalysts (Table 3.1, ✓ and green marked) were used for the CO_2 reduction with chemical analysis.

The properties of the different Cu/CNO catalysts and the different supporting materials were investigated by XRD and SEM. Measurements provide information on the resulting modification and morphology of copper after the pyrolysis. All catalysts show mainly reflexes attributed to metallic copper (Figure S3.1 in Chapter 3.5). Reflexes related to copper(I) and copper(II) oxides were only observed in the catalysts prepared from DES based on CF, UG and UGF. The catalysts were named according to the following scheme: DES + precursor + pyrolysis temperature.

SEM pictures (Figure 3.1) show that the choice of the deep eutectic solvent also influences the particle size. UG-based DES (Figure 3.1e) formed a fine powder, whereas DES based on CV led to larger particles (Figure 3.1b). It is also noticeable that the pyrolysis of the DF-based DES (Figure 3.1c) resulted in a mixture of a fine powder and large particles, while the other DES showed more homogeneous particle sizes.

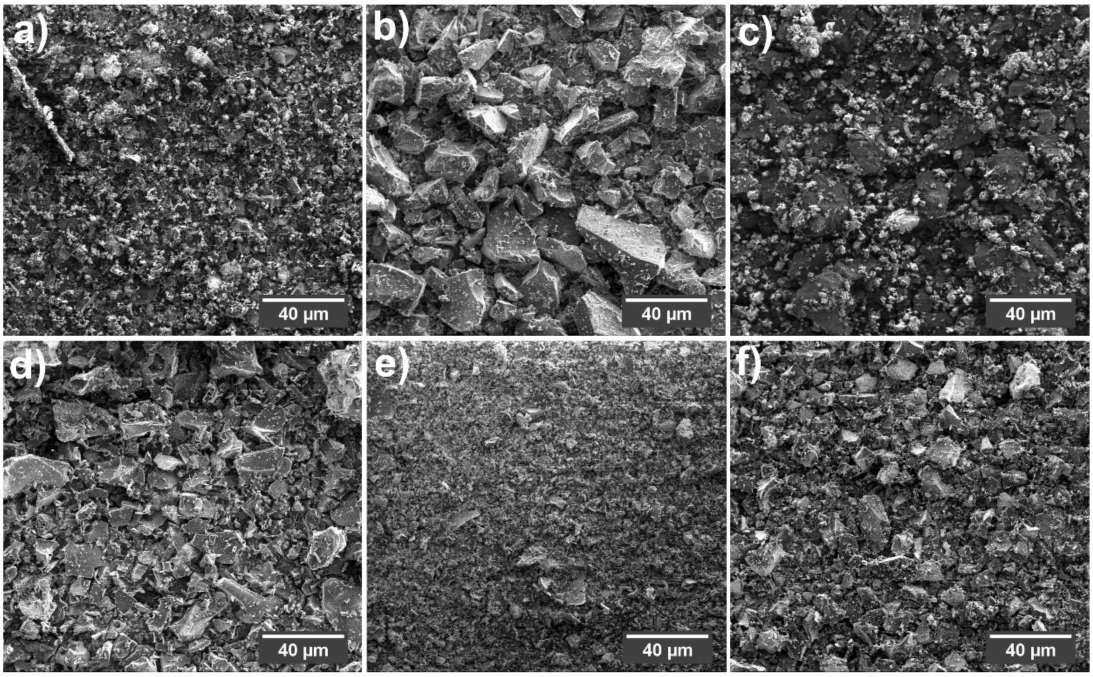

Figure 3.1. SEM investigations of supported copper catalysts: prepared using different DESs with CuNP as precursor and a pyrolysis temperature of 450 °C, a) CFCuNP450, b) CVCuNP450, c) DFCuNP450, d) DLCuNP450, e) UGCuNP450, f) UGFCuNP450.

Elemental mapping measurements with an EDX detector (Figure S3.2 in Chapter 3.5), verified a good distribution of copper on the surface of the catalyst particles with exception of the DL-based material, in which only copper spots on DES support can be found. This can be explained by the large polymeric structure of lignin, which may not lead to a completely homogeneous DES and thus to an inhomogeneous distribution of the metal in the DES. Besides the catalyst particle size determination by SEM, the metal crystallite size was evaluated by XRD (Equation 1 in Chapter 2.2.2).[31] By applying the Scherrer equation, crystallite sizes in a range of 33.8 nm and 68.2 nm were determined (Figure 3.2 and Table S3.2 in Chapter 3.5). According to Reskes group[32], the size of copper nanoparticles influences strongly the activity and selectivity of the electrochemical CO_2 reduction. Smaller nanoparticles (< 5 nm) increase the catalytic activity, but suppress the selectivity towards hydrocarbon production. Thus, investigations in more detail of the prepared copper crystallite sizes in the Cu/CNO catalysts may clarify the catalytic activity. The calculation of the crystallite dimension in one direction using the (200) plane is sufficient due to the cubic crystallographic system of copper. The copper precursor and the pyrolysis temperature have less influence on the crystallite size (Figure 3.1b and 3.1c) than the choice of DES. Larger variations are found in the crystal size of the catalysts prepared by different DES (Figure 3.1a).

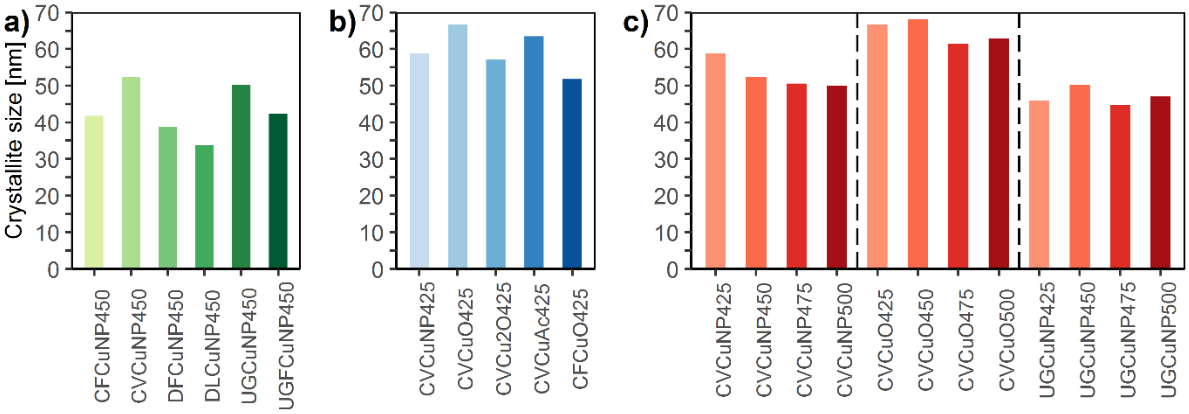

Figure 3.2. Crystallite sizes of the different copper catalysts determined by XRD: a) influence of the different DES, b) influence of the copper precursor and c) influence of the pyrolysis temperature on the copper crystallite size.

It is known from literature[33] that DES can fulfil multiple roles in directing chemistry at the nanoscale such as acting as supramolecular templates and stabilizing reagents for nanoparticles. Moreover, DES components may modulate nucleation and growth mechanisms and thus, dictate growth along defined directions. The observation that the DES mainly affect the crystallite size corresponds exactly to the findings in the literature.

After characterization of the Cu/CNO catalysts, a closer look to the supporting material itself was taken. Figure 3.3 compares the elemental composition of the supports prepared by different DES before and after pyrolysis, which are determined by calculations and CHNS/O elemental analysis. It was found that the amount of nitrogen after the pyrolysis shows an uncertainty to a difference of 8 wt%, while the carbon ratio increases distinctly and the amounts of oxygen, hydrogen and chloride decrease. The urea-based mixtures (UG, UGF) show the highest nitrogen content followed by the N,N´-dimethylurea (DF, DL) and choline chloride-based (CF, CV) supports. Thus, the amount of nitrogen is mainly defined by the choice of starting materials.

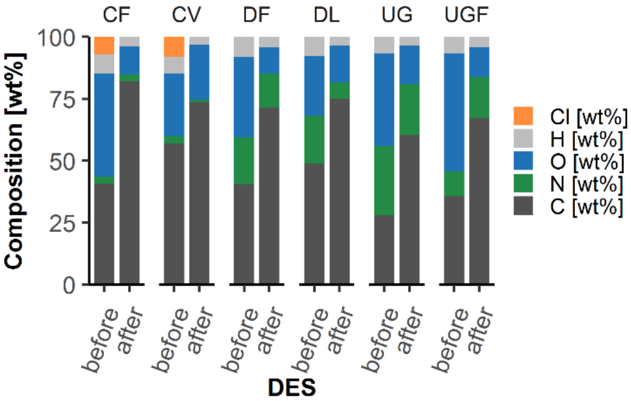

Figure 3.3. Characterization of the elemental composition of the supporting material before and after pyrolysis.

Aim of the catalyst preparation was to utilize the basic functional groups on the surface of the materials due to the Lewis acidic properties of CO_2. Thus, a high amount of basic groups is expected to have a positive effect on CO_2 adsorption and therefore on the CO_2 electrolysis. To compare the binding capacities and the influence of the basic surface groups on the activity of the prepared materials with a commercial one, the amounts of functional groups on the surface of the pyrolysis products were investigated. Boehm titrations of the supporting material without copper showed that the carbon materials are rich in acidic and basic oxygen-containing functional groups (Figure 3.4 and Table S3.3 in Chapter 3.5).

Commercially available activated carbon shows a total amount of 1094 µmol g^{-1} functional groups on the surface, while the DES-based materials provide evidently higher values with an overall amount of functional groups from 888 µmol g^{-1} (CF) to 2091 µmol g^{-1} (UG). Actually, the amount of functional groups may be even higher due to limitations of the Boehm method. Porosity of the materials can reduce the solvent accessible surface and only acidic and basic surface groups are detected.[34] Examples of oxygen-containing acidic functional groups are carboxylates, lactones, phenols and ketones, whereas pyrenes and chromenes can be assigned to basic groups.[35] It was found that the hydrogen bond acceptor in the DES primarily influences the amount of surface groups on the pyrolyzed materials. The urea-based DES UG and UGF exhibit the highest amounts, followed by the N,N´-dimethylurea (DF, DL) and the choline chloride-based (CF, CV) mixtures. Apart from a commercial activated carbon sample, only the DES DL and CV show more acidic than basic surface groups, while all other mixtures show more basic than acidic functional groups.

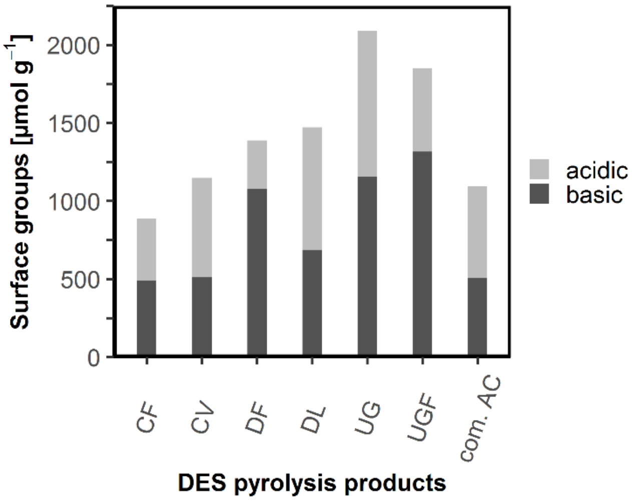

Figure 3.4. Characterization of the supporting material using Boehm titrations.

Comparison of these results with the CHNS/O elemental analysis confirms the trend. Urea-based materials show the highest nitrogen content and result in a higher amount of basic surface groups compared to choline chloride-based supports with comparable low nitrogen contents and the lowest amounts of basic surface groups. The pyrolysis of the nitrogen-containing mixtures under inert conditions promotes the formation of amine groups, which is supposed to improve the CO_2 adsorption.[29-30] Therefore, higher nitrogen contents in the support should also increase the amount of adsorbed CO_2, when the nitrogen-containing starting materials form amines during the pyrolysis.

The capacity of CO_2 binding was investigated using CO_2 adsorption experiments of two differently prepared materials, a nitrogen-rich (UG) and a nitrogen-poor (CV) DES support and a commercial sample of activated carbon (Table S3.4 in Chapter 3.5). Usually, adsorption measurements with CO_2 are performed to determine the amount and volume of micropores in solid materials by the Dubinin-Radushkevich equation[36], but in our case the amount of overall adsorbed carbon dioxide on the support was of interest. Contrary to the theory, the nitrogen-poor and comparably less basic CV material adsorbs almost twice the amount of carbon dioxide (3.96 mL g^{-1} at a relative pressure of 0.03) as the nitrogen-rich and significantly more basic UG support (2.60 mL g^{-1} at a relative pressure of 0.03). The commercially available sample, which shows less basic functional groups and a low nitrogen content (about 6.5 wt%) as well, adsorbs 9.38 mL g^{-1} carbon dioxide at a relative pressure of 0.03. This shows the same tendency as for the DES CV that higher amounts of carbon dioxide are adsorbed with less basic and nitrogen-containing groups. Thus, it was ascertained that there is no influence of basic surface groups and high nitrogen contents on the CO_2 binding capacities of the supporting material. However, the question remains, which parameter promotes the adsorption of CO_2 on the surface of the catalyst materials. Since the preparation of the catalysts with different deep eutectic solvents provides different particle morphologies (Figure 3.1), it is possible that the different surface structures influence the adsorption of carbon dioxide.

X-ray diffraction measurements of the pyrolyzed deep eutectic solvents clarify whether crystalline parts are available after the pyrolysis. The materials based on UG, DF and CV show a broad amorphous peak at the 2θ angle of 26°, corresponding to $d = 3.4$ Å. This value can be related to the interlayer distance 002 of graphite and the distance expected from stacked planar carbon structures. Pair distribution functions *G(r)* functions describe the quantity of interatomic distances *r*. The *G(r)* of all materials are closely correlated to those of crystalline graphite only up to 10 Å (Figure 3.5). These functions describe the probability to find atomic distances at the defined values.

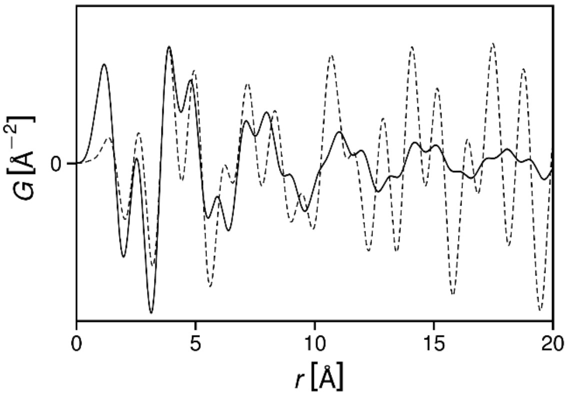

Figure 3.5. Exemplary (DES DF) reduced pair distribution function calculated from scattering data, overlaid with that of graphite (dashed line).

Thus, it can be assumed that with respect to carbon modifications, graphitic structures with long-range orders higher than 10 Å were not present and mainly amorphous materials were formed during pyrolysis of the DES.

3.2.2 Electrochemical CO_2 Reduction

The optimum copper loading in the carbon support and the optimum catalyst material loading immobilized on an electrode surface was investigated by current densities in a CO_2 saturated electrolyte (Figure 3.6). Four different copper catalysts were prepared with a different copper loading in the carbon support. The metal loading was calculated from the theoretical carbon amount in the DES to be 5 wt%, 10 wt%, 20 wt% and 50 wt% of Cu in the final material. The deep eutectic solvent (CV), copper precursor (CuNP) and pyrolysis temperature (450 °C) were kept constant for the catalysts preparation. As for the electrode loading, 3 mg, 5 mg and 10 mg of the 50 wt% loaded Cu/CNO were immobilized on a copper substrate.

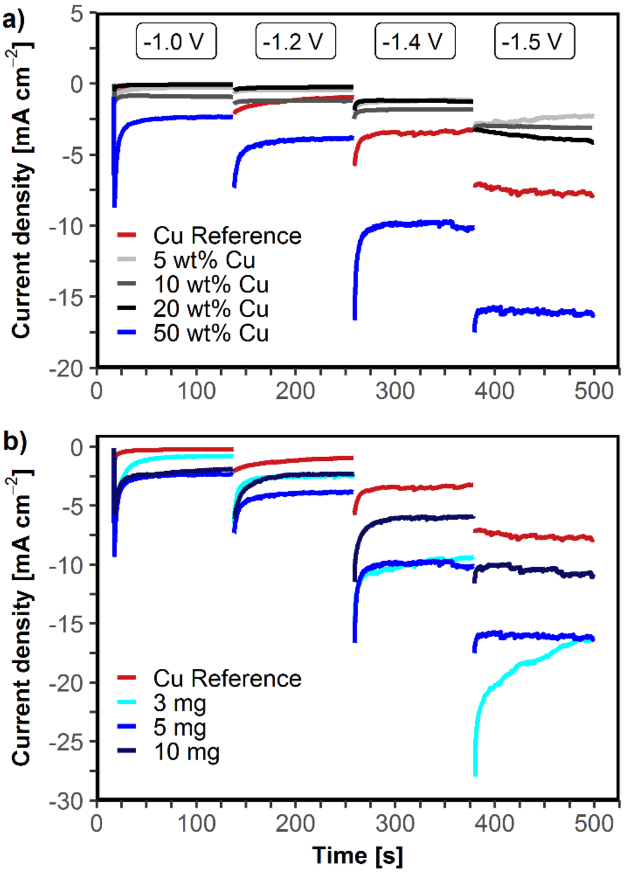

Figure 3.6. Chronoamperometry at different step potentials for catalyst sample varying: a) the copper loading in the DES support for a 5 mg cm^{-2} loading and b) catalyst immobilization on a copper substrate for a 50 wt% Cu/CNO sample. The samples were compared to a copper sheet.

Figure 3.6 shows the chronoamperograms at different step potentials (-1.0 V, -1.2 V, -1.4 V and -1.5 V) for the materials varying the copper loading in the DES support (a) and varying the material immobilization on the current collector (b). Increasing the copper content in the carbon support, increases the current density in a linear fashion. Hence, a copper loading of 50 wt% shows the highest current density for all step potentials. Varying the amount of the same material in the substrate electrode, however, does not change the current density in a linear way. Although, all electrodes with immobilized catalyst showed a higher current density than bare copper. Electrodes containing 3 mg cm^{-2} and 5 mg cm^{-2} showed higher current densities compared to that with 10 mg cm^{-2}. Catalyst loading of 5 mg cm^{-2} led to a more stable current density than electrodes containing 3 mg cm^{-2}. The following measurements were all performed with 5 mg cm^{-2} of a 50 wt% Cu/CNO.

Experiments on a bare gas diffusion layer (GDL) and on six DES-based carbon supports, both in the absence of copper, showed very low current densities and almost no product formation. The GDL led to 0.8 % FE of formate and from the six carbon materials, CF and CV showed respectively 5.84 % and 0.53 % total FE for formate and carbon monoxide (Table S3.5 in Chapter 3.5). Thus, these electrochemical measurements confirmed that the metal is essential for the activity of the catalysts.

Experiments using two different catalyst batches of the same procedure, namely the CVCuNP450-1 or CVCuNP450-2, or two samples of the same catalyst batch (CVCuNP450-2) led to rather similar current densities and formate concentrations (Table 3.2). Consequently, the Faraday efficiency was in the same range with 2 % difference, showing a good reproducibility.

Table 3.2. Reproducibility of the electrochemical CO_2 reduction process: comparison of concentration and Faraday efficiency of formate as well as current density.

Electrode	**Concentration [mM]**	**Faraday efficiency [%]**	**Current density [mA cm^{-2}]**
CVCuNP450-1	8.9	8.6	13.8
CVCuNP450-2	11.1	9.8	18.2
CVCuNP450-2	11.7	10.6	15.8

The electrochemical activity of catalysts containing 50 wt% Cu and prepared from six different DES were investigated by linear sweep voltammetry (LSV). The LSV were compared regarding the effect of the DES, the copper precursors and the pyrolysis temperature on the current densities and onset potential (Figure 3.7).

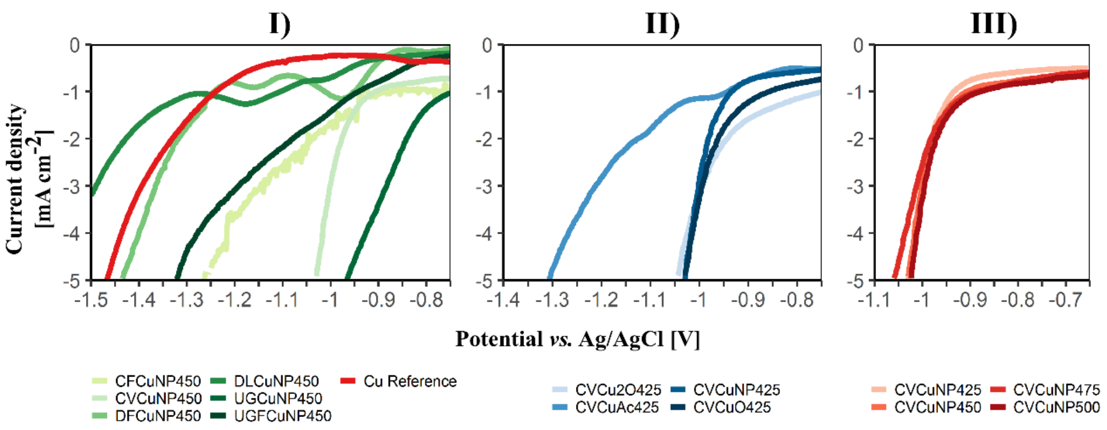

Figure 3.7. LSV of Cu/CNO catalysts in 0.5 M $KHCO_3$ solution saturated with CO_2 at 50 mV s^{-1} scan rate. In the preparation of the catalysts, different parameters were varied: **I)** the nature of the DES; **II)** the copper precursor; **III)** the pyrolysis temperatures.

Almost all tested catalysts show higher current densities compared to a bare copper sheet, with exception of the DES based on lignin (DL). The different preparation parameters also influenced the onset potential for the parallel occurring reactions: CO_2 and water reduction. The overpotential is defined as difference between the standard equilibrium potential and the onset potential for a given reaction.[14]

Materials synthesized from six different DES (Figure 3.7I), all with copper nanoparticles (CuNP) and at 450 °C pyrolysis temperature showed remarkable fluctuations in current densities and onset potentials. The DES UG (-0.8 V) and CV (-0.95 V) decrease considerably the onset potential compared to a bare copper sheet (-1.2 V). The DES CF (-0.95 V) and UGF (-0.85 V) show similar behavior, both have significantly more positive onset potentials than copper. However, compared to UG and CV, the current density is considerably lower. In a distinct fashion, the DES DL and DF show more negative onset potentials compared to the copper and rather low current densities.

The pyrolysis temperature and the copper precursor effects were investigated on materials prepared from the DES CV, firstly by varying the copper source at 425 °C and later by varying the temperature using CuNP as copper source. Considering LSV of catalysts prepared from different copper precursors shown in Figure 3.7II, the onset potential becomes more positive compared to copper and increase from -1.2 V to about -0.95 V for CuNP, CuO and Cu_2O, and -1.05 V for copper acetate.

Comparing the effect of the pyrolysis temperature in the LSV in Figure 3.7III, the onset potentials of the materials synthesized from 425 °C to 500 °C (-0.95 V) also show an onset potential considerably more positive than copper. Figures S3.3 to S3.5 in Chapter 3.5 show the LSV from Figure 3.7 in a wider current and potential range.

According to Hori[26], since hydrogen evolution takes place simultaneously with the CO_2 reduction, the analysis of current densities in CO_2 saturated solutions without chemical analysis and quantification of the eventual products is not reliable. Thus, chemical analysis of the gas and liquid phase for the CO_2 reduction on the catalyst CVCuNP450 were carried out at different applied potentials, from -1.3 V to -2.1 V (Figure 3.8 and Table S3.6 in Chapter 3.5). The applied potentials were chosen based on the onset potentials obtained in the LSV. Hence, the chemical analysis were performed at potentials more negative than -1 V. Moreover, the catalyst was immobilized in a gas diffusion layer (GDL). GDL allows a better supply of CO_2 to the catalyst, which otherwise is limited by the CO_2 solubility in the electrolyte, and consequently higher current densities for CO_2 reduction can be achieved.[37]

Chemical analysis of the gas and liquid phase at different applied potentials showed a variety of products from CO_2 reduction (carbon monoxide, formate, ethylene, ethanol and n-propanol). Operating at more positive potentials (-1.3 V and -1.5 V) led to selective formate production in the liquid phase, while C2 (ethylene, ethanol) and C3 (n-propanol) products were formed at more negative potentials (-1.7 V, -1.9 V and -2.1 V). Since considerably more formate is selectively produced at -1.5 V compared to -1.3 V, all further experiments are performed at this potential.

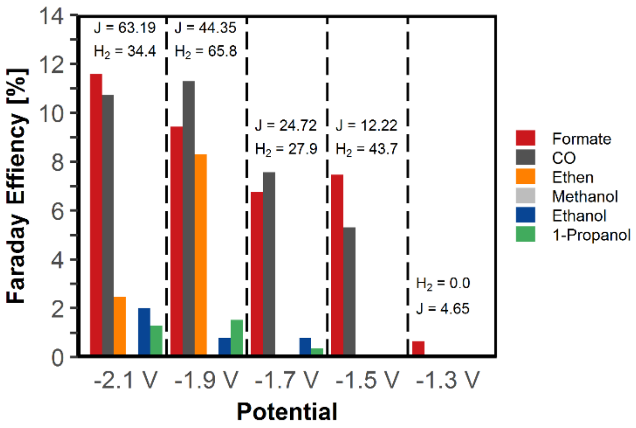

Figure 3.8. Chemical analysis of the products and current density (J, [mA cm^{-2}]) for the electrochemical CO_2 reduction at the catalyst CVCuNP450 on a gas diffusion layer at different step potentials (30 minutes each). Exact values are shown in Table S3.6 in Chapter 3.5.

The catalysts showing the highest current densities in CO_2 saturated solutions, thus considered as the most active, were investigated on GDLs at constant potential (-1.5 V) for two hours. Figure 3.9 shows the measured current densities with the corresponding Faraday efficiencies and formation rates of formate. The catalysts were grouped according to the nature of the DES (I), the copper source (II) and the pyrolysis temperature (III).

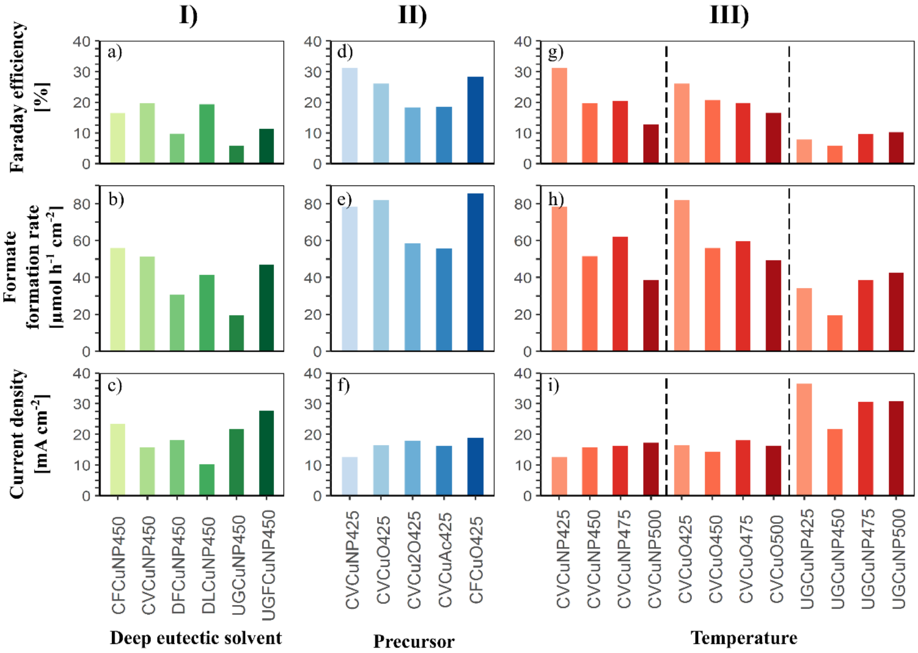

Figure 3.9. Overview of formate Faraday efficiency, formation rate and current density on catalyst prepared varying the following parameters: I) nature of the deep eutectic solvent, II) copper precursor and III) pyrolysis temperature. Each electrochemical measurements was performed at -1.5 V for 30 minutes.

As a result, the CO_2 reduction on the DES-based catalysts provide formate concentrations between 7.8 mM and 34.2 mM, corresponding to formation rates between 19.5 µmol h^{-1} cm^{-2} and 85.5 µmol h^{-1} cm^{-2} (details shown in Table S3.7 in Chapter 3.5).

The nature of the DES strongly influences the catalyst activity, as already indicated by the LSV, with variations of the formation rate between 19.5 µmol h^{-1} cm^{-2} (UG) and 56.0 µmol h^{-1} cm^{-2} (CF) (Figure 3.9I). Regarding the effect of the copper precursor in Figure 3.9II, the copper nanoparticles and copper(II) oxide result in higher formation rates (78.25 µmol h^{-1} cm^{-2}, 82.0 µmol h^{-1} cm^{-2} and 85.5 µmol h^{-1} cm^{-2}, respectively), compared to copper(I) oxide and copper acetate (55.75 µmol h^{-1} cm^{-2} and 58.5 µmol h^{-1} cm^{-2}, respectively). The pyrolysis temperature (Figure 3.9III) has a considerable effect on the catalyst activity, since the highest formation rates of formate were obtained with samples prepared at 425 °C, with exception of the UG-based DES, which shows negligible fluctuations of formation rates for the investigated pyrolysis temperatures (425 °C, 450 °C, 475 °C and 500 °C). These results confirm the importance of product analysis in electrochemical measurements. Both, the influence of the copper precursor and the different pyrolysis temperatures show clear deviations from the LSV. According to these, Cu_2O should perform as well as CuNP and CuO, and all different pyrolysis temperatures should similarly affect the activity.

The size of the copper crystallites in the carbon support, as determined by XRD, showed no significant influence on the electrochemical catalyst activity toward CO_2 reduction. For instance, materials prepared with CV and UG DES, both with 50 nm copper crystallite size, showed quite distinct electrochemical activity. CV led to considerably higher concentrations of formate compared to UG-based materials. Furthermore, the oxidation state of copper in the support may influence the electrochemical activity in a more significant way than the size of the copper crystallites. The more active catalysts based on CV had mainly metallic copper in its crystalline phase, while the less active UG-based catalysts consisted on a mixture of Cu, Cu_2O and CuO in the DES-based carbon support (Figure S3.1 in Chapter 3.5). A specific and more detailed study about the oxidation state of copper in the carbon support will be reported in Chapter 4.

Regarding the capacity of adsorbing CO_2, as shown by the CO_2 adsorption analysis (Table S3.4 in Chapter 3.5), it has been observed that the materials that adsorb more CO_2 (CV) result in higher product amounts compared to materials with lower CO_2 adsorption (UG). This indicates that the carbon support influences the reaction in the copper active sites by increasing the CO_2 adsorption on the electrode surface.

Moreover, catalysts with a higher formation rate can be further optimized by improving the electrochemical CO_2 reduction process, such as electrode preparation (catalyst loading, binder and procedure)[38], supporting electrolytes type and concentration as well as the CO_2 gas flow and the GDL properties.[39]

The achieved formation rates for formate show already good results compared to the rates of copper catalysts in recent literature (Table 3.3).

Still, tin catalysts exhibit about threefold higher rates compared to the Cu/CNO catalyst.[40] Nevertheless, the facile method for the catalyst preparation and the low cost of starting materials offer additional benefits for this method based on the pyrolysis of DES.

Table 3.3. Overview of formate formation rates found in literature and of the best catalyst prepared.

Catalyst	Formation rate [µmol h^{-1} cm^{-2}]	Conditions	Year	Ref.
CuO nanoparticles	21.0	-1.4 V *vs.* Ag/AgCl	2016	[41]
porous dendritic copper	22.0	5 mA cm^{-2}	2017	[42]
Cu/CNO	85.5	-1.5 V *vs.* Ag/AgCl	2019	this work
Sn	228	-2.0 V *vs.* SCE	2014	[40]

3.3 Conclusions

The reported protocol demonstrates a novel and facile preparation method for copper supported on carbon material through the pyrolysis of deep eutectic solvents. These copper/carbonaceous materials could be used as electrocatalysts for CO_2 reduction to formate, resulting in high formation rates compared to the literature. Several parameters such as copper loading in the carbon support, catalyst material loading on the electrode, as well as the nature of the DES, copper precursors and influence of pyrolysis temperatures were investigated. The catalysts prepared led to the production of formate in yields up to 85.5 µmol h^{-1} cm^{-2} as the only liquid product from CO_2 reduction at -1.5 V *vs.* Ag/AgCl. In summary, it we conclude that the different preparation parameters significantly affect the catalysts activity and it was possible to assign catalyst properties with larger or smaller effect on the catalyst activity. Choline chloride-based materials (CV and CF) prepared with copper nanoparticles at a pyrolysis temperature of 425 °C showed the highest formation rates.

3.4 Experimental

3.4.1 Chemicals

Commercial reagents and used chemicals were purchased from Sigma Aldrich, Acros, TCI, VWR, Carl Roth, Merck or Alfa Aesar and used without further purification.

3.4.2 Catalyst preparation

Catalysts were prepared as described previously.[28] In a round-bottom flask of 25 mL, a total amount of 25 mmol of the different DES materials were heated to 110 °C until a clear, homogeneous liquid was formed. The following molar ratios of the different DES were used: choline chloride - D-fructose (CF, 1:2), choline chloride - vanillin (CV, 1:2), N,N´-dimethylurea - D-fructose (DF, 3:1), N,N´-dimethylurea - lignin (DL, 60:40 wt%), urea - D-glucose (UG, 9:2) or urea - D-glucose - D-fructose (UGF, 9:5.5:5.5). To obtain a theoretical copper loading of 50 wt% in the final material (Cu/CNO), different amounts of copper precursors CuNP, CuO, CuAc and Cu_2O were added to the mixture as shown in Table 3.4. As soon as the metal compound was homogeneously distributed, the mixture was heated to 290 °C under inert gas atmosphere for 90 minutes. Afterwards, the pre-pyrolyzed material was further heated in a muffle furnace to the different final temperatures of 425 °C, 450 °C, 475 °C and 500 °C under inert atmosphere until the material turned into a fine black powder. In summary, 96 catalysts were prepared for activity screening and investigation of the preparation parameter influence.

Table 3.4. Overview of the starting materials used; CuNP - copper nanopowder, CuAc - copper acetate.

DES	Cu precursor [g in 25 mmol DES]			
	CuNP	CuO	CuAc	Cu_2O
CF	0.85	1.06	2.67	0.96
CV	0.95	1.19	2.99	1.07
DF	0.56	0.70	1.77	0.63
DL	0.20	0.25	0.63	0.23
UG	0.29	0.36	0.90	0.32
UGF	0.56	0.70	1.77	0.63

3.4.3 Catalyst characterization

Scanning electron microscopy (SEM)

Scanning electron microscopy was performed to determine the morphologies of the supporting material by secondary electron (SE) detector. The distribution of the copper on the support and the composition of the support was evaluated with the energy-disperive X-ray (EDX) spectroscopy and elemental mapping. The samples were fixed on a carbon tape and investigated using a digital scanning electron microscope (Zeiss, DSM 940 A, Oberkochen, Germany) with the following operating parameters: 10 kV for imaging, 20 kV for mapping.

Powder diffractometry (XRD)

Materials were assessed by powder X-ray diffractometry in Bragg-Brentano geometry (XRD, Miniflex, Rigaku, Tokyo, Japan with silicon strip detector D/teX Ultra). Copper Kα radiation was used and the samples rotated during measurements. Intensities were recorded in steps of $2\theta = 0.02°$; Soller slits with angular apertures of 5° were used. Samples were placed on monocrystalline silicon substrates, which showed no Bragg reflexes within the considered range of 2θ. Their continuous background scattering intensities were recorded separately and subtracted. Our results were compared with data in the Crystallography Open Database (COD) by the Rigaku PDXL software (integrated X-ray powder diffraction software).

A combination with the Scherrer equation (1) allows the calculation of the crystallite size:

$$D_{hkl} = \frac{\lambda \cdot \kappa}{FWHM \cdot \cos(\theta)} \qquad (1)$$

Thereby, D_{hkl} is the crystallite size in h, k and l direction, κ is the shape constant chosen for that system (0.94) and FWHM the full width at half-maximum of the diffraction peak. The intrinsic machine line width was taken into consideration.

Reduced pair distribution functions[43] G(r) were calculated from the scattering patterns, using the Diffpy suite.[44] Due to the maximum recorded scattering angle $2\theta = 100°$ and the X-ray wavelength $\lambda = 1.54$ Å, the resolution was in all cases limited to $q_{\text{max}} = 6.25$ Å^{-1}.

Elemental analysis

CHNS/O elemental analysis was performed using an EuroEA 3000 Serie of the HEKAtech GmbH (Germany). After oxidation at 1000 °C, gas chromatography with thermal conductivity detector separates and analyzes the gaseous products. Carbon, hydrogen and nitrogen relative contents were measured using 1 - 3 mg of sample in tin capsules and the relative content of oxygen (O) was quantified using silver capsules with 1 - 2 mg of sample.

Boehm titration

Boehm titrations were carried out by using the results of standardization experiments performed by Goertzen *et al.* and Oickle *et al.*. [45-46] Defined amounts of the supporting material without metal were agitated in 0.05 M hydrochloric acid or sodium hydroxide solution for 24 h. After filtration of the solid material and saturation with N_2 for two hours, to ensure a complete removal of carbon dioxide, the titration of the solutions to pH 7 allows the calculation of the amount of basic or acidic surface groups.

3.4.4 Electrocatalytic tests

Electrode preparation

A defined amount of the as-prepared catalysts was dispersed in 400 µL of a mixture of distilled water and isopropanol (1:1) with 10.8 µL of a 5 wt% Nafion® solution as binder and sonicated. The mixture was drop coated on the substrates and dried in an oven in air at 80 °C for 1 h. The substrates consisted on 1 cm^2 copper sheets (99.95+% purity, Advent Research Materials) and gas diffusion layers (GDL, Freudenberg).

Electrochemical measurements

Catalyst screening was carried out in two steps: firstly, all materials were measured in a 1-compartment three-electrode cell in 20 mL of CO_2 or Argon saturated 0.5 M $KHCO_3$. An Ag/AgCl in 3 M KCl electrode (Metrohm) was used as reference (RE) and a TiO_2/IrO_2 mesh (Metakem, 6x3.5x1x1 mm, 12 g m^{-2} of Ir) as a counter electrode (CE). All experiments were performed at room temperature (23 ºC).

The second step was performed using gas diffusion electrodes (GDE) in a 3-compartment cell (Gaskatel) comprising an anode compartment (30 mL of 0.5 M $KHCO_3$), a cathode compartment (15 mL of CO_2 saturated 0.5 M $KHCO_3$) and a gas chamber. The experiments were executed with a CO_2 flow of 10 mL min^{-1}. Gas bags (0.6 L, Sigma Aldrich) and liquid samples were collected every 30 minutes.

A Metrohm Echo Chemie Autolab PGSTAT128N or PGSTAT204 potentiostat controlled by NOVA software was used for all electrochemical experiments.

3.4.5 Product analysis

Gas chromatography with thermal conductivity detector (GC-TCD)

The gaseous samples were analyzed using gas chromatography (GC, Shimadzu 2010) equipped with three columns (two Poraplot Q (25 m x 0.53 mm), thickness: 20 µm, one Cp-Molsieve (5A 50 m x 0.53 mm), ID: 50 µm) and a 25 µL sample loop. The used temperature program was 60 °C for 6.3 min followed by a heating rate of 15° min^{-1} to 150 °C for 2 minutes. The thermal conductivity detector (TCD) operated under a helium flow of 10 mL min^{-1} at 250 °C and the product determination was performed using calibration curves for each gaseous product.

High pressure liquid chromatography (HPLC)

The formate detection was performed using high pressure liquid chromatography (HPLC, Shimadzu LC20A) with a Rezex ROA-Organic Acid H+ (8%) column (Phenomenex). For formate determination, an isocratic separation with 0.005 N H_2SO_4 was used with a flow of 0.5 mL min^{-1}. Quantification was done using calibration curves between 0.3 and 100 mM. For that, a sample of 150 µL was taken during the process and 10 µL were injected at the equipment.

Nuclear magnetic resonance (NMR) spectroscopy

Nuclear magnetic resonance (NMR) spectroscopy was carried out in a JEOL JNM ECA 400MHz spectrometer. For the experiments, the following parameters were used: 25 °C, 90 ° pulse, NS of 128, relaxation time of 18 s and water suppression of 40 DB. The internal standard 3-(trimethylsilyl) propanoic acid sodium salt-D4 dissolved in deuterium oxide was used for product quantification.

3.5 Supporting information

Table S3.1. Current densities [mA cm^{-2}] of the different copper catalysts in argon and CO_2 saturated 0.5 M $KHCO_3$.

	CO_2 saturated 0.5 M $KHCO_3$															
	copper nanopowder				**copper (II) oxide**				**copper acetate**				**copper (I) oxide**			
DES	**425**	**450**	**475**	**500**	**425**	**450**	**475**	**500**	**425**	**450**	**475**	**500**	**425**	**450**	**475**	**500**
CF	6	7	6	8.5	9	8	8	7.5	7	5.5	7	8.5	5.5	9	9	10
CV	10	10.5	10	13	14	16	13	8.5	8.5	6.5	6.5	7.5	10	7	7	6.5
DF	9	10	8.5	10	9	-	-	-	-	-	10	9	9	10.5	9	9
DL	3	3.5	3	4	2	3	4	8	3.5	3	3.5	3.5	3.5	5	6	4
UG	10	10	9	17	5	6	5	3	5	6	4.5	9	5.5	4.5	8	5.5
UGF	7	6	5	6.5	3	2.5	4	3	3	4	3	3.5	4	4	3.5	4
	Argon saturated 0.5 M $KHCO_3$															
	copper nanopowder				**copper (II) oxide**				**copper acetate**				**copper (I) oxide**			
DES	**425**	**450**	**475**	**500**	**425**	**450**	**475**	**500**	**425**	**450**	**475**	**500**	**425**	**450**	**475**	**500**
CF	3.8	6.5	4.5	8.5	5	5	5	5.5	5.5	5.5	6	5.5	4.5	7	6	7
CV	6	4.5	5	4	4.5	6	4	4	8	6	5	7.5	4.5	4.5	4	5
DF	5.5	10	6	4.5	14	-	-	-	-	-	5.5	9	13	11	12	13
DL	4	4.5	5.5	5	5	7	4	6	7	2	4.5	3.5	6	3	8	7.5
UG	6	7	8	14	6	4.5	2.5	3	3.5	4	2.5	3	2	2	2	2.5
UGF	3	4	3	4	2	2	4	3	3	3	2.5	2	3	4	2.5	3

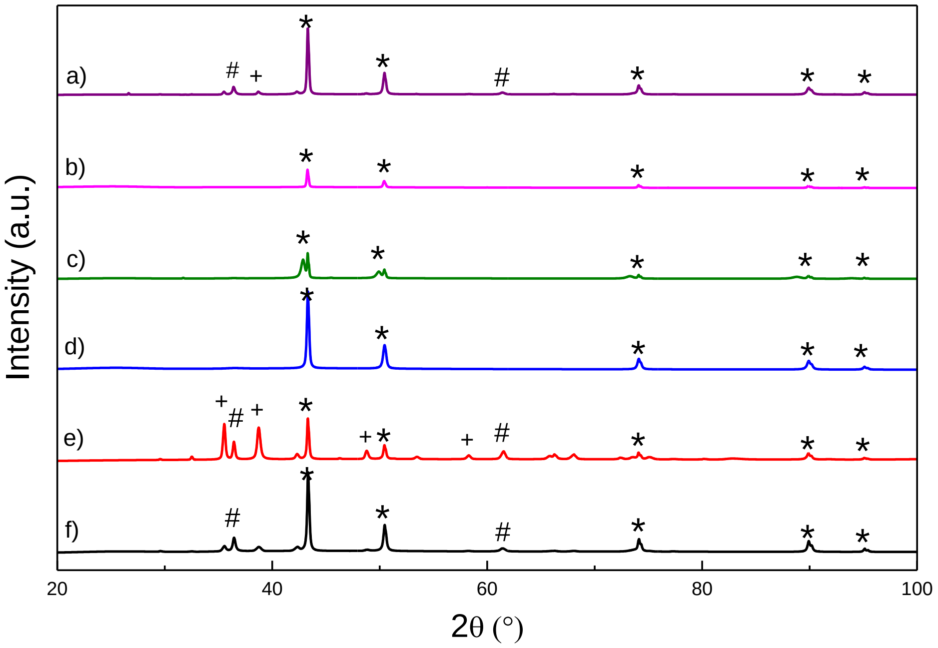

Figure S3.1. XRD patterns of a) CFCuNP450, b) CVCuNP450, c) DFCuNP450, d) DLCuNP450, e) UGCuNP450, f) UGFCuNP450. Peak signs indicate Cu (*), Cu_2O (#) and CuO (+). The following crystallography open database (COD) IDs were used for comparison: Cu (PDF card number: 7101264, space group: F m -3 m), Cu_2O (PDF card number: 9005769, space group: P n -3:1), CuO (PDF card number: 9016326, space group: C 1 c 1).

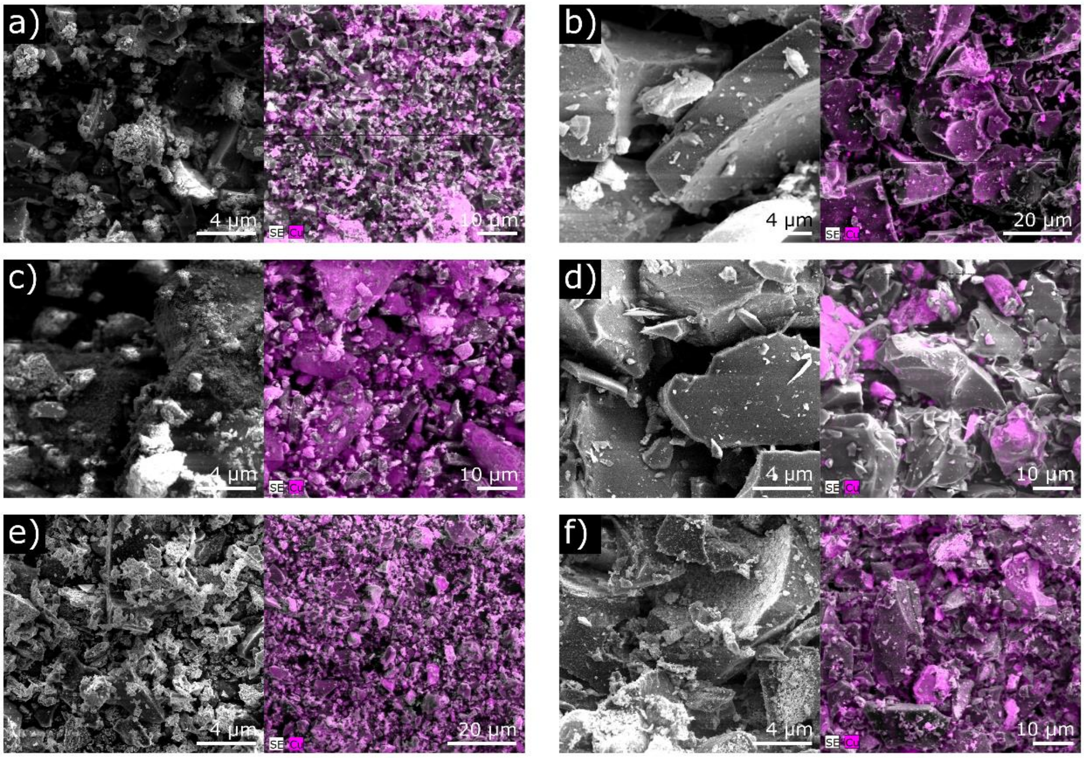

Figure S3.2. SEM micrographs and EDX mapping of Cu (purple) for the supported copper catalysts prepared from different DES with copper nanoparticles as precursor and a pyrolysis temperature of 450 °C: a) CFCuNP450. b) CVCuNP450. c) DFCuNP450. d) DLCuNP450. e) UGCuNP450. f) UGFCuNP450.

Table S3.2. Comparison of the crystallite sizes determined by XRD compared with the formate concentration obtained after 2 hours of electrochemical CO_2 reduction.

Catalyst	c (Formate) [mM]	crystallite size [nm]
CFCuNP450	22.40	41.8
CVCuNP450	20.60	52.3
DFCuNP450	12.30	38.8
DLCuNP450	16.60	33.8
UGCuNP450	7.80	50.2
UGFCuNP450	18.80	42.4
CFCuO425	34.20	51.8
CVCuNP425	31.30	58.8
CVCuNP475	24.90	50.6
CVCuNP500	15.50	49.9
CVCuO425	32.80	66.7
CVCuO450	22.40	68.2
CVCuO475	23.90	61.4
CVCuO500	19.80	62.8
CVCu$_2$O425	23.40	57.1
CVCuAc425	22.30	63.5
UGCuNP425	13.70	45.9
UGCuNP475	15.40	44.8
UGCuNP500	17.00	47.0

Table S3.3. Results of Boehm titrations of the different deep eutectic solvents without copper loading after pyrolysis at 440 °C.

DES	Acidic [µmol g^{-1}]	Basic [µmol g^{-1}]
CF	396	492
CV	635	512
DF	312	1077
DL	789	684
UG	934	1156
UGF	535	1317
com. AC	588	506

Table S3.4. CO_2 adsorption measurements of commercial activated carbon (AC) and the supporting material prepared from the U-G DES.

	Surface area [m^2 g^{-1}]	Micropores [m^2 g^{-1}]	External surface area [m^2 g^{-1}]	Micropore volume [cc g^{-1}]	Adsorbed CO_2 at rel. pressure of 0.03 [mL g^{-1}]
com. AC	202.57	53.72	148.85	0.003	9.38
CV	104.57	45.31	59.26	0.005	3.96
UG	64.36	25.90	38.46	0.005	2.60

Table S3.5. Blank experiments using a bare gas diffusion layer and the different supporting carbon materials (without copper) coated with Nafion® on a GDL.

Electrode	c(H_2) [%]	c(CO) [%]	c(Formate) [mM]	FE (Formate) [%]	total FE [%]
GDL	-	-	0.53	0.73	0.9
CF	-	0.012	1.84	5.45	5.84
CV	-	0.010	0.23	0.30	0.53
DF	-	-	-	-	-
DL	-	-	-	-	-
UG	-	-	-	-	-
UGF	-	-	-	-	-

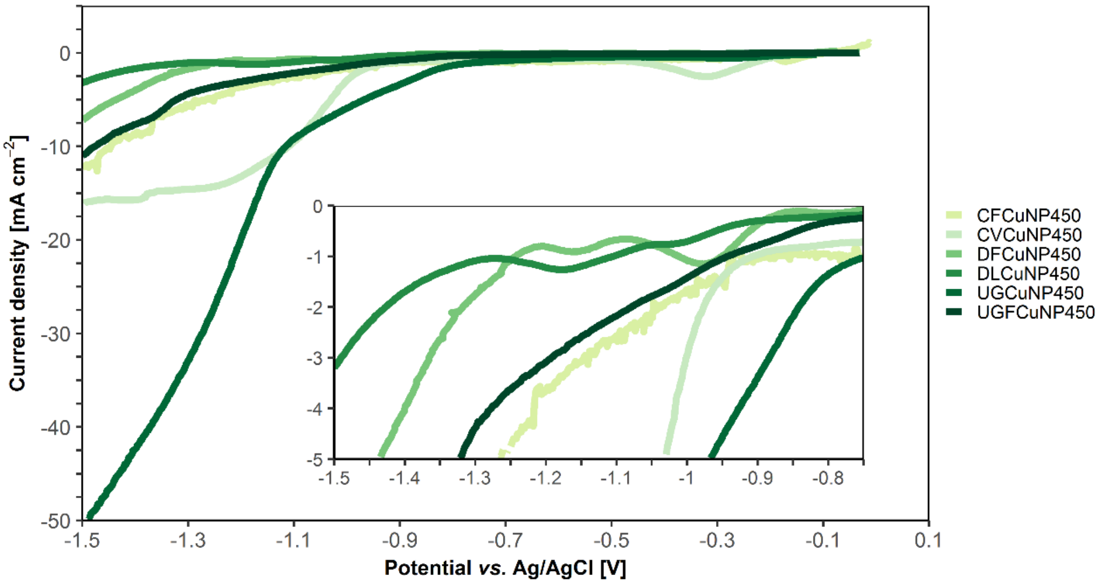

Figure S3.3. LSV measurements of catalysts prepared with different DES from CuNP at 450° C. LSV are recorded in 0.5 M CO_2 saturated $KHCO_3$ electrolyte with a scan rate of 50 mV s^{-1}.

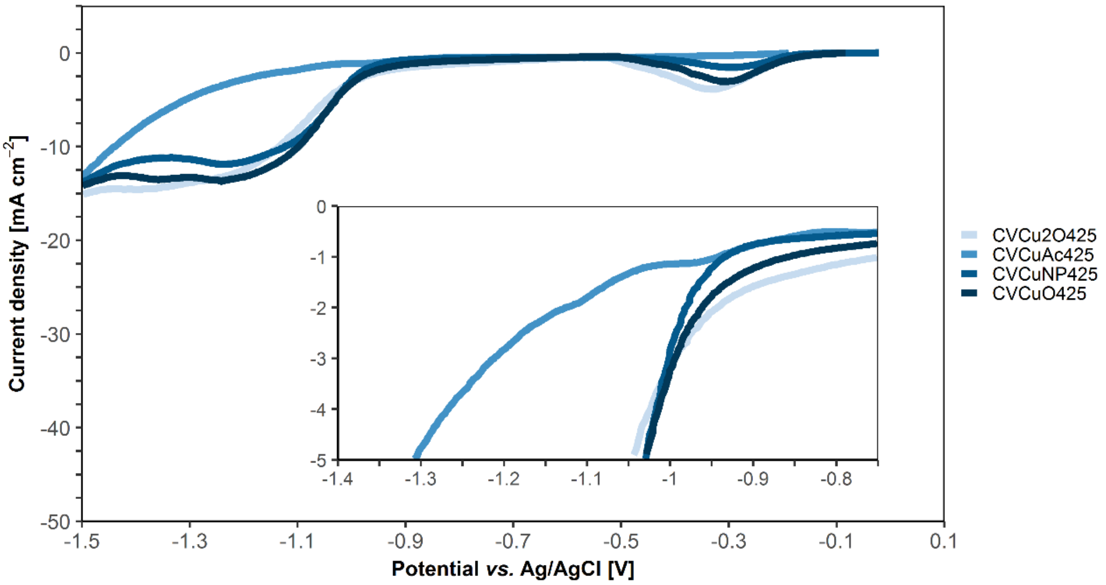

Figure S3.4. LSV measurements of catalysts prepared with different copper precursor at 425 °C from the DES CV. LSV are recorded in 0.5 M CO_2 saturated $KHCO_3$ electrolyte with a scan rate of 50 mV s^{-1}.

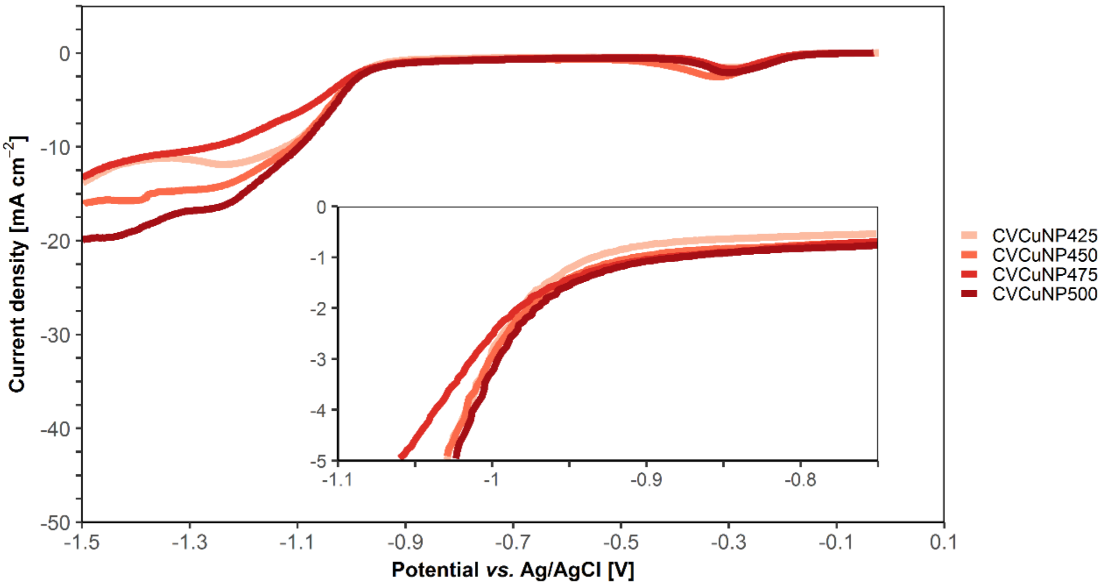

Figure S3.5. LSV measurements of catalysts prepared from CuNP and CV DES at different pyrolysis temperatures. LSV are recorded in 0.5 M CO_2 saturated $KHCO_3$ electrolyte with a scan rate of 50 mV s^{-1}.

Table S3.6. Potential screening with product analysis (Faraday efficiency FE in %) for the potential optimization. For determination of the product amount, the concentrations were subtracted from the previous values.

Potential	Formate	CO	H_2	Ethen	MeOH	EtOH	n-PrOH	total
-1.3 V	0.66	0.0	0.0	0.0	0.0	0.0	0.0	0.66
-1.5 V	7.46	5.31	43.73	0.0	0.0	0.0	0.0	56.5
-1.7 V	6.77	7.56	27.92	0.0	0.02	0.78	0.36	43.4
-1.9 V	9.43	11.29	65.81	8.29	0.01	0.79	1.52	97.2
-2.1 V	11.59	10.73	34.37	2.46	0.02	2.01	1.30	62.5

.

Table S3.7. Overview of the formate concentration, formate Faraday efficiency (FE), current density and formate formation rate for the electrochemical measurements with different catalysts in CO_2 saturated 0.5 M $KHCO_3$ solution.

Catalyst	c(Formate) [mM]	FE(Formate) [%]	Current density [mA cm^{-2}]	Formation rate [µmol h^{-1} cm^{-2}]
CFCuNP450	22.40	16.47	23.40	56.00
CVCuNP450	20.60	19.68	15.82	51.40
DFCuNP450	12.30	9.73	18.11	30.75
DLCuNP450	16.60	19.34	10.21	41.50
UGCuNP450	7.80	5.77	21.76	19.50
UGFCuNP450	18.80	11.23	27.62	47.00
CFCuO425	34.20	28.39	18.80	85.50
CVCuNP425	31.30	31.10	12.52	78.25
CVCuNP475	24.90	20.50	16.14	62.25
CVCuNP500	15.50	12.79	17.26	38.75
CVCuO425	32.80	26.11	16.54	82.00
CVCuO450	22.40	20.75	14.22	56.00
CVCuO475	23.90	19.79	18.04	59.75
CVCuO500	19.80	16.49	16.31	49.50
CVCu$_2$O425	23.40	18.38	17.83	58.50
CVCuAc425	22.30	18.47	16.18	55.75
UGCuNP425	13.70	7.88	36.50	34.25
UGCuNP475	15.40	9.64	30.63	38.50
UGCuNP500	17.00	10.23	30.92	42.50

3.6 Additional results - Novel nitrogen-rich low melting mixtures

3.6.1 Low melting mixtures screening with nitrogen-rich starting materials

For investigation of the influence of CO_2 binding domains on the catalyst activity in form of amines in the supporting materials, a screening of novel low melting mixtures with nitrogen-rich starting materials was performed. An overview of all tested mixtures and the resulting melting points are shown in Table A3.1. The green marked mixtures were chosen for preparation of supporting materials using the molar ratios shown in Table A3.2. The pyrolysis of the low melting mixtures was carried by round-bottom flask method at 440 °C as described in Chapter 2.4.2 without adding a metal salt.

Table A3.1. Overview of all investigated mixtures with nitrogen-rich starting materials. The green marked mixtures were used for the preparation of CNO supporting materials. Melting points were determined by differential scanning calorimetry (DSC) measurements.

HBD	**HBA**	**liquid < 130 °C**	**T_m [°C]**
chitosan oligomer	urea	✓	124
chitosan oligomer	N,N'-dimethylurea	✓	94 - 98
chitosan oligomer	choline chloride	x	
chitosan polymer	urea	x	
D-fructose	4-aminoantipyrine	✓	97 and 100
D-fructose	malonamide	✓	
D-fructose	guanine	x	
D-fructose	uric acid	x	
D-fructose	benzimidazole	✓	
glucosamine hydrochloride	urea	✓	115
glucosamine hydrochloride	N,N'-dimethylurea	x	
glucosamine hydrochloride	choline chloride	x	
glucosamine hydrochloride	4-aminoantipyrine	x	
glucosamine hydrochloride	malonamide	x	-
D-glucose	4-aminoantipyrine	✓	104
D-glucose	malonamide	✓	
D-glucose	guanine	x	
D-glucose	uric acid	x	
D-glucose	benzimidazole	✓	
guanidine hydrochloride	uric acid	x	
guanidine hydrochloride	4-aminoantipyrine	✓	76
urea	benzimidazole	✓	
urea	4-aminoantipyrine	✓	96
L-arginine monohydrochloride	urea	✓	113

L-arginine monohydrochloride	N,N'-dimethylurea	x	
L-arginine monohydrochloride	choline chloride	x	
L-arginine monohydrochloride	betaine hydrochloride	x	
L-histidine	urea	x	
L-histidine	N,N'-dimethylurea	x	
L-histidine	choline chloride	x	
N-acetyl-D-glucosamine	urea	✓	120
N-acetyl-D-glucosamine	N,N'-dimethylurea	x	
N-acetyl-D-glucosamine	choline chloride	✓	
N-acetyl-D-glucosamine	betaine hydrochloride	x	

Table A3.2. Investigated molar ratios for the different low melting mixtures used for preparation of the supporting materials. [a] mass ratio instead of molar ratio.

HBA	HBD	HBA:HBD (mol)	Abbreviation
urea	glucosamine hydrochloride	4:1	U-GlHCl
urea	N-acetyl-D-glucosamine	4:1	U-NAGl
urea	chitosan oligomer	2:1[a]	U-Ch
urea	L-arginine monohydrochloride	4:1	U-ArHCl
4-aminoantipyrine	urea	1:1	AA-U
4-aminoantipyrine	guanidine hydrochloride	2:1	AA-GuHCl
4-aminoantipyrine	D-fructose	1:1	AA-F
4-aminoantipyrine	D-glucose	1:1	AA-G
malonamide	glucosamine hydrochloride	3:1	M-GlHCl
N,N'-dimethylurea	chitosan oligomer	2:1[a]	D-Ch

3.6.2 Elemental composition of the prepared supporting materials

Elemental composition of the prepared supporting materials was investigated by CHNS/O elemental analysis. The DES based on urea and D-glucose showed in previous studies the highest nitrogen content (20.8 wt%). Table A3.3 shows an overview of the composition of the supporting materials prepared from the novel nitrogen-rich low melting mixtures. The nitrogen-content could be increased to 25.9 wt% with the new low melting mixture urea - L-arginine monohydrochloride (U-ArHCl).

Table A3.3. Elemental composition of the prepared supporting materials from new nitrogen-rich DES.

Mischung	ω(C) [wt%]	ω(N) [wt%]	ω(O) [wt%]	ω(H) [wt%]
U-GlHCl	55.6	20.1	20.0	4.3
U-NAGl	61.7	22.4	12.4	3.5
U-Ch	59.6	21.7	15.3	3.4
U-ArHCl	60.7	25.9	10.3	3.2
AA-U	60.9	23.6	11.1	4.4
AA-GuHCl	63.3	22.9	10.2	3.7
AA-F	72.9	13.6	9.8	3.8
AA-G	74.4	14.6	6.8	4.2
M-GlHCl	64.4	16.7	15.5	3.4
D-Ch	67.5	16.3	12.4	3.7

3.6.3 Copper supported on the nitrogen-rich supporting material - Electrochemical CO_2 reduction

The catalyst was prepared using the new low melting mixture U-ArHCl in a round-bottom flask according to the method shown in Chapter 3.4.2. To obtain a theoretical copper loading of 50 wt% in the final nitrogen-rich material (Cu/CNO), 1.13 g of CuNP were added to the mixture and the final temperature used for the preparation was 450 °C.

The electrode was coated with 5 mg cm^{-2} of the prepared catalyst and used for electrochemical CO_2 reduction in a 3-compartment cell at -1.5 V *vs.* Ag/AgCl for two hours in 0.5 M $KHCO_3$. The resulting products are summarized in Table A3.4.

Table A3.4. Results of electrochemical CO_2 reduction using the copper catalyst prepared from the novel low melting mixture with the highest nitrogen content U-ArHCl.

c(Formate) [mM]	FE(Formate) [%]	Current density [mA cm^{-2}]	Formation rate [µmol h^{-1} cm^{-2}]
4.4	6.2	9.02	11.0

Compared to the overview of all tested catalysts, shown in Table S3.7, the prepared nitrogen-rich copper catalyst leads to the lowest formate formation rate. Thus, an increase of the nitrogen content in the supporting materials diminishes the catalyst performance in the electrochemical CO_2 reduction to formate. This result confirms the tendency found in Chapter 3.2.2 that a higher nitrogen content in the supporting material results in lower formate formation rates.

3.7 References

[1] C. Costentin, M. Robert, J.-M. Savéant, *Chemical Society Reviews* **2013**, *42*, 2423-2436.

[2] M. Grasemann, G. Laurenczy, *Energy & Environmental Science* **2012**, *5*, 8171-8181.

[3] M. Pérez-Fortes, J. C. Schöneberger, A. Boulamanti, G. Harrison, E. Tzimas, *International Journal of Hydrogen Energy* **2016**, *41*, 16444-16462.

[4] J. Hietala, A. Vuori, P. Johnsson, I. Pollari, W. Reutemann, H. Kieczka, *Formic Acid*, **2016**.

[5] J. Albo, D. Vallejo, G. Beobide, O. Castillo, P. Castaño, A. Irabien, *ChemSusChem* **2017**, *10*, 1100-1109.

[6] C. Finn, S. Schnittger, L. J. Yellowlees, J. B. Love, *Chemical Communications* **2012**, *48*, 1392-1399.

[7] D. Du, R. Lan, J. Humphreys, S. Tao, *Journal of Applied Electrochemistry* **2017**, *47*, 661-678.

[8] M. Rumayor, A. Dominguez-Ramos, A. Irabien, *Applied Sciences* **2018**, *8*, 914.

[9] S. M. Benson, F. M. Orr, *MRS Bulletin* **2011**, *33*, 303-305.

[10] F. A. Rahman, M. M. A. Aziz, R. Saidur, W. A. W. A. Bakar, M. R. Hainin, R. Putrajaya, N. A. Hassan, *Renewable and Sustainable Energy Reviews* **2017**, *71*, 112-126.

[11] D. Y. C. Leung, G. Caramanna, M. M. Maroto-Valer, *Renewable and Sustainable Energy Reviews* **2014**, *39*, 426-443.

[12] H.-R. M. Jhong, S. Ma, P. J. A. Kenis, *Current Opinion in Chemical Engineering* **2013**, *2*, 191-199.

[13] D. T. Whipple, P. J. A. Kenis, *The Journal of Physical Chemistry Letters* **2010**, *1*, 3451-3458.

[14] B. Kumar, J. P. Brian, V. Atla, S. Kumari, K. A. Bertram, R. T. White, J. M. Spurgeon, *Catalysis Today* **2016**, *270*, 19-30.

[15] M. Azuma, K. Hashimoto, M. Hiramoto, M. Watanabe, T. Sakata, *Journal of Electroanalytical Chemistry and Interfacial Electrochemistry* **1989**, *260*, 441-445.

[16] Y. Hori, A. Murata, R. Takahashi, S. Suzuki, *Journal of the Chemical Society, Chemical Communications* **1988**, 17-19.

[17] C. W. Li, M. W. Kanan, *Journal of the American Chemical Society* **2012**, *134*, 7231-7234.

[18] W. Tang, A. A. Peterson, A. S. Varela, Z. P. Jovanov, L. Bech, W. J. Durand, S. Dahl, J. K. Nørskov, I. Chorkendorff, *Physical Chemistry Chemical Physics* **2012**, *14*, 76-81.

[19] K. P. Kuhl, E. R. Cave, D. N. Abram, T. F. Jaramillo, *Energy & Environmental Science* **2012**, *5*, 7050-7059.

[20] J. Hussain, H. Jónsson, E. Skúlason, *ACS Catalysis* **2018**, *8*, 5240-5249.

[21] R. Kortlever, J. Shen, K. J. P. Schouten, F. Calle-Vallejo, M. T. M. Koper, *The Journal of Physical Chemistry Letters* **2015**, *6*, 4073-4082.

[22] R. Kortlever, I. Peters, S. Koper, M. T. M. Koper, *ACS Catalysis* **2015**, *5*, 3916-3923.

[23] Y. Hori, H. Wakebe, T. Tsukamoto, O. Koga, *Electrochimica Acta* **1994**, *39*, 1833-1839.

[24] M. Gattrell, N. Gupta, A. Co, *Journal of Electroanalytical Chemistry* **2006**, *594*, 1-19.

[25] Y. Hori, A. Murata, R. Takahashi, *Journal of the Chemical Society, Faraday*

Transactions 1: Physical Chemistry in Condensed Phases **1989**, *85*, 2309-2326.

[26] Y. Hori, in *Modern Aspects of Electrochemistry* (Eds.: C. G. Vayenas, R. E. White, M. E. Gamboa-Aldeco), Springer New York, New York, NY, **2008**, pp. 89-189.

[27] **2018**.

[28] M. Iwanow, J. Finkelmeyer, A. Söldner, M. Kaiser, T. Gärtner, V. Sieber, B. König, *Chemistry – A European Journal* **2017**, *23*, 12467-12470.

[29] N. A. Brunelli, S. A. Didas, K. Venkatasubbaiah, C. W. Jones, *Journal of the American Chemical Society* **2012**, *134*, 13950-13953.

[30] Y. G. Ko, S. S. Shin, U. S. Choi, *Journal of Colloid and Interface Science* **2011**, *361*, 594-602.

[31] F. T. L. Muniz, M. A. R. Miranda, C. Morilla dos Santos, J. M. Sasaki, *Acta Crystallographica Section A* **2016**, *72*, 385-390.

[32] R. Reske, H. Mistry, F. Behafarid, B. Roldan Cuenya, P. Strasser, *Journal of the American Chemical Society* **2014**, *136*, 6978-6986.

[33] D. V. Wagle, H. Zhao, G. A. Baker, *Accounts of Chemical Research* **2014**, *47*, 2299-2308.

[34] A. M. Kalijadis, M. M. Vukčević, Z. M. Jovanović, Z. V. Laušević, M. D. Laušević, *Journal of the Serbian Chemical Society* **2011**, *5*, 757-768.

[35] M. S. Shafeeyan, W. M. A. W. Daud, A. Houshmand, A. Shamiri, *Journal of Analytical and Applied Pyrolysis* **2010**, *89*, 143-151.

[36] J. Garrido, A. Linares-Solano, J. M. Martin-Martinez, M. Molina-Sabio, F. Rodriguez-Reinoso, R. Torregrosa, *Langmuir* **1987**, *3*, 76-81.

[37] M. N. Mahmood, D. Masheder, C. J. Harty, *Journal of Applied Electrochemistry* **1987**, *17*, 1159-1170.

[38] H.-R. M. Jhong, F. R. Brushett, P. J. A. Kenis, *Advanced Energy Materials* **2013**, *3*, 589-599.

[39] C.-T. Dinh, T. Burdyny, M. G. Kibria, A. Seifitokaldani, C. M. Gabardo, F. P. García de Arquer, A. Kiani, J. P. Edwards, P. De Luna, O. S. Bushuyev, C. Zou, R. Quintero-Bermudez, Y. Pang, D. Sinton, E. H. Sargent, *Science* **2018**, *360*, 783-787.

[40] J. Qiao, Y. Liu, F. Hong, J. Zhang, *Chemical Society Reviews* **2014**, *43*, 631-675.

[41] K. Gupta, M. Bersani, J. A. Darr, *Journal of Materials Chemistry A* **2016**, *4*, 13786-13794.

[42] T. N. Huan, P. Simon, G. Rousse, I. Génois, V. Artero, M. Fontecave, *Chemical Science* **2017**, *8*, 742-747.

[43] E. Takeshi, S. J. L. Billinge, in *Pergamon Materials Series, Vol. 16* (Eds.: T. Egami, S. J. L. Billinge), Pergamon, **2012**, pp. 1-25.

[44] P. Juhas, T. Davis, C. L. Farrow, S. J. L. Billinge, *Journal of Applied Crystallography* **2013**, *46*, 560-566.

[45] A. M. Oickle, S. L. Goertzen, K. R. Hopper, Y. O. Abdalla, H. A. Andreas, *Carbon* **2010**, *48*, 3313-3322.

[46] S. L. Goertzen, K. D. Thériault, A. M. Oickle, A. C. Tarasuk, H. A. Andreas, *Carbon* **2010**, *48*, 1252-1261.

CHAPTER 4

4 Enhanced C2 and C3 Product Selectivity in electrochemical CO_2 Reduction on Copper Oxide Catalysts prepared by Deep Eutectic Solvent Calcination

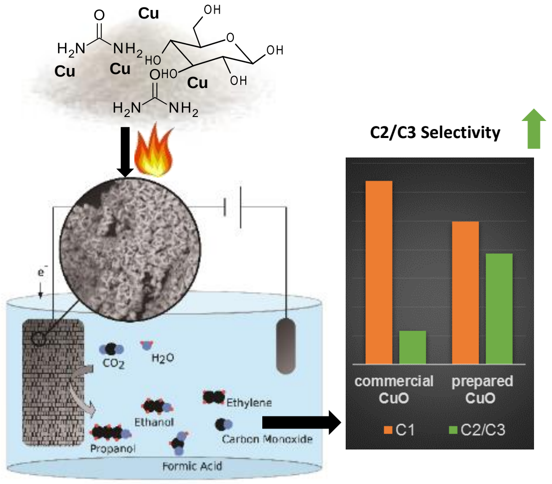

This chapter has been submitted as:

M. Iwanow, J. Pößnecker, L. Vieira, M. Kaiser, D. Van Opdenbosch, C. Zollfrank, T. Gärtner, B. König, V. Sieber, *Advanced Functional Materials* **2019**, submitted.

MI developed the synthesis method and carried out the preparation and characterization of catalyst Cu-a, Figure 4.6b, crystallite size calculation, developed analytical methods and wrote the manuscript. JP synthesized the catalysts Cu-b to Cu-g and carried out electrochemical experiments during his internship and Master thesis under supervision of MI and LV. MK developed the GC method for gaseous products. DVO supported the evaluation of XRD. LV, TG, VS and BK supervised the project. VS is the corresponding author.

4.1 Introduction

The rising concentration of global atmospheric carbon dioxide since the beginning of industrialization (280 part per million by volume (ppmv) to 365 ppmv)[1] requires a reduction of carbon dioxide release and solutions for its capture and utilization.[2-4] For CO_2 capture, several technologies have been developed involving point sources or direct air capture.[5] As for the CO_2 utilization, using CO_2 for chemical synthesis of industrial relevant chemicals would be a sustainable solution not only for the utilization, but also for the replacement of fossil based chemicals by CO_2-neutral alternatives. In this way, the electrochemical reduction of CO_2 is a promising conversion method towards a carbon-neutral economy by using directly renewable electricity. The electrochemical carbon dioxide reduction (CO_2R) process can use CO_2 as building block for the synthesis of several value-added products. Moreover, CO_2R offers a possibility for storing intermittent renewable energy, as wind and solar, since it would be in principle relatively simple to ramp up and down according to the energy availability.[6-8]

Mild reaction conditions (ambient pressure and temperature) and the use of low-cost catalysts are key advantages of the electrocatalytic CO_2 conversion in aqueous media, making it a particularly promising method.[9-10] Nevertheless, the electrochemical CO_2 reduction competes with the hydrogen evolution reaction (HER). Therefore, a powerful catalyst is required to favour the CO_2 reduction and suppress hydrogen production. In contrast to many other catalyst materials, copper and its oxides CuO and Cu_2O catalyze the generation of numerous products from CO_2 and are one of the few materials, which lead to the formation of C-C bonds.[8, 11] Depending on the potential, surface morphology and oxidation state of the catalyst, a wide variety of products can be obtained in different ratios: carbon monoxide, methane, ethylene, methanol, ethanol, n-propanol, and formate (Table 4.1).[11-14] In addition, the preparation method of the Cu-based catalysts or electrodes can have an effect on the selectivity of product formation.

Table 4.1. CO_2 reduction products on the cathode with their respective potentials at pH 7.[15-16]

Chemical equations	Potential *V vs.* SHE
$CO_2 + H_2O + 2\,e^- \rightarrow HCOO^-(aq) + OH^-$	- 0.43 V
$CO_2 + H_2O + 2\,e^- \rightarrow CO\uparrow + 2\,OH^-$	- 0.52 V
$2\,CO_2 + 8\,H_2O + 12\,e^- \rightarrow C_2H_4\uparrow + 12\,OH^-$	- 0.34 V
$2\,CO_2 + 9\,H_2O + 12\,e^- \rightarrow C_2H_5OH\,(aq) + 12\,OH^-$	- 0.33 V
$3\,CO_2 + 13\,H_2O + 18\,e^- \rightarrow C_3H_7OH\,(aq) + 18\,OH^-$	- 0.32 V

Various copper and copper oxide materials have been reported in the literature as catalysts for electrochemical CO_2 reduction.[13-14, 17-19] Yet, most methods for catalyst synthesis are demanding and time consuming. Herein, we report a novel and facile preparation method of copper oxide and its application as catalysts for electrochemical CO_2 reduction. The materials were prepared by a slight modification of the deep eutectic solvent (DES) pyrolysis method, previously described by our group.[20-21] The initial method was based on the pyrolysis of Cu-containing DES in an inert nitrogen atmosphere, which led to copper materials embedded in a carbon support (Cu/CNO). Such materials showed high selectivity for the production of formate from CO_2 electrolysis.[21]

In the current preparation method, the calcination atmosphere has been changed from N_2 to air resulting in partially oxidized copper due to the oxidative conditions. In contrast to the previous catalyst preparation method, whereby mainly formate was produced in the CO_2R, the newly produced CuO/CNO showed higher selectivity for C2 (ethylene, ethanol) and C3 (n-propanol) molecules during electrochemical CO_2 reduction. Compared to commercial copper(II) oxide nanoparticles, the activities and selectivities of the as-prepared catalysts are significantly higher. Thus, we could tailor the synthesis method to improve the productivity and selectivity of the catalysts. The influence of calcination time (10 min, 15 min or 60 min) in the oxidative atmosphere as well as the influence of different deep eutectic solvents and copper precursors on the catalytic activity of the prepared materials were investigated in detail.

4.2 Results and discussion

4.2.1 Catalyst synthesis and characterization

Different materials were produced by systematically varying the preparation parameters such as type of DES, copper precursor, pre-treatment atmosphere, calcination time and temperature. The pre-treatment step was carried out in inert or air atmosphere for 1.5 hours. This step enables a homogeneous and controlled thermal treatment of the material under stirring of the copper-containing DES. After the pre-heating, the resulting solid mixture is transferred to an evaporating dish and calcined in a muffle furnace under air or N_2. Pyrolysis under inert gas leads to an end mixture of copper in a carbon support (Cu/CNO).[21] Calcination in air leads to a considerably lower content of CNO due to the oxidation of the DES and release as gases, and to the oxidation of copper species to CuO. In this work, we have mainly focused on the calcination in air for the preparation of CuO. These oxide materials were further used as catalysts for electrochemical CO_2 reduction.

The catalyst Cu-a, which was prepared from the DES urea - ᴅ-glucose (UG), copper nanoparticles (CuNP), pre-treated and calcined for 60 minutes at 500 °C, both in air, was set as benchmark for the materials synthesis. Following materials were prepared changing the DES to urea - ᴅ-galactose (UGa, Cu-b), the copper precursor to CuO (Cu-c), the calcination time to 15 minutes in air (Cu-d) or the pre-treatment atmosphere to nitrogen (Cu-g). Since the remaining supporting material (CNO) can influence the catalyst activity[21], the preparation method was slightly modified for Cu-e and Cu-f in order to increase the amount of CNO in the final material. Cu-e and Cu-f were firstly pre-treated under nitrogen. After cooling to room temperature, the mixture was transferred to an oven and heated up to 450 °C (Cu-e) or 500 °C (Cu-f), also under nitrogen atmosphere. Subsequently, the atmosphere was changed to air and the temperature was raised to 500 °C (Cu-e) or 550 °C (Cu-f) and kept for 10 minutes. In this way, carbon-supported copper oxide catalysts (CuO/CNO) should be obtained.

The influence of the preparation methods on the morphologies and elemental compositions of the prepared materials were analyzed by SEM and EDX. Figure 4.1I shows the SEM images for Cu-b (a) and Cu-f (b) and the respective EDX analysis in two different spots. Cu-b was calcined in air only, whereas Cu-f was thermally treated in two steps, first in nitrogen then in air atmosphere.

Catalysts prepared by 60 minutes calcination in air (Cu-a, Cu-b, Cu-c and Cu-g) exhibit in general a quite homogeneous morphology, as shown exemplarily in Figure 4.1-Ia for Cu-b. EDX analysis reveals that Cu-b is rich in copper with a low content of carbonaceous supporting material, similarly to Cu-a, Cu-c and Cu-g. The copper content in these materials lay between 72.8 wt% and 80.3 wt% with less than 6.6 wt% of supporting material. Catalysts Cu-d, Cu-e and Cu-f with a shorter thermal treatment in air (10 min or 15 min in air) show two different types of particle morphology, as depicted in the SEM image of Cu-f (Figure 4.1-Ib). EDX of the catalyst Cu-f, which was firstly thermally treated in an inert atmosphere, reveals a higher concentration of carbonaceous material compared to samples treated in air only and similarly to Cu-d and Cu-e. Moreover, EDX analysis show different composition for the different particle types: (+) CuO domains with less carbon support; and (-) CuO/CNO domains with comparable lower copper contents (< 50 wt %) and higher amounts of carbon, nitrogen and oxygen. Thus, varying treatment time in oxygen-containing atmosphere changes the ratio of Cu/C/N/O. Shorter thermal treatment time in air leads to more remaining CNO support, whereas longer pyrolysis in air mostly oxidizes the material to CuO and converts the remaining DES to CO_2. Nevertheless, the final material did not result in a homogeneous composition, indicating heterogeneous oxidation of the catalysts. More details on the preparation method and elemental composition can be found in Figure S4.1 in Chapter 4.5 and Table 4.7 in Chapter 4.4.2.

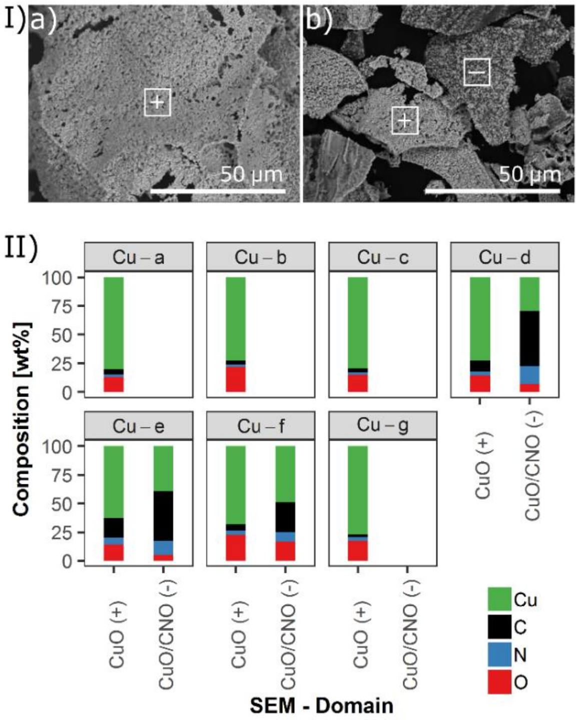

Figure 4.1. I) SEM images of a) Cu-b and b) Cu-f. II) Elemental composition (EDX) of synthesized copper catalysts Cu-a, Cu-b, Cu-c, Cu-d, Cu-e, Cu-f and Cu-g.

Different copper precursor influence the morphology of the synthesized materials. Copper nanoparticles (Cu-a, Cu-b, Cu-d, Cu-e, Cu-f and Cu-g) led to a frilled and compact structure with smooth surfaces (Cu-a, Figure 4.2a), while CuO as precursor revealed large pores and less dense ordered structure (Cu-c, Figure 4.2b). Calcination at 500 °C may lead to sintering of the copper(II) oxide in Cu-c. In addition, the carbon-rich domains of the catalysts Cu-d, Cu-e and Cu-f (CuO/CNO) show the same smooth morphology of the Cu/CNO catalysts.[21] SEM images of all prepared catalysts are shown in Figure S4.2 in Chapter 4.5.

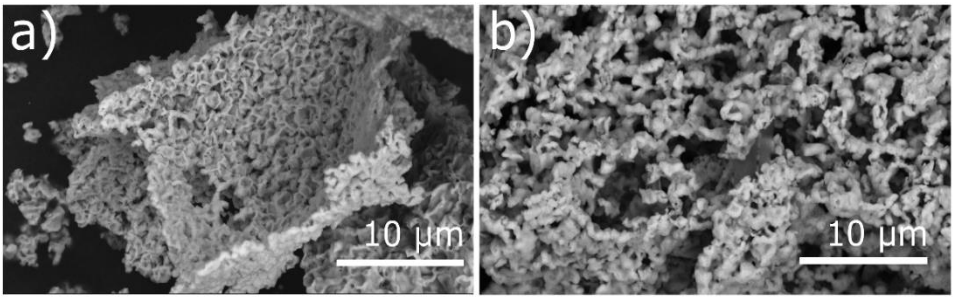

Figure 4.2. SEM images of a) Cu-a and b) Cu-c. Cu-a shows a frilled and compact CuO structure obtained from CuNP precursor and Cu-c shows large pores and a less dense ordered structure from CuO as precursor.

The effect of the annealing time and atmosphere on the oxidation of copper was additionally investigated by X-ray powder diffractometry (XRD). Different oxidation states of copper (0, +I, +II) can be observed from the reflexes (Figure S4.3 in Chapter 4.5). Cu-a, Cu-b, Cu-c and Cu-g only show reflexes attributed to copper(II) oxide and are, therefore, abbreviated in the following text as CuO-60 catalysts, due to the 60 minutes oxidative treatment. XRD of samples prepared with shorter treatment time in an O_2-containing atmosphere (Cu-d, Cu-e and Cu-f) show reflexes of less oxidized forms of copper, such as Cu_2O and Cu^0, besides CuO. Thus, longer treatment times in an O_2-containing atmosphere at 500 °C leads to higher oxidized copper species.

By applying the Scherrer equation, crystallite sizes of CuO were examined.[22] The calculation of the crystallite sizes for the CuO-60 catalysts were performed as shown in Chapter 4.5 (Figure S4.4) and are presented in real space in Table 4.2.

Table 4.2. Crystallite sizes in *x*-, *y*- and *z*-direction relative to the unit cells for the CuO-60 catalysts.

Catalyst	**D_x [nm]**	**D_y [nm]**	**D_z [nm]**
Cu-a	50.5	33.4	44.5
Cu-b	58.6	35.6	89.3
Cu-c	69.2	31.0	44.5
Cu-g	50.8	37.2	96.0

Similar sizes of the crystallites were found regarding the *x*- and *y*-direction, with exception of the Cu-c catalyst, which shows a clear deviation in *x*-direction. However, the crystallites differ strongly in *z*-direction between 44.5 nm (Cu-a, Cu-c) and 89.6 or 96.0 nm for Cu-b and Cu-g, respectively. Interestingly, the copper precursor is not the only dimension-determining factor of the crystallites, because Cu-a (CuNP) and Cu-c (CuO) exhibit an equal length in *z*-direction. However, the used deep eutectic solvent seems to influence the length of the copper crystallites in *z*-direction. This is consistent with findings from Wagle et al. that DES can fulfil multiple roles in directing chemistry at the nanoscale and thus, dictating growth along defined directions.[23] Cu-b was prepared with the DES UGa instead of UG and the preparation of Cu-g differs in the inert pre-treatment atmosphere compared to the catalysts Cu-a, Cu-b and Cu-c. Thus, during the first step of the Cu-g catalyst preparation, resulting carbon-rich supporting material from DES is available and may influence the building of copper crystallites.

4.2.2 Electrochemical measurements

Benchmark catalyst Cu-a was used for optimization of the electrochemical setup. Experiments in helium and CO_2 saturated 0.5 M $KHCO_3$ electrolytes were performed in order to verify the production of hydrocarbons by reduction of CO_2. Table 4.3 shows that only hydrogen is produced in the absence of CO_2. Thus, neither the bicarbonate electrolyte nor remnants of the pyrolysis of the deep eutectic solvents are involved in product formation, but solely CO_2 reduction.

Table 4.3. Faraday efficiencies (FE) for the synthesized copper material Cu-a in He saturated and CO_2 saturated 0.5 M $KHCO_3$, respectively at E = -1.7 V *vs.* Ag/AgCl. The pH was measured in the beginning and after 120 min of electrolysis.

	Faraday efficiency FE [%]						**total FE [%]**	**pH**
	H_2	CO	C_2H_4	$HCOO^-$	C_2H_5OH	C_3H_7OH		
He	45.05	-	-	-	-	-	45.05	8.82 → 12.79
CO_2	32.21	5.85	0.40	7.92	0.56	0.36	46.29	7.77 → 9.63

Interestingly, the overall efficiency of the catalyst does not depend on whether He or CO_2 is used for electrolyte saturation. In both cases, a total FE of ca. 45 % was obtained. In helium-saturated electrolytes, water is the only redox species available for reduction on the catalyst active sites, whereas in CO_2 saturated solutions, water and CO_2 compete for the electrode reactions. In both, He and CO_2 saturated medium, the pH of the catholyte increases considerably during the reaction (Table 4.3) due to the generation of OH^- ions from water reduction to hydrogen (Equation 1).[24-25]

$$2\,H_2O + 2\,e^- \rightarrow H_2\uparrow + 2\,OH^- \qquad (1)$$

$$OH^- + HCO_3^- \rightarrow H_2O + CO_3^{2-} \qquad (2)$$

The increase of pH may be prevented by the buffering of the produced hydroxide with HCO_3^- ions (Equation 2). The 0.5 M $KHCO_3$ is not concentrated enough to buffer the OH^-

formation and the pH rises.[25] However, the solubility of CO_2 in the electrolyte depends on the pH and is higher in more acidic solutions. In more basic solutions, the equilibrium shifts from CO_2 towards HCO_3^- and for values higher than pH 8, no aqueous CO_2 is expected to be present.[26]

To overcome the limitation of low CO_2 dissolution in aqueous solutions, experiments were carried out on gas diffusion electrodes. Thereby, the supply of CO_2 to the catalyst surface was maintained by the transport of gaseous CO_2 through the gas diffusion layer.

Besides the buffer effect, the influence of the electrolyte concentration on the electrochemical reaction and the product formation was investigated. Varying the electrolyte concentration affects the resulting current density and the selectivity of product formation.[27] In lower concentrated electrolytes, the current density decreased more rapidly, most likely due to the degradation of the anolyte. In the anode, water molecules are oxidized to molecular oxygen releasing protons (Equation 3) and the equilibrium of carbonic acid (Equation 4) shifts towards CO_2 and water.

$$2\,H_2O \;\rightarrow\; O_2\uparrow + 4\,H^+ + 4\,e^- \tag{3}$$

$$CO_2 + H_2O \leftrightarrows (H_2CO_3) \leftrightarrows HCO_3^- + H^+ \tag{4}$$

Our experiments showed that the current density drops and the anolyte had to be replaced after ~40 min in 0.1 M $KHCO_3$ and only after ~120 min in 0.5 M $KHCO_3$ (Figure S4.5 in Chapter 4.5). This reaction and the migration of potassium ions through the cation exchange membrane led to a decrease of electrolyte concentration, which reduces the conductivity and strongly increases cell resistance. Table 4.4 compares the catalyst activity in 0.1 M and 0.5 M $KHCO_3$ solutions. The formation rates of all products are higher in the concentrated 0.5 M $KHCO_3$ solution. Thus, following experiments were carried out with 0.5 M $KHCO_3$ electrolytes, since the product formation rates were higher and the electrochemical cell was more stable in this $KHCO_3$ concentration.

Table 4.4. Total product formation rates for 2 h reaction time using copper catalyst Cu-a in two different concentrated $KHCO_3$ electrolytes at E = -1.7 V *vs.* Ag/AgCl.

$KHCO_3$ concentration [M]	**Formation rates [µmol h^{-1} cm^{-2}]**						**total FE [%]**
	H_2	**CO**	**$HCOO^-$**	**C_2H_4**	**C_2H_5OH**	**C_3H_7OH**	
0.1	81.2	60.8	67.0	1.1	2.0	0.9	40.8
0.5	176.5	94.2	114.1	3.4	3.3	1.7	53.5

The effects of the catalyst loading on the gas diffusion layers and the CO_2 gas flow on product formation were investigated in 0.5 M $KHCO_3$. The product formation rate for Cu-a catalyst loadings of 5, 10 or 20 mg cm^{-2} for CO_2 gas flows of 5, 10 and 20 mL min^{-1} are shown in Figure 4.3.

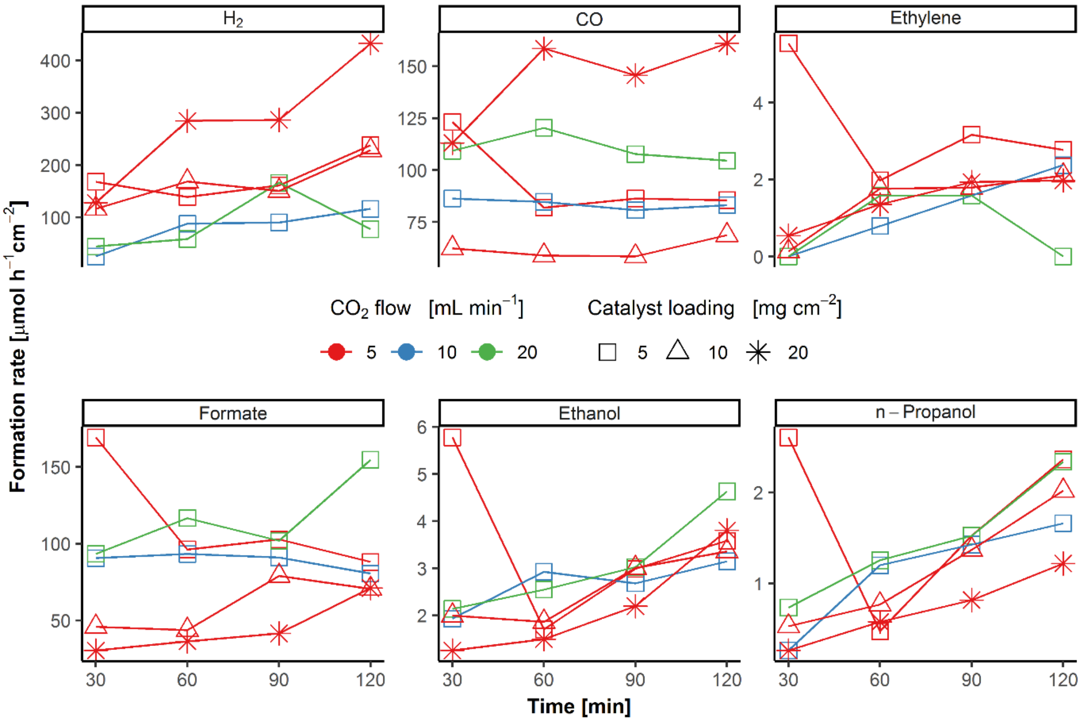

Figure 4.3. Formation rate of hydrogen, carbon monoxide, ethylene, formate, ethanol and n-propanol for different CO_2 flows and Cu-a catalyst loadings for two hours. The experiments were performed at constant potential *E* = - 1.7 V *vs.* Ag/AgCl in CO_2 saturated 0.5 M $KHCO_3$.

The variation of catalyst loading immobilized on a gas diffusion layer was investigated with a constant CO_2 gas flow of 5 mL min^{-1}. The catalyst amount influences distinctly formation rates of gaseous products. The highest hydrogen and carbon monoxide formation rates were achieved using a catalyst loading of 20 mg cm^{-2}, while ethylene shows higher formation rates on 5 mg cm^{-2}. Regarding liquid products (formate, ethanol and n-propanol), the catalyst loading shows less influence and a slight tendency towards a lower amount of catalyst was found. For example, ethanol formation rates of 3.5, 2.8 and 3.2 µmol h^{-1} cm^{-2} were obtained, when the catalyst loading was 5, 10 or 20 mg cm^{-2}, respectively. Thus, 5 mg cm^{-2} was chosen as the optimum of catalyst loading for this setup. This result is consistent to the findings of the optimum Cu/CNO catalyst amount by chronoamperometry measurements.[21]

The CO_2 gas flow, examined with 5 mg cm^{-2} of Cu-a, does not affect the product formation so significantly compared to the catalyst loading. At a higher gas flow of 20 mL min^{-1}, the formation rate of carbon monoxide increases, by a simultaneous decrease of ethylene formation. The electrochemical process was rather stable with a CO_2 gas flow of 10 mL min^{-1}, while the fluctuation for all products is high with 5 mL min^{-1}. This is in accordance to findings in literature that a higher CO_2 pressure favors the product formation from electrochemical CO_2 reduction.[28-29]

Summarizing the experiments with benchmark catalyst Cu-a, gas diffusion layers coated with a lower catalyst loading (5 mg cm^{-2}), a CO_2 gas flow of 10 mL min^{-1} and more concentrated electrolytes (0.5 M) led to higher product formation rates and better stabilities of the electrochemical CO_2 reduction. Thus, these parameters were used for all following experiments.

Using the above-mentioned parameters, the applied potential was varied between -2.1 V and -1.5 V *vs.* Ag/AgCl exemplarily for catalyst Cu-g. Faraday efficiency (FE) for the detected products shown along with the average current density at each step potential is illustrated in Figure 4.4. Carbon monoxide is produced at all potentials with FE between 6.3 % and 10.8 %. Stepping to more negative potentials from -1.9 V to -2.1 V increases the ethylene formation from 5.9 % to 8.8 %, and decreases the efficiency of formate from 11.6 % to 10.9 %. The FE of ethanol and n-propanol is the highest at -1.7 V with 4.7 % (EtOH) and 5.5 % (n-PrOH). At this potential, the overall efficiency of hydrocarbons was also the highest with 40.9 % FE. Since the highest concentration of hydrocarbons was found at -1.7 V vs. Ag/AgCl, this potential was used for all further experiments.

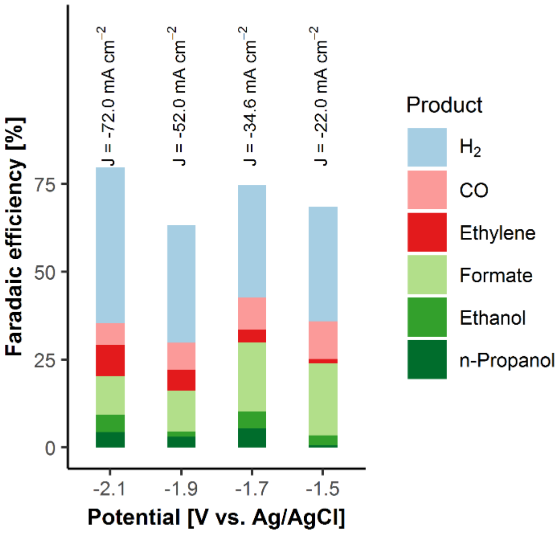

Figure 4.4. Products generated by the copper catalyst Cu-g between -2.1 V, -1.9 V, -1.7 V and -1.5 V in CO_2 saturated 0.5 M $KHCO_3$ electrolyte. The measurements were performed for half an hour at each potential.

4.2.3 Catalyst Screening

Catalysts prepared by varying the DES, copper precursor and calcination times were investigated toward their activity for CO_2 reduction using the optimized parameters.

An initial assessment of the current densities at different applied potentials in CO_2 saturated 0.5 M $KHCO_3$ was carried out by linear sweep voltammetry (LSV) and chronoamperometry (CA) (Figure 4.5). A comparison of the measurements in CO_2 and argon saturated solutions for all catalysts is shown in Figure S4.6 in Chapter 4.5.

LSV of the different copper catalysts in CO_2 saturated electrolytes shows higher current densities and more positive onset potentials (ΔE of 0.5 V to 0.7 V *vs.* Ag/AgCl) for all catalyst-containing electrodes compared to carbon paper substrate (Figure 4.5a). Nevertheless, the current densities differ depending on the preparation parameters. CuO-60 catalysts (Cu-a, Cu-b, Cu-c and Cu-g) show quite high current densities (from 55 mA cm^{-2} to 75 mA cm^{-2}) compared to the catalysts with less oxidized copper (Cu-d, Cu-e and Cu-f), which exhibit current densities between 17 mA cm^{-2} and 34 mA cm^{-2}. In particular, Cu-c stands out with the highest current density of 75 mA cm^{-2} and the most positive onset potential at -0.5 V *vs.* Ag/AgCl. Based on the higher current densities and lower onset potentials, the CuO-60 catalysts should have higher activity toward CO_2 reduction.

In Figure 4.5b, the chronoamperometric profile of the different catalyst materials are shown in CO_2 saturated 0.5 M $KHCO_3$ electrolyte. CA allow the examination of the electrochemical stability of a catalyst in a certain potential for a longer time. In consistency with the LSV, all materials exhibit considerably high current densities (between ~30 mA cm^{-2} and 50 mA cm^{-2} at -2.0 V *vs.* Ag/AgCl) compared to the carbon paper without catalyst (blank). At low potentials (-1.0 V and -1.3 V *vs.* Ag/AgCl), the CuO-60 catalysts induce higher current densities. Nevertheless, the resulting current of these catalysts at -1.3 V *vs.* Ag/AgCl is not constant during the two minutes of applied potential and it drops with time. The reduction of copper(II) oxide to a less oxidized copper species could be accounted for this current drop. Smaller differences in current densities of all catalysts at more negative potentials as well as the visually observed color change of the catalysts from black to the characteristic reddish brown color of metallic copper further confirm this hypothesis.

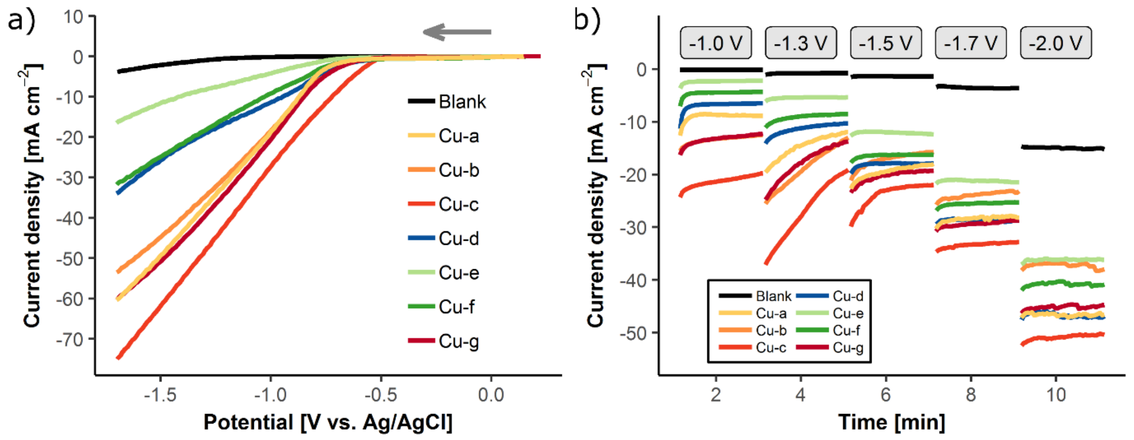

Figure 4.5. a) LSV and b) CA measurements of the synthesized copper catalysts in CO_2 saturated 0.5 M $KHCO_3$, blank = bare carbon paper without catalyst. LSV was measured from Open Circuit Potential (OCP) to -1.7 V *vs.* Ag/AgCl. CA measurements were performed at the different step potentials -1.0 V, -1.3 V, -1.5 V, -1.7 V and -2.0 V *vs.* Ag/AgCl for two minutes each.

Chemical product analysis during two hours of CO_2 reduction were carried out for all catalysts (5 mg cm^{-2}) at -1.7 V *vs.* Ag/AgCl under 10 mL min^{-1} CO_2. Product formation rates and Faraday efficiencies for C1 compared to C2 and C3 products are shown in Figure 4.6. More detailed information on the FE for all materials is presented in Table S4.1 in Chapter 4.5.

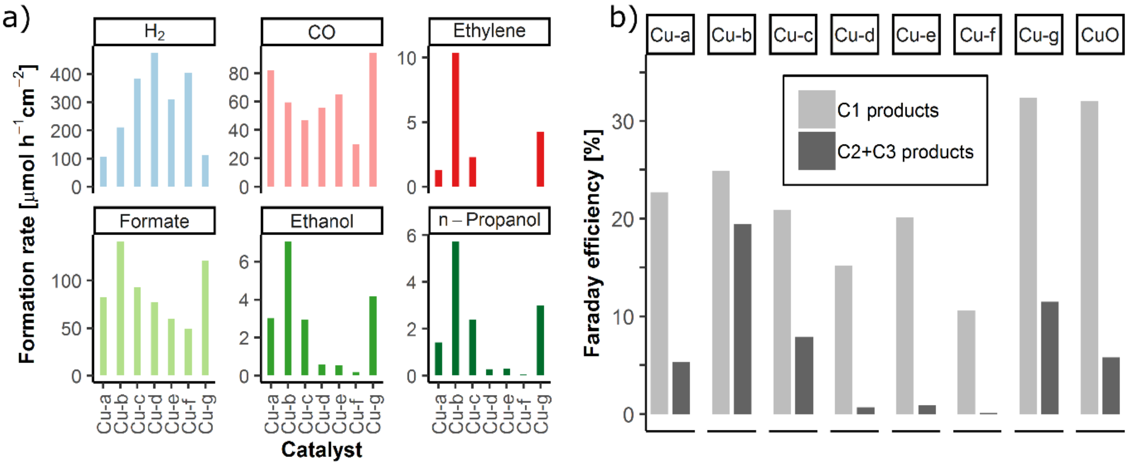

Figure 4.6. a) Formation rates for hydrogen, carbon monoxide, ethylene, formate, ethanol and n-propanol for all synthesized copper catalysts at *E* = -1.7 V *vs.* Ag/AgCl in CO_2 saturated 0.5 M $KHCO_3$. b) Faraday efficiency of the C1 and C2 + C3 products: significantly increasing of C2 and C3 for Cu-b compared to commercial CuO.

Among the products, carbon monoxide, formate, ethanol and n-propanol besides hydrogen were detected for all catalyst materials, whereas ethylene was found exclusively for CuO-60 catalysts (Figure 4.6a).

Catalysts Cu-d, Cu-e and Cu-f, with less oxidized copper species, lead to lower hydrocarbon formation rates, especially for alcohols (< 0.6 µmol h^{-1} cm^{-2}). However, copper(II) oxide-containing catalysts (CuO-60) show a distinctly better performance for C2 and C3 product formation with 1.3 to 10.4 µmol h^{-1} cm^{-2} of ethylene, 2.9 to 7.1 µmol h^{-1} cm^{-2} of ethanol and 1.4 to 5.7 µmol h^{-1} cm^{-2} of n-propanol. Thus, the calcination conditions influence the activity and selectivity of the catalysts towards C2 and C3 products (Figure 4.6b).

Literature reports on Cu and Cu_2O materials[13-14, 30] show that catalysts with less oxidized copper can also generate C2 and C3 products and the current drop for catalysts containing more CuO (CuO-60) during chronoamperometry (Figure 4.5b) suggest that copper(II) oxide is already reduced to metallic copper within the first few minutes of the electrochemical experiment. Thus, the reduction of CuO formed during DES calcination to metallic copper is necessary to create *in situ* a more active copper modification, which promotes the CO_2 reduction to C2 and C3 products. Enhanced C2+ product selectivity by oxide-derived copper catalysts is also found in literature.[31-32] The copper oxide species is preferably reduced at the negative potentials used for CO_2 reduction and metallic copper with a different the morphology is formed during this reduction step resulting in a rough surface with defects.[32]

Low amount of CuO domains in the Cu-d, Cu-e, and Cu-f catalysts may prevent to achieve the same effect of *in situ* activation of Cu compared to the CuO-60 catalysts. However, the carbon-rich domains CuO/CNO of these catalysts have similar morphology and show similar electrochemical activity for C1 products, especially formate, consistently to previous report on CNO rich catalysts.[21]

Comparing the different CuO-60 catalysts in more detail, Cu-b and Cu-g show a better performance compared to Cu-a and Cu-c (Figure 4.6b). Catalyst Cu-b shows by far the highest C2 and C3 selectivity, thus the change of the DES used for the preparation indicates the greatest influence on catalyst activity and selectivity. Interestingly, the calculation of crystallite sizes by XRD revealed that crystallites of Cu-b and Cu-g are larger in *z*-direction compared to Cu-a and Cu-c. This may suggest that a larger *z*-size of the CuO crystallites is beneficial to the C2 and C3 selectivity in the CO_2 reduction. The performance of the catalysts is in accordance to the findings of various authors[14, 33-34] that the performance of copper catalysts, i.e. selectivity and efficiency, differs with the directional crystallite surface areas.

Interestingly, compared to a commercial sample of copper(II) oxide nanoparticles

(Figure 4.6b), the product formation rates of all CuO-60 catalysts prepared by the presented DES calcination in an oxidative atmosphere increase the selectivity to C2 and C3 products. An influence of temperature on the catalyst selectivity could be excluded by sintering of the copper(II) oxide nanoparticles for one hour at 500 °C. This procedure caused even a decrease of the selectivity towards C2 and C3 products from 5.8 % FE for the untreated CuO nanoparticles to 3 % FE for the sintered sample. At the same time, it could be confirmed that the DES calcination method improves the selectivity of the prepared catalysts.

Reproducibility of the experiments could be confirmed exemplarily by using the same batch of the best-performing Cu-b at -1.7 V *vs.* Ag/AgCl for two runs as well as two different catalyst batches of Cu-a at the same conditions (Table 4.5). Apart from hydrogen production, which exhibits large variations and is mainly responsible for the increase in current density ($\Delta J = 18$ mA cm^{-2} for two runs of the same batch of Cu-b and $\Delta J = 26$ mA cm^{-2} for two different Cu-a batches), the product formation rates of C2 and C3 products (ethylene, ethanol, n-propanol) show low fluctuations. As for C1 products CO ($\Delta = 13$ µmol h^{-1} cm^{-2} and $\Delta = 44.1$ µmol h^{-1} cm^{-2}, respectively) and formate ($\Delta = 16.6$ µmol h^{-1} cm^{-2} and $\Delta = 13.9$ µmol h^{-1} cm^{-2}, respectively), these fluctuations are higher, although it remain within the limits of measurement inaccuracies. The total FE differs only by 5 % for two runs of the same catalyst Cu-b and by 0.9 % for two different Cu-a batches, showing good reproducibility for the experimental setup and the catalyst preparation.

Table 4.5. Product formation rates, Faraday efficiency and current densities for two experiments using the same batch of copper catalyst Cu-b at *E* = -1.7 V *vs.* Ag/AgCl in CO_2 saturated 0.5 M $KHCO_3$ and for two different batches of copper catalyst Cu-a.

		Formation rates [µmol h^{-1} cm^{-2}]						**total FE**	***J***
		H_2	CO	$HCOO^-$	C_2H_4	C_2H_5OH	C_3H_7OH	**[%]**	**[mA cm^{-2}]**
Cu-b	1st run	210.2	59.4	141.1	10.4	7.1	5.7	70.5	-43
	2nd run	373.9	72.4	124.5	13.4	7.5	5.1	65.5	-61
Cu-a	1st batch	252.5	75.3	80.3	3.3	2.5	1.3	54.9	-68
	2nd batch	176.5	119.4	94.2	3.4	3.5	1.8	54.1	-42

Formation rates for C1, C2 and C3 products described in literature are compared to those observed in this work for Cu-b in Table 4.6. Cu-b shows remarkably high formation rates for C2 and C3 products at a rather positive potential compared to literature values. The catalyst shows also comparable rates for C1 products (CO and formate).

Table 4.6. Comparison of the product formation rates from electrochemical CO_2 reduction performed on different electrode materials. *E* is shown *vs.* RHE: * converted from -1.7 V *vs.* Ag/AgCl, ** 2 electrode setup, *** converted from -2.0 V *vs.* SCE

Electrode	**E *vs.* RHE [V]**	**Formation rates [μmol h^{-1} cm^{-2}]**					**Ref.**
		CO	**C_2H_4**	**$HCOO^-$**	**C_2H_5OH**	**C_3H_7OH**	
Fe-N-C	-0.80	126	-	-	-	-	[35]
Cu-organic porous materials	-0.90	-	-	-	0.05	-	[36]
Cu-mesocrystals	-0.99	6	17	-	-	-	[30]
Cu-nanocrystals	-1.05	10	12	-	10	2	[37]
Cu-b	-1.08*	59.4	10.4	147.6	7.4	6.0	this work
doped nanodiamond	-1.10	-	-	-	1.96	-	[38]
Ru-based catalyst	-1.25**	-	-	-	0.045	0.03	[39]
Sn	-1.76***	-	-	228	-	-	[40]

4.3 Conclusion

The reported protocol demonstrates a novel and facile preparation method for carbon-containing copper oxide electrocatalysts based on deep eutectic solvent calcination. Their activity towards electrochemical CO_2 reduction in aqueous media was investigated in detail. The catalyst properties were affected by different preparation parameters such as choice of DES and copper precursor or the treatment time in air during calcination.

Copper precursors influence the morphology of the catalyst particles and the DES affects the crystallite size of copper in *z*-direction. Time of oxidative treatment influences the oxidation state of copper and the amount of supporting material CNO formed from the DES. Treatment time of 60 minutes in air provides exclusively copper(II) oxide containing catalysts with less support, while a shorter time causes less oxidized forms of copper (Cu_2O and Cu^0), besides CuO and distinctly higher amounts of support.

Electrochemical investigations of the catalysts revealed that calcination at 500 °C in air for 60 minutes leads to higher activity and C2/ C3 product selectivity compared to shorter treatment times. However, copper(II) oxide is reduced to metallic copper at an early stage of the CO_2 reduction experiment, which has an intrinsic influence on the catalytic performance of the *in situ* formed copper species.

The catalyst prepared with the DES UGa, copper nanoparticles as precursor and an oxidative treatment for 60 minutes at 500 °C showed the highest activity and enhanced the selectivity towards C2 and C3 products significantly compared to commercial CuO. This catalyst produced a mixture of 141.1 µmol h^{-1} cm^{-2} formate, 10.4 µmol h^{-1} cm^{-2} ethylene, 7.1 µmol h^{-1} cm^{-2} ethanol, 5.7 µmol h^{-1} cm^{-2} n-propanol and 59.4 µmol h^{-1} cm^{-2} CO at -1.7 V *vs.* Ag/AgCl at the investigated optimum process parameters, 5 mg cm^{-2} catalyst loading, 10 mL min^{-1} CO_2 gas flow in 0.5 M $KHCO_3$. Reproducibility of the experiments could be confirmed using the best-performing catalyst, since the experiments differ only in a total Faraday efficiency of 5 %.

Finally, we have presented a promising and facile method for preparation of copper electrocatalysts, which show a remarkable performance for C2 and C3 products from electrochemical CO_2 reduction compared to the literature.

4.4 Experimental Section

4.4.1 Chemicals

Commercial reagents and used chemicals were purchased from Sigma Aldrich, Acros, TCI, VWR, Carl Roth, Merck or Alfa Aesar and used without further purification.

4.4.2 Catalyst preparation

Catalysts were prepared as described previously.[20] In a round-bottom flask, a total amount of 45 mmol of the different DES based on urea - ᴅ-glucose (UG) in a molar ratio of 2:9 or urea - ᴅ-galactose (UGa) in a molar ratio of 1:7 were heated to 110 °C until a clear, homogeneous liquid was formed. A defined amount of copper precursor (500 mg CuNP or 650 mg CuO) was homogeneously mixed to the DES and the mixture was heated to 290 °C under air or inert atmosphere for 90 minutes (pre-treatment). Afterwards, in the calcination step, the pre-pyrolyzed material was further heated in a muffle furnace to a final temperature between 450 °C and 550 °C under air for 10 min, 15 min or 60 min, until a fine porous powder resulted. Table 4.7 shows the detailed synthesis parameters for all catalysts shown in this work.

Table 4.7. Overview of the different preparation parameter. The following abbreviations correspond to Glc - D-glucose, Gal - D-galactose, U - urea, CuNP - copper nanopowder, RT - room temperature. Catalysts Cu-e and Cu-f were prepared in two steps, pyrolysis under an inert atmosphere and oxidative treatment for 10 minutes. Elemental composition is shown of the different catalysts prepared after calcination. Catalysts Cu-d, Cu-e and Cu-f show two different types of particles - Cu rich and Cu poor ones.

	Precursor		**Pre-treatment**			**Calcination**			**Elemental composition**			
	DES	Metal	*t* [h]	*T* [°C]	Atm.	*t* [min]	*T* [°C]	Atm.	Cu [wt%]	O [wt%]	C [wt%]	N [wt%]
Cu-a	UG	CuNP	1.5	290	air	60	500	air	80.3	13.1	4.4	2.2
Cu-b	UGa	CuNP	1.5	290	air	60	500	air	72.8	21.6	3.2	2.5
Cu-c	UG	CuO	1.5	290	air	60	500	air	79.3	14.9	3.5	2.2
Cu-d	UG	CuNP	1.5	290	air	15	500	air	72.9	14.6	9.5	3.2
									29.5	7.0	48.0	15.4
Cu-e	UG	CuNP	1.5	290	N_2	from RT	to 450	N_2	62.6	14.3	17.0	6.2
						10	500	air	39.2	4.9	43.2	12.7
Cu-f	UG	CuNP	1.5	290	N_2	from RT	to 500	N_2	68.0	22.8	5.7	3.6
						10	550	air	49.0	16.8	25.9	8.3
Cu-g	UG	CuNP	1.5	290	N_2	60	500	air	77.1	17.7	2.2	3.0

4.4.3 Catalyst characterization

Scanning electron microscopy (SEM)

Scanning electron microscopy was performed to determine the morphologies of the catalysts by secondary electron (SE) detector and the composition of the materials by the energy-disperive X-ray (EDX) detector. The samples were fixed on a carbon tape and investigated using a field emission electron microscope (Leo 1530VP, Zeiss) at 15 kV for imaging and EDX.

Powder diffractometry (XRD)

Materials were assessed by powder X-ray diffractometry in Bragg-Brentano geometry (XRD, Miniflex, Rigaku, Tokyo, Japan, with silicon strip detector D/teX Ultra). Copper K_α radiation with a wavelength λ of 1.54 Å was used and the samples rotated during measurements. Intensities were recorded in steps of $2\theta = 0.02°$; Soller slits with angular apertures of 5° were used. The maximum recorded scattering angle was $2\theta = 100°$. Samples were placed on monocrystalline silicon substrates, which showed no Bragg reflexes within the considered range of 2θ. Their continuous background scattering intensities were recorded separately and subtracted. Our results were compared with data in the Crystallography Open Database (COD) by the Rigaku PDXL software (integrated X-ray powder diffraction software).

A combination with the Scherrer equation (5) allows the calculation of the crystallite size of copper oxide:

$$D_{hkl} = \frac{\lambda \cdot \kappa}{FWHM \cdot \cos(\theta)} \quad (5)$$

Thereby, D_{hkl} is the crystallite size in *h*, *k* and *l* direction in reciprocal scale, κ is the shape constant chosen for that system (0.94) and FWHM the full width at half-maximum of the diffraction peak. A detailed calculation of the copper oxide crystallite sizes in real space is shown in Figure S4.4 in Chapter 4.5.

4.4.4 Electrochemical measurements

Electrode preparation

A defined amount (5 mg cm^{-2}) of the as-prepared catalysts was dispersed in 400 µL of a mixture of distilled water and isopropanol (1:1) containing 10.8 µL of 5 wt% Nafion® solution as binder. The mixture was sonicated for 30 minutes, drop coated on the substrates and dried at room temperature overnight. The substrates consisted on 1 cm^2 Toray™ Carbon Paper TP-060 (Quintech) for cyclic voltammetry (CV) and chronoamperometry (CA) and gas diffusion layers (GDL, Freudenberg) for product analysis experiments.

Electrochemical cells

Catalyst screening was carried out in two steps: firstly, the current density of all materials were evaluated by CV and CA in 20 mL of CO_2 or Argon saturated 0.5 M $KHCO_3$ electrolyte in a 1-compartment three electrode cell. An Ag/AgCl in 3 M KCl electrode (Metrohm) was used as reference (RE) and a TiO_2/IrO_2 mesh (Metakem, 6x3.5x1x1 mm, 12 g m^{-2} of Ir) as counter electrode (CE). All experiments were performed at room temperature (23 ºC).

The second step was performed on drop-coated gas diffusion electrodes (GDE) in a 3-compartment cell (Gaskatel) comprising an anode compartment (30 mL of 0.5 M $KHCO_3$), a cathode compartment (15 mL of CO_2 saturated 0.5 M KHCO3) and a gas chamber with a CO_2 flow of 10 mL min^{-1}. A cation exchange membrane (Fumatech, FUMASEP® FKL-PK-130) divided the anode and cathode chamber. Gas bags (0.6 L, Sigma Aldrich) and liquid samples were collected every 30 minutes.

Metrohm Echo Chemie Autolab PGSTAT128N or PGSTAT204 potentiostates controlled by NOVA software were used for all electrochemical experiments.

4.4.5 Product analysis

Gas chromatography with thermal conductivity detector (GC-TCD)

The gaseous samples were detected using gas chromatography (GC, Shimadzu 2010) equipped with three columns (two Poraplot Q (25 m x 0.53 mm), thickness: 20 µm, one Cp-Molsieve (5A 50 m x 0.53 mm), ID: 50 µm) and a 25 µL sample loop. The temperature program used was 60 °C for 6.3 min followed by a heating rate of 15 ° min^{-1} to 150 °C and a duration time of 2 minutes. The thermal conductivity detector (TCD) operates under a helium flow of 10 mL min^{-1} at 250 °C and the product determination was performed using calibration curves for each gaseous product.

Gas chromatography with flame ionization detector (GC-FID)

The volatile liquid products were detected using a gas chromatography (GC, Shimadzu 2010) equipped with a Zebron ZB-WAX column (Phenomenex). The samples were agitated at 90 °C for 15 min and 2000 µL of the vaporized samples were injected at 250 °C to the equipment. The temperature program used was 35 °C for 7 min followed by a heating rate of 20 ° min^{-1} to 190 °C and a duration time of 3 minutes with a helium column flow of 1 mL min^{-1}. Quantification was performed using calibration curves.

High pressure liquid chromatography (HPLC)

The acidic product determination was performed using high pressure liquid chromatography (HPLC, Shimadzu LC20A) with a Rezex ROA-Organic Acid H+ (8 %) column (Phenomenex). For formate determination, an isocratic separation with 0.005 N H_2SO_4 was used with a flow of 0.5 mL min^{-1}. Quantification was done using calibration curves. For that, a sample of 150 µL was taken during the process and 10 µL were injected at the equipment.

NMR spectroscopy

NMR spectroscopy was carried out in a JEOL JNM ECA 400MHz spectrometer. For the experiments the following parameter were used: 25 °C, 90° pulse, NS of 128, relaxation time of 18 s and water suppression of 40 DB. The internal standard 3-(trimethylsilyl) propanoic acid sodium salt-D4 dissolved in deuterium oxide was used for product quantification.

4.5 Supporting information

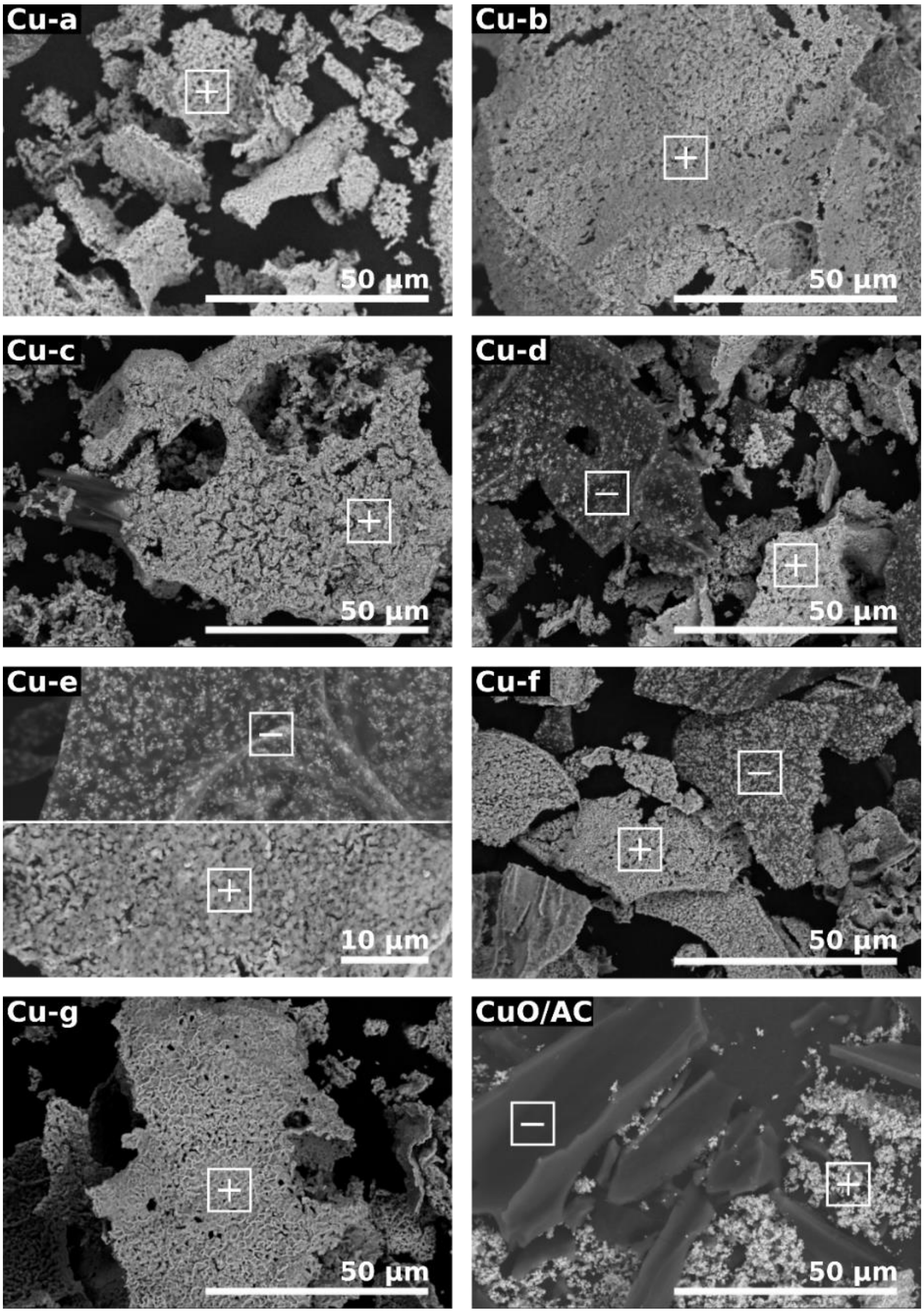

Figure S4.1. SEM images of synthesized copper materials comprising light (+) and dark (-) particle types. CuO/AC shows CuO mixed with activated carbon (commercial products).

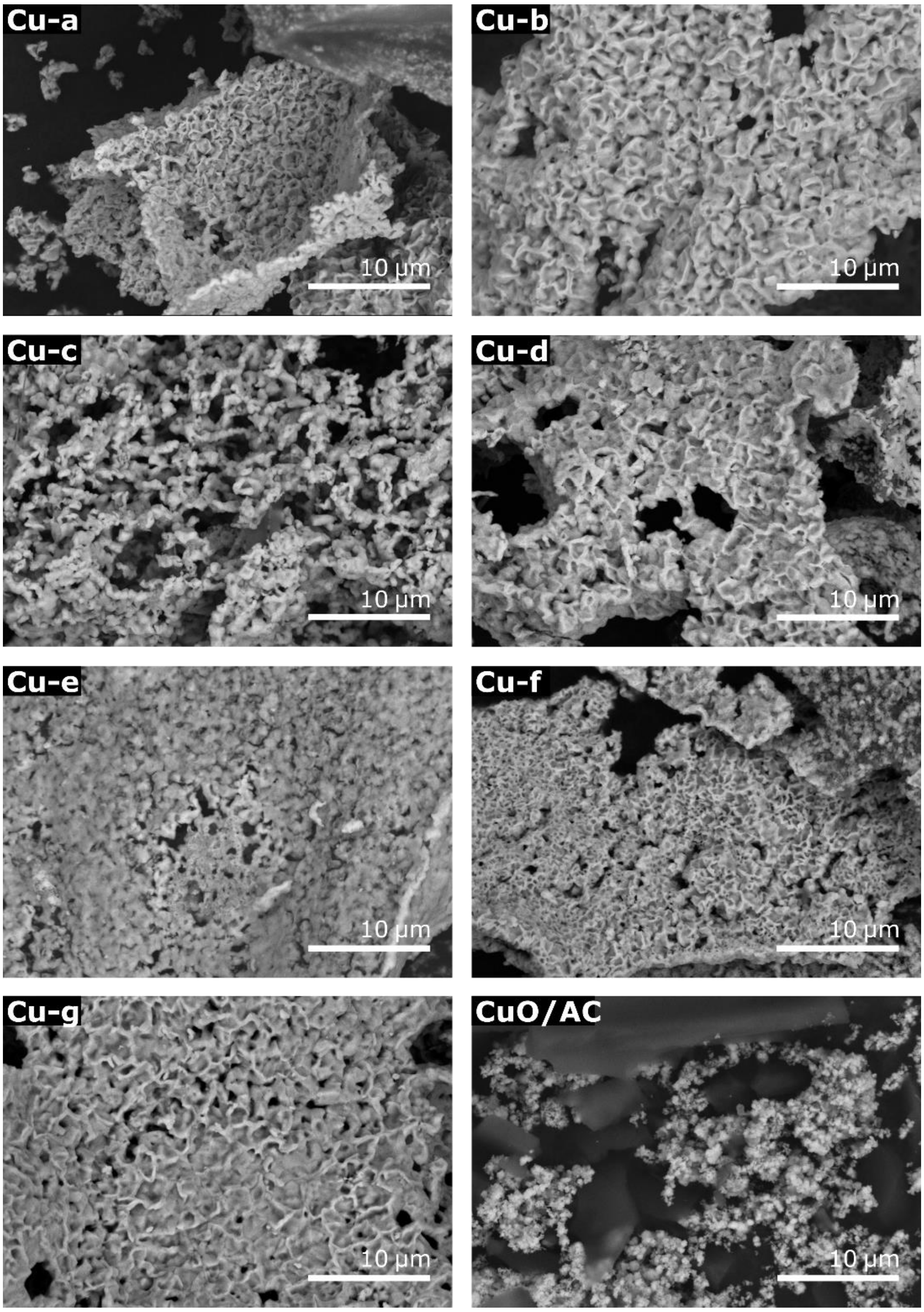

Figure S4.2. SEM images of all synthesized copper materials and CuO/AC.

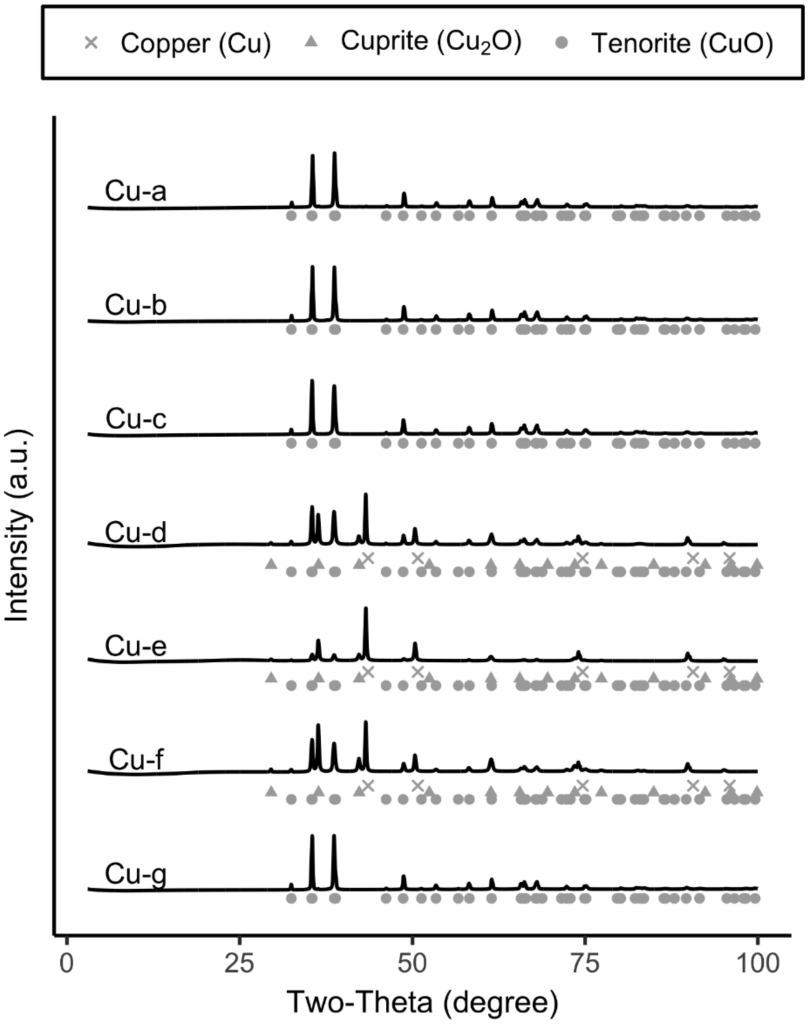

Figure S4.3. X-ray powder diffractograms of all copper catalysts show different copper oxidation states (0, +I and +II). The measurements are normalized to 1.

Calculation of the crystallite size

The Scherrer equation relates the crystallite size to the width at half maximum of the peaks in a diffractogram. Since each peak represents a certain symmetry plane of the crystal, the shape of the crystallite can be estimated by the calculation of the length in the different directions. Scherrer's equation yields crystallite dimension in the reciprocal space. These dimensions can be converted into the size in the real space. Directions $\vec{h}$, $\vec{k}$ and $\vec{l}$ in the reciprocal space are orthogonal to the according planes, spanned by unity cell axes $\vec{a}, \vec{b}, \vec{c}$:

$\vec{h} \sim \vec{b} \times \vec{c}$

$\vec{k} \sim \vec{a} \times \vec{c}$

$\vec{l} \sim \vec{a} \times \vec{b}$

Tenorite (CuO) shows a monoclinic crystal system with angles $\alpha = \gamma = 90°$ and $\beta = 99.5°$.[1] Our measurements match well with the tenorite structure of the crystallography open database (COD) ID 9016326 (space group C1c1 and unit cell with a = 4.6927, b = 3.4283 and c = 5.1370). Therefore, the mentioned vectors $\vec{h}$ and $\vec{l}$ are not parallel to the *x*- and *z*-axis, respectively (Figure S4.4).

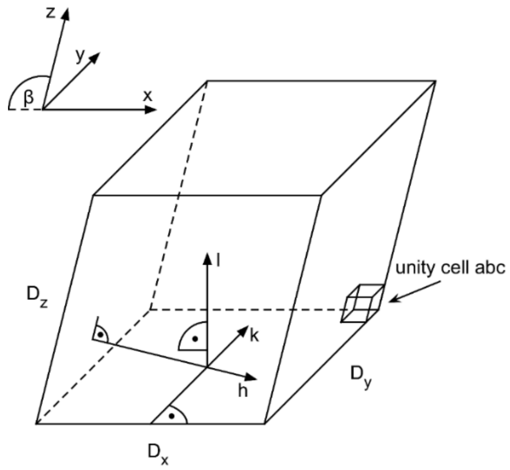

Figure S4.4. Scheme of the monoclinic CuO crystallite. Axes *h*, *k* and *l* are orthogonal to the planes, spanned by unity cell axes *a*, *b* and *c*.

The according values D_h and D_l obtained by Scherrer's equation need to be corrected by the angle β, while D_k corresponds directly to the size in the *y*-direction:

$\vec{h} \nparallel \vec{x} \Rightarrow D_x = D_h \cdot sin(\beta)$

$\vec{k} \parallel \vec{y} \Rightarrow D_y = D_k$

$\vec{l} \nparallel \vec{z} \Rightarrow D_z = \frac{D_l}{sin(\beta)}$

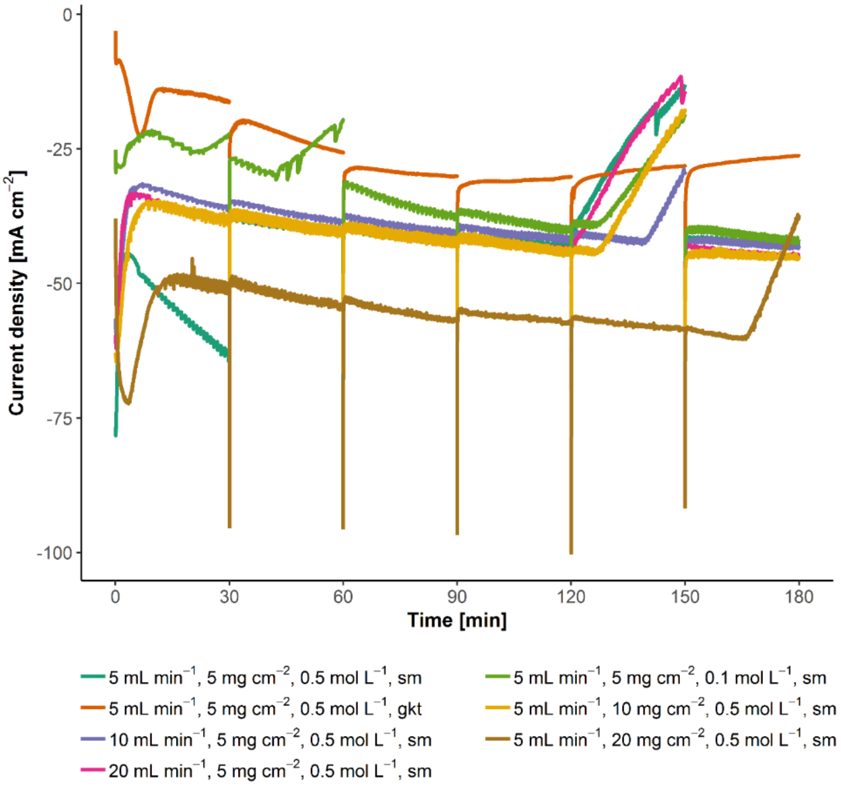

Figure S4.5. Overview of the current densities at -1.7 V *vs.* Ag/AgCl. The 0.1 M concentrated electrolyte degrades after ~ 40 min, while the 0.5 M $KHCO_3$ is stable for about 120 min.

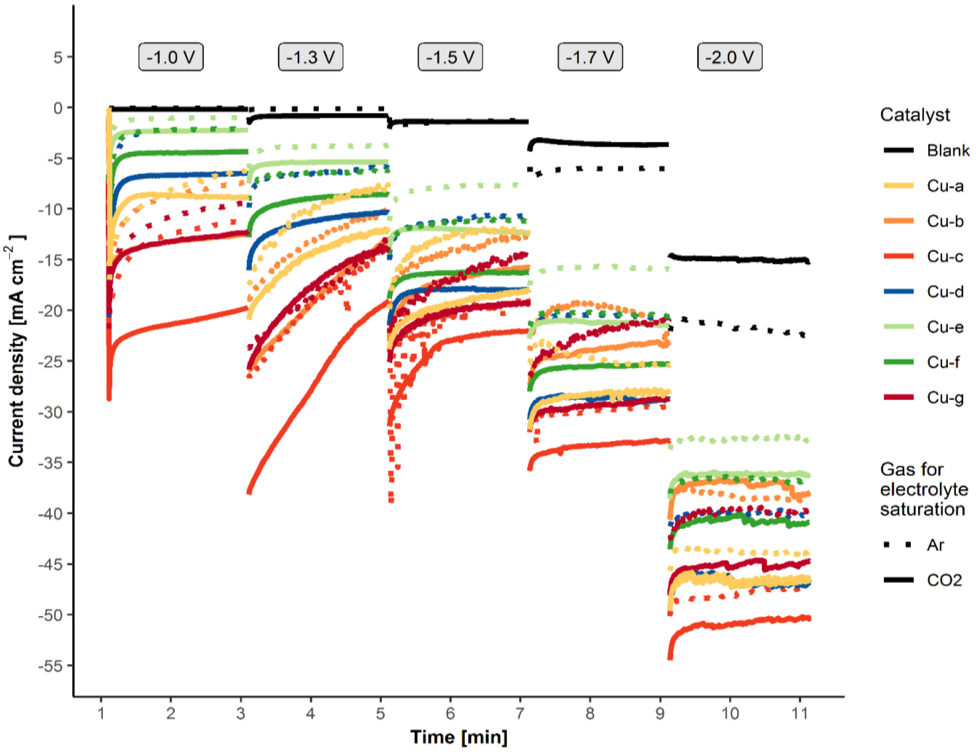

Figure S4.6. Chronoamperograms for synthesized copper catalysts in Argon and CO_2 saturated 0.5 M $KHCO_3$. Potentials shown vs. Ag/AgCl.

Table S4.1. Faraday efficiencies of all synthesized copper materials at E = -1.7 V *vs.* Ag/AgCl in CO_2 saturated 0.5 M $KHCO_3$. More detailed information of Figure 4.6b is shown in this table.

Catalyst	**FE [%]**							**J [mA cm^{-2}]**
	total	**H_2**	**CO**	**ethylene**	**formate**	**ethanol**	**n-propanol**	
Cu-a	42.7	14.7	11.3	1.1	11.4	2.5	1.7	-38.96
Cu-b	70.5	26.1	7.4	7.7	17.5	5.3	6.4	-43.11
Cu-c	86.1	57.3	7.0	2.1	13.9	2.6	3.2	-35.79
Cu-d	70.3	54.4	6.4	—	8.8	0.4	0.3	-46.91
Cu-e	71.0	50.0	10.5	—	9.6	0.5	0.4	-33.25
Cu-f	65.3	54.5	4.0	—	6.6	0.1	—	-39.73
Cu-g	60.8	16.8	14.2	3.8	18.2	3.7	4.0	-35.70

4.6 References

[1] A. Indermühle, E. Monnin, B. Stauffer, T. F. Stocker, M. Wahlen, *Geophysical Research Letters* **2000**, *27*, 735-738.

[2] S. M. Benson, F. M. Orr, *MRS Bulletin* **2011**, *33*, 303-305.

[3] F. A. Rahman, M. M. A. Aziz, R. Saidur, W. A. W. A. Bakar, M. R. Hainin, R. Putrajaya, N. A. Hassan, *Renewable and Sustainable Energy Reviews* **2017**, *71*, 112-126.

[4] D. Y. C. Leung, G. Caramanna, M. M. Maroto-Valer, *Renewable and Sustainable Energy Reviews* **2014**, *39*, 426-443.

[5] A. A. Olajire, *Energy* **2010**, *35*, 2610-2628.

[6] H.-R. M. Jhong, S. Ma, P. J. A. Kenis, *Current Opinion in Chemical Engineering* **2013**, *2*, 191-199.

[7] D. T. Whipple, P. J. A. Kenis, *The Journal of Physical Chemistry Letters* **2010**, *1*, 3451-3458.

[8] B. Kumar, J. P. Brian, V. Atla, S. Kumari, K. A. Bertram, R. T. White, J. M. Spurgeon, *Catalysis Today* **2016**, *270*, 19-30.

[9] M. Azuma, K. Hashimoto, M. Hiramoto, M. Watanabe, T. Sakata, *Journal of Electroanalytical Chemistry and Interfacial Electrochemistry* **1989**, *260*, 441-445.

[10] Y. Hori, A. Murata, R. Takahashi, S. Suzuki, *Journal of the Chemical Society, Chemical Communications* **1988**, 17-19.

[11] M. B. Gawande, A. Goswami, F.-X. Felpin, T. Asefa, X. Huang, R. Silva, X. Zou, R. Zboril, R. S. Varma, *Chemical Reviews* **2016**, *116*, 3722-3811.

[12] K. P. Kuhl, E. R. Cave, D. N. Abram, T. F. Jaramillo, *Energy & Environmental Science* **2012**, *5*, 7050-7059.

[13] F. S. Roberts, K. P. Kuhl, A. Nilsson, *Angewandte Chemie International Edition* **2015**, *54*, 5179-5182.

[14] D. Ren, Y. Deng, A. D. Handoko, C. S. Chen, S. Malkhandi, B. S. Yeo, *ACS Catalysis* **2015**, *5*, 2814-2821.

[15] Y. Hori, in *Modern Aspects of Electrochemistry* (Eds.: C. G. Vayenas, R. E. White, M. E. Gamboa-Aldeco), Springer New York, New York, NY, **2008**, pp. 89-189.

[16] W. Zhang, Y. Hu, L. Ma, G. Zhu, Y. Wang, X. Xue, R. Chen, S. Yang, Z. Jin, *Advanced Science* **2018**, *5*, 1700275.

[17] A. Loiudice, P. Lobaccaro, E. A. Kamali, T. Thao, B. H. Huang, J. W. Ager, R.

Buonsanti, *Angewandte Chemie International Edition* **2016**, *55*, 5789-5792.

[18] D. Kim, C. S. Kley, Y. Li, P. Yang, *Proceedings of the National Academy of Sciences* **2017**, *114*, 10560-10565.

[19] C. W. Li, M. W. Kanan, *Journal of the American Chemical Society* **2012**, *134*, 7231-7234.

[20] M. Iwanow, J. Finkelmeyer, A. Söldner, M. Kaiser, T. Gärtner, V. Sieber, B. König, *Chemistry – A European Journal* **2017**, *23*, 12467-12470.

[21] M. Iwanow, L. Vieira, I. Rud, J. Pöessnecker, M. Kaiser, D. Van Opdenbosch, C. Zollfrank, T. Gärtner, B. König, V. Sieber, **2019**, *Pyrolysis of deep eutectic solvents for the preparation of supported copper electrocatalysts*, in preparation.

[22] F. T. L. Muniz, M. A. R. Miranda, C. Morilla dos Santos, J. M. Sasaki, *Acta Crystallographica Section A* **2016**, *72*, 385-390.

[23] D. V. Wagle, H. Zhao, G. A. Baker, *Accounts of Chemical Research* **2014**, *47*, 2299-2308.

[24] M. Gattrell, N. Gupta, A. Co, *Journal of Electroanalytical Chemistry* **2006**, *594*, 1-19.

[25] Y. Hori, R. Takahashi, Y. Yoshinami, A. Murata, *The Journal of Physical Chemistry B* **1997**, *101*, 7075-7081.

[26] J. A. Wojtowicz, *Journal of the Swimming Pool and Spa Industry* **2001**, *4.1*, 54-59.

[27] A. S. Varela, M. Kroschel, T. Reier, P. Strasser, *Catalysis Today* **2016**, *260*, 8-13.

[28] O. Scialdone, A. Galia, G. L. Nero, F. Proietto, S. Sabatino, B. Schiavo, *Electrochimica Acta* **2016**, *199*, 332-341.

[29] Q. Lu, F. Jiao, *Nano Energy* **2016**, *29*, 439-456.

[30] C. S. Chen, A. D. Handoko, J. H. Wan, L. Ma, D. Ren, B. S. Yeo, *Catalysis Science & Technology* **2015**, *5*, 161-168.

[31] Y. Zheng, A. Vasileff, X. Zhou, Y. Jiao, M. Jaroniec, S.-Z. Qiao, *Journal of the American Chemical Society* **2019**.

[32] J. E. Pander III, D. Ren, Y. Huang, N. W. X. Loo, S. H. L. Hong, B. S. Yeo, *ChemElectroChem* **2018**, *5*, 219-237.

[33] D. Ren, Y. Deng, A. D. Handoko, C. S. Chen, S. Malkhandi, B. S. Yeo, *ACS Catalysis* **2015**, *5*, 2814-2821.

[34] R. Kas, R. Kortlever, A. Milbrat, M. T. M. Koper, G. Mul, J. Baltrusaitis, *Physical Chemistry Chemical Physics* **2014**, *16*, 12194-12201.

[35] T. N. Huan, N. Ranjbar, G. Rousse, M. Sougrati, A. Zitolo, V. Mougel, F. Jaouen, M. Fontecave, *ACS Catalysis* **2017**, *7*, 1520-1525.

[36] J. Albo, D. Vallejo, G. Beobide, O. Castillo, P. Castaño, A. Irabien, *ChemSusChem* **2017**, *10*, 1100-1109.

[37] D. Ren, N. T. Wong, A. D. Handoko, Y. Huang, B. S. Yeo, *The Journal of Physical Chemistry Letters* **2016**, *7*, 20-24.

[38] Y. Liu, Y. Zhang, K. Cheng, X. Quan, X. Fan, Y. Su, S. Chen, H. Zhao, Y. Zhang, H. Yu, M. R. Hoffmann, *Angewandte Chemie International Edition* **2017**, *56*, 15607-15611.

[39] D. Sebastián, A. Palella, V. Baglio, L. Spadaro, S. Siracusano, P. Negro, F. Niccoli, A. S. Aricò, *Electrochimica Acta* **2017**, *241*, 28-40.

[40] J. Qiao, Y. Liu, F. Hong, J. Zhang, *Chemical Society Reviews* **2014**, *43*, 631-675.

[41] R. D. C. Team, R Foundation for Statistical Computing, Vienna, Austria, **2010**.

SUMMARY

5 Summary

This thesis presents the preparation of novel supported metal catalysts based on deep eutectic solvents (DES). The catalysts were loaded with palladium for the development of the method and with copper for the application in electrochemical CO_2 reduction.

Chapter 1

The preparation of activated carbon materials is discussed using selected examples of precursor materials, of available production and modification methods and possible characterization techniques. The preparation methods for activated carbon materials were evaluated with respect to its use as catalyst support and important parameters for metal loading were identified. The considered carbon sources include coal, wood, agricultural wastes or biomass as well as ionic liquids, deep eutectic solvents or precursor solutions. The preparation of the activated carbon usually involves pre-treatment steps followed by physical or chemical activation and application-dependent modification. In addition, highly porous materials can also be produced by salt templating or ultrasonic spray pyrolysis as well as by microwave irradiation. The resulting activated carbon materials are characterized by a variety of techniques such as SEM, FTIR, nitrogen adsorption, Boehm titrations, adsorption of phenol, methylene blue and iodine, TPD, CHNS/O elemental analysis, EDX, XPS, XRD and TGA.

Chapter 2

The development of the DES method was carried out by loading with palladium in order to compare the resulting catalyst activities easily with commercial catalysts in test reactions.
Deep eutectic solvents (DES) dissolve metal salts or oxides and were used as solvent and carbon source for the preparation of supported palladium catalysts. After dissolving of the palladium salt in the DES, the pyrolysis of the mixture under nitrogen atmosphere yields catalytically active palladium on supporting material composed of carbon, nitrogen and oxygen (CNO) by a simple single step preparation method without further activation. The catalysts were characterized by SEM and XPS microscopy, XRD, BET and CHNS/O elemental analysis. The amount of functional groups on the surface of the supporting material was determined by Boehm titrations. Moreover, the activity of the prepared catalysts was evaluated in the hydrogenation of linear alkenes and compared with a commercial Pd/C catalyst.

Chapter 3

Electrochemical CO_2 reduction on Cu-based catalysts can form hydrocarbons, alcohols and formate, besides carbon monoxide and hydrogen. This chapter focus on the preparation of novel supported copper catalysts for the electrochemical CO_2 reduction to formate. Material characterization by SEM, XRD, CHNS/O elemental analysis, CO_2 adsorption measurements and Boehm titrations showed that these catalysts consist mostly of metallic copper supported on a carbon material rich in oxygen and nitrogen functional groups (Cu/CNO). The electrochemical activity of the prepared materials was investigated by cyclic voltammetry and chronoamperometry in CO_2-saturated $KHCO_3$ solutions. Current densities and onset potentials were correlated with material preparation parameters such as the nature of the different DES, copper precursor and pyrolysis temperature. The effect of the copper loading in the carbon support and catalyst loading on the electrode were correlated with the current densities. Copper catalysts in carbon support materials rich in oxygen and nitrogen showed a selective formate production in liquid phase at -1.5 V *vs.* Ag/AgCl with formation rates up to 85.5 µmol h^{-1} cm^{-2}.

Chapter 4

Copper oxides (CuO and Cu_2O) are promising candidates that promote the formation of hydrocarbons in electrochemical CO_2 reduction. A novel preparation method for carbon-doped copper oxide catalysts (CuO/CNO) based on an oxidative thermal treatment of copper-containing deep eutectic solvents (DES) is reported in this chapter. SEM micrographs show different particle morphologies, while XRD exhibits different oxidation states of copper based on the preparation conditions. A longer treatment time at 500 °C (60 min) in an O_2-containing atmosphere provides exclusively CuO catalysts, whereas shorter times (10 min or 15 min) lead to less oxidized forms of copper (Cu_2O and Cu^0), besides CuO. Linear sweep voltammetry and chronoamperometry showed high current density in CO_2-saturated electrolytes. Chemical analysis of the products revealed an enhanced selectivity towards C2 and C3 products for the catalyst prepared from the DES urea - ᴅ-galactose with copper nanoparticles and calcination for 60 minutes in air. At -1.7 V *vs.* Ag/AgCl, the product concentration is considerably higher compared to commercial CuO, with formation rates of 7.4, 6.0 and 10.4 µmol h^{-1} cm^{-2} for ethanol, n-propanol and ethylene, respectively.

ZUSAMMENFASSUNG

6 Zusammenfassung

Diese Arbeit befasst sich mit der Herstellung von neuen geträgerten Metallkatalysatoren basierend auf tiefeutektischen Lösungsmitteln (deep eutectic solvents, DES). Die Katalysatoren wurden zur Entwicklung des Verfahrens mit Palladium beladen. Für die Anwendung in der elektrochemischen CO_2-Reduktion wurden geträgerte Kupferkatalysatoren hergestellt.

Kapitel 1

In diesem Kapitel wird die Herstellung von Aktivkohle anhand ausgewählter Beispiele von Ausgangsmaterialien, verfügbaren Herstellungs- und Modifizierungsmethoden und möglichen Charakterisierungstechniken diskutiert. Als mögliche Kohlenstoffquellen wurden Kohle, Holz, landwirtschaftliche Abfälle oder Biomasse, sowie ionische Flüssigkeiten, tief eutektische Lösungsmittel oder spezielle Lösungen betrachtet. Aktivkohle wird üblicherweise in mehreren Schritten hergestellt: Vorbehandlung, physikalische oder chemische Aktivierung mit anschließender Modifikation der Materialien. Darüber hinaus können hochporöse Materialien auch durch die *Salt Templating* Methode, die *Ultrasonic Spray* Pyrolyse oder mittels Mikrowellenbestrahlung hergestellt werden. Die resultierenden Aktivkohlenmaterialien können anhand vieler Methoden charakterisiert werden, wie REM, FTIR, Stickstoffadsorption, Boehm Titrationen, Adsorption von Phenol, Methylenblau und Iod, TPD, CHNS/O Elementaranalyse, EDX, XPS, XRD und TGA.

Kapitel 2

Tiefeutektische Lösungsmittel (DES) lösen Metallsalze oder -oxide und werden dadurch gleichzeitig als Lösungsmittel und Kohlenstoffquelle für die Herstellung von geträgerten Palladium-Katalysatoren (Pd/CNO) verwendet. Die Pyrolyse der DES-Palladiumsalz Mischung unter Stickstoff liefert den aktiven Pd/CNO in einem einfachen einstufigen Herstellungsverfahren ohne weitere Aktivierung. Das Trägermaterial besteht dabei aus Kohlenstoff, Stickstoff und Sauerstoff (CNO). Durch Beladung der Katalysatoren mit Palladium konnte während der DES-Methodenentwicklung die resultierende Katalysatoraktivität einfach mit handelsüblichen Katalysatoren (Pd/C) in Testreaktionen (Hydrierung von Alkenen) verglichen und so der Einfluss der verschiedenen Herstellungsparameter festgestellt werden.

Kapitel 3

Die elektrochemische CO_2-Reduktion an Kupfer-Katalysatoren liefert neben Kohlenmonoxid und Wasserstoff auch Kohlenwasserstoffe, Alkohole und Formiat. Dieses Kapitel befasst sich mit der Herstellung von neuen geträgerten Kupfer-Katalysatoren, basierend auf der Pyrolyse von DES, für die elektrochemische CO_2-Reduktion zu Formiat. Die Charakterisierung mit Hilfe von REM, XRD, CHNS/O Elementaranalyse, CO_2-Adsorptionsmessungen und Boehm Titrationen ergab, dass die Katalysatoren hauptsächlich aus metallischem Kupfer und einem kohlenstoffhaltigem Trägermaterial mit vielen sauerstoff- und stickstoffhaltigen funktionellen Gruppen bestehen. Die elektrochemische Aktivität der hergestellten Materialien wurde mittels Cyclovoltammetrie und Chronoamperometrie in CO_2-gesättigten Elektrolyten ($KHCO_3$) untersucht. Die Stromdichten und Onset-Potentiale wurden mit den Herstellungsparametern (verschiedene DES, Kupfervorstufen und Pyrolysetemperaturen) korreliert. Der Einfluss der Kupferbeladung im Katalysator und der Katalysatorbeladung auf der Elektrode wurden anhand der resultierenden Stromdichten untersucht. Die hergestellten Kupfer-Katalysatoren zeigten eine höhere Selektivität für die Formiat Produktion bei -1,5 V *vs* Ag/AgCl mit Bildungsraten hin bis zu 85,5 $\mu mol\ h^{-1}\ cm^{-2}$.

Kapitel 4

Kupferoxide (CuO und Cu_2O) sind vielversprechende Materialien für die Bildung von Kohlenwasserstoffen bei der elektrochemischen CO_2-Reduktion. In diesem Kapitel wird eine neue Methode vorgestellt, in der DES-Kupfer-Mischungen in oxidativer Atmosphäre kalziniert werden, woraus kohlenstoffdotierte Kupferoxidkatalysatoren (CuO/CNO) resultieren. Abhängig von den genauen Herstellungsbedingungen zeigen REM-Aufnahmen unterschiedliche Morphologien der Materialien und mittels XRD konnten verschiedene Oxidationsstufen von Kupfer festgestellt werden. Eine 60-minütige Kalzinierung bei 500 °C in Luft liefert ausschließlich CuO-Katalysatoren, während eine kürzere Kalzinierzeit (10 min oder 15 min) auch zu weniger oxidierten Kupfermodifikationen (Cu_2O und Cu^0) führt. Linear Sweep Voltammetrie und Chronoamperometrie zeigen eine hohe Stromdichte in CO_2 gesättigten Elektrolyten. Die chemische Produktanalyse zeigt eine erhöhte Selektivität hin zu C2- und C3-Produkten. Mit Bildungsraten von 7,4 (Ethanol), 6,0 (n-Propanol) und 10,4 $\mu mol\ h^{-1}\ cm^{-2}$ (Ethen) bei 1,7 V *vs* Ag/AgCl ist die Konzentration der Produkte im Vergleich zu kommerziellem CuO erheblich höher.

APPENDIX

7 Appendix

Abbreviations

°C	degrees Celsius
Å	Ångström (10^{-10} m)
AC	activated carbon
Ag/AgCl	silver/ silver chloride reference electrode
Ar	argon
Atm.	atmosphere
A.U.	arbitrary unit
BET	Brunauer-Emmet-Teller analysis
BSE	backscattered electrons
c	concentration
C	choline chloride
CA	chronoamperometry
CE	counter electrode
CNO	supporting material consisting of carbon, nitrogen and oxygen
CO_2R	electrochemical CO_2 reduction
cm^2	square centimeter
C1	products consisting of one carbon atom *e.g.* CO and formate
C2	products consisting of two carbon atoms *e.g.* ethylene and ethanol
C3	products consisting of three carbon atoms *e.g.* n-propanol
Cu/CNO	copper supported on CNO
CuO/CNO	copper oxide supported on CNO
CV	cyclic voltammetry
Δ	delta
D	*N,N′*-dimethylurea
DES	deep eutectic solvent
DSC	differential scanning calorimetry
E	electrode potential
EDX	energy dispersive X-ray
e.g.	for example (*lat.* exempli gratia)
et al.	and others (*lat.* et alii)

eV	electron volt
F	ᴅ-fructose
FE	Faraday efficiency
g	gram
G	ᴅ-glucose
Ga	ᴅ-galactose
GC-MS	gas chromatography with mass spectrometry
GDL	gas diffusion layer
h	hour
HBA	hydrogen-bond acceptor
HBD	hydrogen-bond donor
He	helium
λ	wavelength
L	lignin
LSV	linear sweep voltammetry
M	molar (mol L^{-1})
mg	milligram
min	minute
mL	milliliter
mM	millimolar (mmol L^{-1})
mV	millivolt
mmol	millimole
µL	microliter
µm	micrometer
µmol	micromole
nm	nanometer
Pd/CNO	palladium supported on CNO
ppmv	parts per million by volume
RE	reference electrode
RHE	reversible hydrogen electrode
s	second
SEM	scanning electron microscopy
SHE	standard hydrogen electrode

SCE	saturated calomel electrode
T	temperature
TCD	thermal conductivity detector
TGA	thermogravimetric analysis
T_m	melting point
U	urea
V	volt
V	vanillin
vs.	against (*lat.* versus)
wt%	weight percent
XPS	X-ray photoelectron spectroscopy
XRD	powder X-ray diffraction

DANKSAGUNG

8 Danksagung

Mein besonderer Dank gilt meinem Doktorvater Herrn Prof. Dr. Burkhard König, der es mir ermöglicht hat, meine Dissertation in Zusammenarbeit mit dem Institutsteil Straubing des Fraunhofer IGB anfertigen zu können. Burkhard, ich möchte mich ganz herzlich für die spannende Themenstellung, die Unterstützung, die Motivation und die unkomplizierte Zusammenarbeit während der letzten Jahre bedanken!

Bei Herrn Prof. Dr. Volker Sieber möchte mich ganz herzlich bedanken, dass er es mir ermöglicht hat, meine Dissertation am Institutsteil Straubing des Fraunhofer IGB in einem tollen Umfeld anfertigen zu können, und für die Übernahme des Zweitgutachtens. Volker, vielen lieben Dank für deine Unterstützung, die Motivation und die gute Zusammenarbeit während der letzten Jahre!

Vielen Dank an Prof. Dr. Frank-Michael Matysik und Prof. Dr. Alexander Breder, für die Zeit, die sie sich genommen haben, um in meinem Prüfungsausschuss mitzuwirken.

Mein besonderer Dank gilt Dr. Tobias Gärtner für die Einführung in das spannende Thema der Katalysatorherstellung aus DES, die regelmäßigen Diskussionen, die permanente Unterstützung, die motivierenden und aufbauenden Worte in den letzten Jahren und das Korrekturlesen meiner Arbeit. Tobi, vielen lieben Dank, dass du immer ein offenes Ohr für mich hattest und für die Zeit, in der du mich super unterstützt hast!

Ganz herzlich möchte ich mich auch bei Dr. Luciana Vieira bedanken für die Einführung in die Elektrochemie, die vielen Diskussionen und das Korrekturlesen meiner Arbeit. Luciana, herzlichen Dank, dass du immer Zeit für mich hattest und mich gerade im Endspurt meiner Arbeit so tatkräftig unterstützt hast!

Herrn Apl. Prof. Rainer Müller möchte ich für die zahlreichen BET Messungen danken. Bedanken möchte ich mich auch bei Sabine Kugler, Christina Sagmeister, Sabine Witzel und Dr. Daniel Van Opdenbosch für die Geräteeinführungen und Hilfe bei REM Aufnahmen, Elementaranalysen und XRD Auswertungen.

Meinen Studenten Jasmin Finkelmeyer, Igor Rud, Martin Friedrich und Johannes Pößnecker danke ich für ihre Mitarbeit an meinen Forschungsprojekten.

Vielen lieben Dank an meine Studienkollegen Ricarda, Olga, David und Franzi für die gegenseitige Unterstützung und eure Freundschaft. Ihr habt das Studium zu einer großartigen Zeit gemacht!

Danke an alle derzeitigen und ehemaligen Mitarbeiter des Arbeitskreises König in Regensburg für eine tolle Atmosphäre und die Hilfsbereitschaft, trotz der wenigen Zeit, die ich in Regensburg verbracht habe.

Bei Anika Söldner und Martin Obst möchte ich mich für ihre Hilfe und die guten Diskussionen in unserer kleinen Runde über die Arbeiten mit DES bedanken.

Für ihre Hilfsbereitschaft, die super Zusammenarbeit und vielen Diskussionen, die gemeinsamen Mittags-, Eis- und Kaffeepausen, die spaßigen Ausflüge und Abende danke ich allen Mitarbeitern in Straubing: Annette, Anton, Carina, Christina, Claudia, Dhananjai, Harald, Johanna P.,Johannes, Jonathan, Julia, Lena, Lenard, Leonardo, Luciana, Manuela, Marion, Melanie, Michael H., Michael R., Patricia, Paul, Sabine, Sigita, Steffen, Sumanth, Tobias und Vanessa.
Ihr habt die letzten Jahre zu etwas ganz Besonderem gemacht!

Besonders möchte ich mich auch bei meinen Freunden bedanken, vor allem bei Anna und Nina, für die permanente Unterstützung und einfach dafür, dass ihr immer für mich da seid. Mit euch zusammen ist alles einfach lustiger und schöner!

Von ganzem Herzen danke ich schließlich meiner ganzen Familie, besonders aber meinen Eltern und meinem Bruder. Worte allein können nicht ausdrücken, wie dankbar ich euch für eure Liebe, euren Rückhalt, eure Ermutigung, Motivation und Unterstützung bin.
Ohne euch wäre diese Arbeit nicht möglich gewesen!

Danke